DIRECTED SELF ASSEMBLY OF BLOCK COPOLYMERS

A Dissertation
Presented to
The Academic Faculty

By

Benjamin D. Nation

In Partial Fulfillment
of the Requirements for the Degree
Doctor of Philosophy in the
School of Chemical and Biomolecular Engineering

Georgia Institute of Technology

August 2017

DIRECTED SELF ASSEMBLY OF BLOCK COPOLYMERS

Approved by:

Dr. Clifford L. Henderson,
Advisor
School of Chemical and
Biomedical Engineering
University of South Florida

Dr. Peter J. Ludovice,
Advisor
School of Chemical and
Biomolecular Engineering
Georgia Institute of Technology

Dr. J. Carson Meredith
School of Chemical and
Biomolecular Engineering
Georgia Institute of Technology

Dr. Andrew J. Medford
School of Chemical and
Biomolecular Engineering
Georgia Institute of Technology

Dr. David Bucknall
School of Engineering and
Physical Sciences
Heriot Watt University

Date Approved: July 14, 2017

ACKNOWLEDGEMENTS

I would thank both Dr. Clifford Henderson and Dr. Peter Ludovice for serving as my thesis advisors these last few years. Dr. Henderson has given me great guidance over the years, helping brainstorm new ideas and challenging bad ideas. Dr. Peter Ludovice always added great entertainment to all our group meetings and was a helpful source of ideas whenever I hit a roadblock. I would also like to thank the rest of the professors who served on my thesis committee, including Dr. Carson Meredith, Dr. David Bucknall, Dr. Andrew Medford, and Dr. Laren Tolbert.

There have been many group members to help me over the years. Dr. Richard Lawson and Dr. Andrew Peters were both immensely helpful in the early years of my research. These two spent lots of time teaching me about our simulation methods and in developing my ability to design experiments. Additionally, we often had good discussions/debates in our office. I would also like to thank Caleb Breaux who has been a constant friend throughout graduate school. His unique view of the world often helps improve the mood of the group and is quite fun for spawning discussions. Also, he has been fun competition for various games, such as Pokemon and Chess. Dr. Wei-Ming Yeh initially trained me in many various cleanroom techniques. Hannah Narcross and Brandon Sharp were fun additions to the group who made trips and time in the cleanroom more enjoyable.

I have had many friends over the years who have supported me in this time. Dr. Krishna Jayachandrababu has been a good friend ever since I met him and Caleb at the graduate recruitment weekend. Josh Davis, Micah Lansing, and Darrell Hines are all great men who I have enjoyed many discussions with over the years. I would like to thank my oldest friend Ralph Long who has been a roommate, a best man, and a good friend throughout these years. Along with Ralph, Drew Showalter and Dr. Kevin Skenes were great fun to play both Overwatch and Team Fortress 2 with. Finally, I had the pleasure of being a groomsman for both Andy Bunting and Hunter Reed, and the honor of having them both

as my own groomsmen.

I would like to thank my family who has grown greatly over the years. I have gained a brother-in-law, five nieces, and two nephews from my siblings. In addition, with my marriage I have gained a mother, father, sister, and two brothers. All these have been very supportive of me over the years.

Last and certainly not least I would like to thank my wife Parke. She has been with me through my entire time in grad school, marrying me a couple years into it. She has supported me in many ways through the years, both by earning the big bucks to support our family during at times and in other times by being a loving stay-at-home wife. She is a constant source of fun and companionship, and I look forward to spending the rest of my life with her.

TABLE OF CONTENTS

LIST OF TABLES

LIST OF FIGURES

List of Abbreviations

BCP	Block Copolymer
CD	Critical Dimension
CED	Cohesive Energy Density
CPU	Central Processing Unit
DSA	Directed Self-Assembly
EUV	Extreme Ultraviolet
GPU	Graphics Processing Unit
ITRS	International Technology Roadmap for Semiconductors
L_0	Natural Repeat Distance (Pitch or Domain) of a BCP System
LER	Line Edge Roughness
LiNe Flow	Liu-Nealey Flow
LWR	Line Width Roughness
MC	Monte Carlo
MD	Molecular Dynamics
MF	Mean Field
ML	Mixed Lamellae
N	Degree of Polymerization
NA	Numerical Aperture
NVT	Canonical Ensemble
NPT	Isothermal-Isobaric Ensemble
ODT	Order Disorder Transition
PCND	Protracted Colored Noise Dynamics
PS	Polystyrene
PMMA	Poly(methyl methacrylate)
SCFT	Self-Consistent Field Theory
VWD	Variation of Width through Depth
χ	Flory-Huggins Interaction Parameter

SUMMARY

Block copolymer (BCP) directed self-assembly (DSA) is currently being explored as a potential method for producing smaller features in the integrated circuit fabrication industry. However, before implementation a few challenges must be overcome. These include lowering line edge roughness (LER), lowering line width roughness (LWR), and increasing pattern registration. Most notably though, while the defectivity of current BCP-DSA systems is low and difficult to characterize experimentally, it is still too high to satisfy the requirements of the integrated circuit fabrication industry. In this work a coarse-grained molecular dynamics model is used to look various aspects of this problem. Additionally, a new simulation technique is introduced that helps polymeric molecular dynamics simulations cross energetic barriers more easily.

In Chapter 3 the ability of chemoepitaxial guiding underlayers to aid in the formation of a defect free array of lamellae is considered for both symmetric BCPs and asymmetric BCPs. In Chapter 4 the free energy of defects of various sizes is measured as a function of the level of density multiplication in the underlayer and the position of the defect relative to the guiding pattern. In Chapter 5 factors other than defectivity, such as the line edge roughness of the resulting film and the variations of lamellae width through the depth of the film, are considered. In Chapter 6 various geometrical and energetic parameters in a hybrid chemoepitaxial and graphoepitaxial guiding underlayer are considered with regards to defectivity of the resulting film. These four chapters provide an improved understanding of the effect underlayer design has on BCP-DSA and the resulting defectivity.

In Chapter 7 a new simulation technique, Protracted Colored Noise Dynamics (PCND), is introduced. This technique introduces a time correlated force to polymer chains in molecular dynamics simulations. This force helps encourage a reptation like motion of the chains, and therefore increases diffusion and sampling across energetic barriers, increasing the kinetics of the simulation.

CHAPTER 1
INTRODUCTION AND BACKGROUND

This chapter is intended to give an introduction to block copolymers (BCPs) and directed self-assembly (DSA). The primary motivation for this work will be given by discussing the limitations of optical lithography. Next, a detailed description of what a block copolymer is and how they phase separate will be given. Following this, directed self assembly, the means of controlling the patterns made by BCPs, will be explained. The ongoing challenge of defectivity for BCP DSA will be discussed. Finally, a brief overview will be given of models used in simulating BCP DSA.

1.1 Optical Lithography

A key step in the fabrication of integrated circuits is optical lithography. In optical lithography (Figure 1.1), a chemical called a photoresist is coated onto a silicon wafer through a process called spin coating (Figure 1.1A). Photoresists are chemicals that undergo either an increase or a decrease in solubility to a solvent when exposed to light. Once coated, the photoresist film is selectively illuminated by shining light through a chrome mask that is composed of regions that block the light and regions that allow the light to pass through (Figure 1.1B). The exposed portions of the film react in a way that changes the solubility (Figure 1.1C). After the solubility change, the resist is "developed", where either the exposed region or the unexposed region (depending on the type of resist) is removed by a solvent. There are two basic types of resists, "positive tone" and "negative tone". In a positive tone resist, the exposed region of the resist will be removed (Figure 1.1D), while in a negative tone resist the unexposed region is removed (Figure 1.1E).

A typical positive tone resist is a polymer that has a protecting group attached to it to make the resist hydrophobic. However, exposure to light will cause the resist to undergo

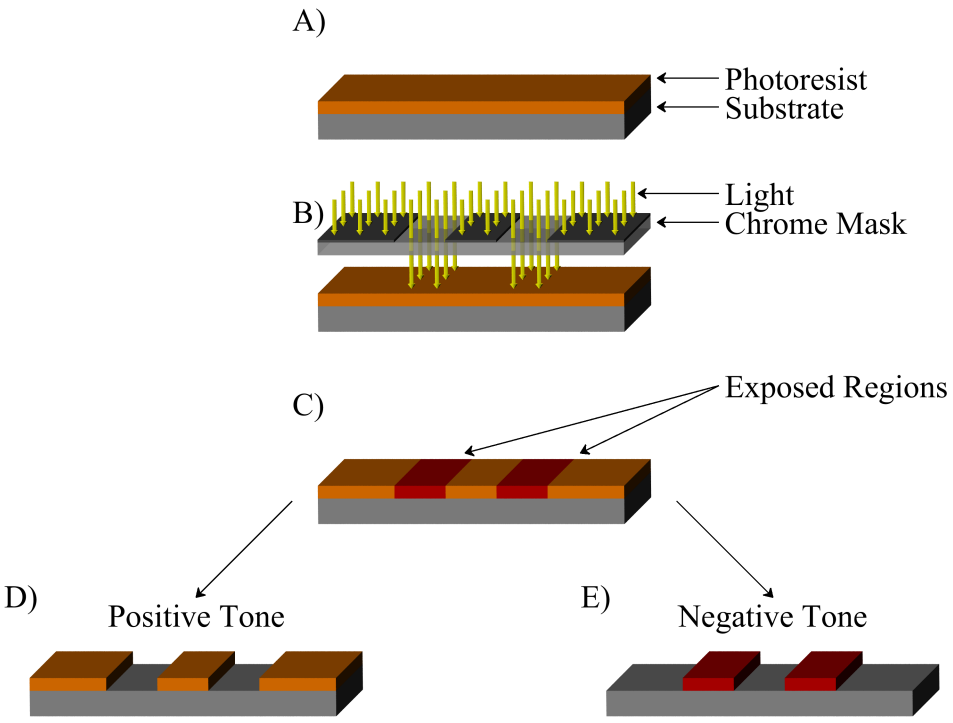

Figure 1.1: An cartoon of the process flow for optical lithography. A) A photoresist film is placed on a substrate. B) Light is shown through a mask to selectively expose the photoresist. C) The resist undergoes a reaction where exposed. D) If undergoing positive tone development, the exposed region leaves. E) If undergoing negative tone development, the unexposed region leaves.

a deprotection reaction, removing the protecting group and making the resist hydrophilic in the exposed regions. Then, the exposed region can be developed using an aqueous solvent which will selectively remove the exposed, hydrophilic region while leaving the unexposed, hydrophobic region behind. These resists can also be developed in an organic solvent (removing the unexposed region, effectively making these resists negative tone).

Negative tone resists typically utilize a different mechanism. A typical negative tone resist is composed of polymer chains that have crosslinkable groups built into the chains. When exposed to light, these negative tone resists will undergo a cross-linking reaction, forming an insoluble cross-linked network. After devolopment, the remaining photoresist is used as a mask to selectively either etch the substrate beneath it or to dope the silicon.

The advancement of optical lithography has been one of the key steps in the growth of the semi-conductor manufacturing industry. In order to make faster, more efficient processors, the size of transistors has been continually shrunk since their introduction, allowing for more transitors to be packed into the same area.[1] It can be seen in Figure 1.2 that the number of transistors per CPU has increased exponentially over the past few decades. This is essentially a statement of Moore's Law, which is an observation that the number of transistors per CPU doubles every couple years. This trend has been useful in making integrated circuits since there are many benefits in making smaller transistors. The smaller the transistor, the quicker it can be switched from on to off. Additionally, less energy is required to make this switch. And, as summarized in Figure 1.2, more transistors can be placed in the same size area.

Optical lithography is a highly important step in making these transistors. However, there are limits on the minimum feature size that can be patterned using optical lithography. The minimum feature size, or critical dimension (CD) is controlled by the following equation:

$$\text{CD} = k_1 \cdot \frac{\lambda}{\text{NA}}\,, \tag{1.1}$$

where λ is the wavelength of light used to expose the sample, NA is the numerical aperture

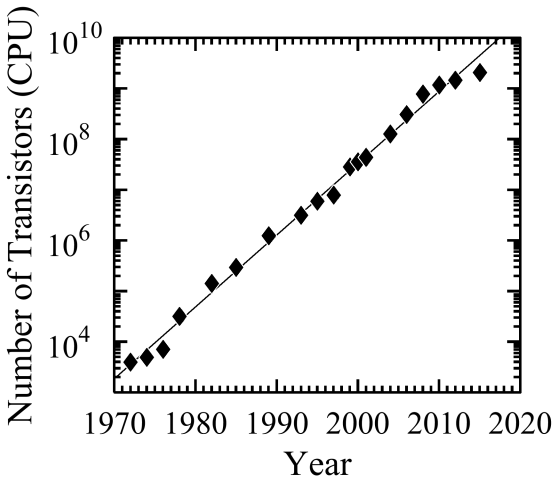

Figure 1.2: A plot of the number of transistors on a CPU versus the year.[2]

of the lens, and k_1 is a process dependent factor, theoretically limited to 0.25.[3] Based on this equation, there are a couple possible options for decreasing the minimum critical dimension. First, one could increase the numerical aperture, which is governed by the following equation:

$$\text{NA} = n \sin\theta \,, \tag{1.2}$$

where n is the index of refraction of the medium the lens is working in and $\sin\theta$ is related to the size of the lens. The size of lens has already been increased as much as is economical. In order to increase the index of refraction, more recent lithography tools replaced the medium of air ($n \approx 1$) with water ($n \approx 1.33$). This is a method known as immersion lithography. However, it should be noted that while minimum CD decreases with increasing NA, the depth of field decreases with increasing NA quadratically, as shown by the following equation.

$$d = \frac{\lambda \cdot n}{\text{NA}^2} \,, \tag{1.3}$$

Another option for decreasing the minimum critical dimension (Equation 1.1) is to decrease the wavelength of light used for exposure (λ). This has been one of the primary steps taken in the past decades, starting with 436 nm light, moving to 405 nm, 365 nm,

248 nm, and finally 193 nm light now. While some lower wavelength light sources have been pursued, none have yet managed to succeed in replacing 193 nm when combined with using immersion lithography (193i). Instead, the industry has started a process known as double patterning.[4] As the name implies, in double patterning there will be two optical lithography steps instead of one. The first step will make a pattern, then there will be a second exposure that makes features between the original features. This method can be difficult to do in practice since the two exposures must be very well aligned, but this has been done in industry with great success so far. The larger problem with this method is that the optical lithography step in the fabrication process is the most expensive part of the process, so the cost of this step is now being doubled.

A current focus of the industry is in getting an extreme ultraviolet (EUV) light source into production.[5] This light source has a wavelength of 22 nm, which would drastically decrease the minimum feature size. While EUV lithography is likely going to be used soon in industry, there are still a few issues that need to be overcome. Specifically, EUV tools still have a very low throughput and require very large amounts of power due to the inefficiency of the mirrors used for focusing the light.

One possible option to continue making smaller feature sizes is to use block copolymer directed self-assembly (BCP-DSA) which will be detailed in the next two sections.[1] In BCP-DSA, optical lithography will be used to make a guiding pattern for a BCP film, then the BCP will microphase separate on this guiding pattern in a way that increases the density of features. Through this method block copolymers may be able to extend the usefulness of optical lithography, which useful since optical lithography is a process very well known and understood by the industry.

1.2 Block Copolymers

Block copolymers (BCPs) are molecules composed of two or more different homopolymers covalently bonded together. A homopolymer molecule is a molecule composed of a

single repeated monomer unit, all covalently bonded together in a chain. In the simplest variety of BCP, two different homopolymers are covalently bonded together at their end, making a linear diblock copolymer, as shown in Figure 1.3A. However, there are more complicated forms of block copolymers, such as a linear triblock copolymer (Figure 1.3B or star copolymers (Figure 1.3C). All work done in this thesis is on linear chain diblock copolymers.

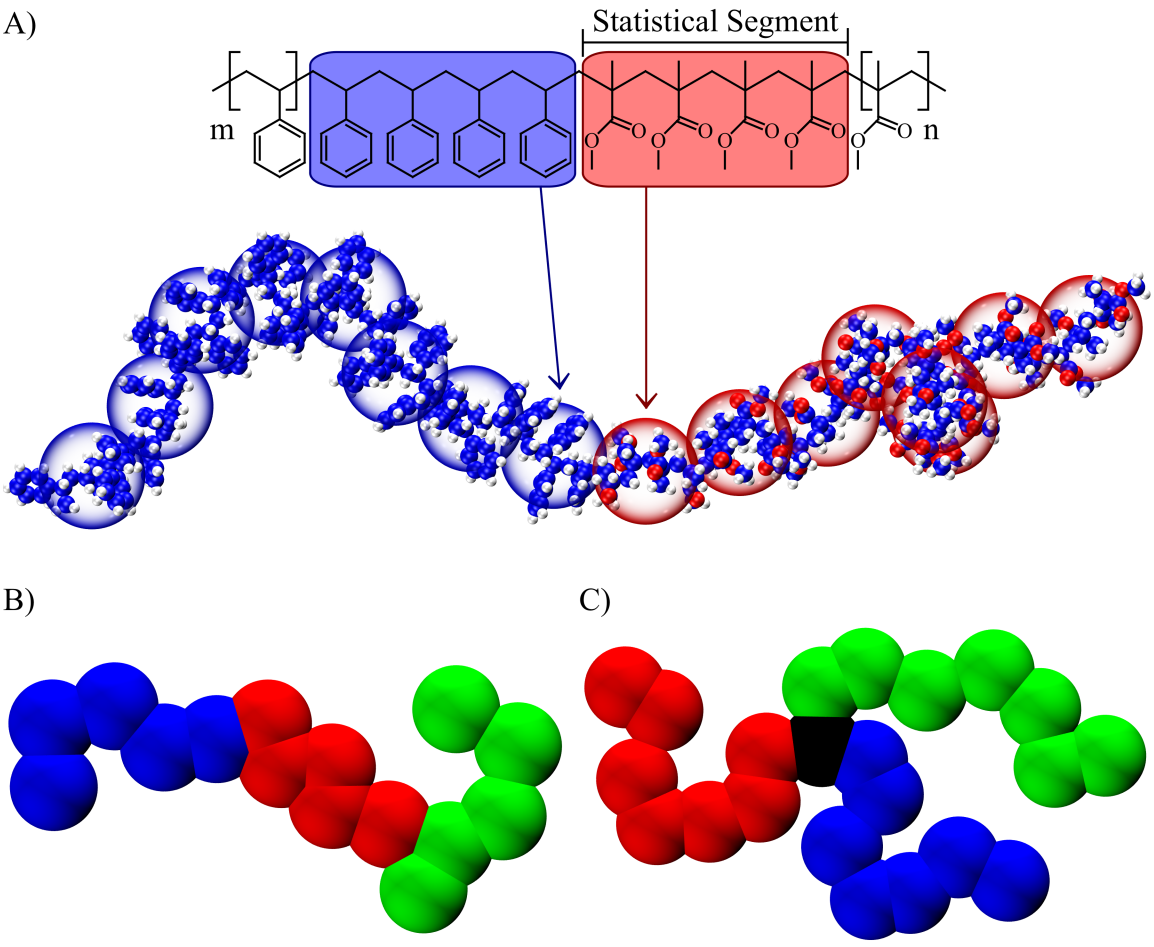

Figure 1.3: Examples of various block copolymers. A) An atomistically detailed example of a linear chain diblock copolymer. The larger transparent beads represent the coarse-grained chain where four monomeric units are combined into a single bead. B) A linear chain triblock copolymer of the form ABC where the blocks are composed of either A beads (blue), B beads (red), or C beads (green). C) A triblock star copolymer.

It is known from polymer physics that two different homopolymers will attempt to

phase separate when their parameter χN is sufficiently high ($\chi N > 2$). Here, χ is the Flory Huggin's parameter which gives a measure of the enthalpy of mixing for polymers. This parameter quantifies the degree to which a block prefers to be near itself versus being near the other block. This is multiplied by N or the degree of polymerization of the polymers, *i.e.* how many monomers make up the homopolymer chains. Therefore, if the degree of polymerization (N) is large enough, or the homopolymers dislike each other enough (χ is large), the homopolymer mixture will separate and form two distinct polymeric phases.

This macrophase separation cannot occur in the case of a BCP since the two different homopolymers are covalently tethered to each other. However, if the value of χN is high enough ($\chi N > 10.495$ for a volume fraction, ϕ, of 0.5) phase separation will occur, though not on a macro scale.[6] Instead, regular repeating structures will form known as microphases. There are four primary phases known for a linear chain diblock copolymer which are summarized in Figure 1.4.[6, 7] If the volume fraction of A beads (ϕ_A) is very small, implying a large volume fraction of B block (ϕ_B) since $\phi_A + \phi_B = 1$, then a morphology forms that consists of spheres of A formed in a B matrix. These spheres can be packed in a body-centered cubic fashion or a close packed fashion,[8] or more complex phases such as a Frank Kasper phase.[9] If the volume fraction of A increases, these spheres start to become more oblong, eventually connecting to form cylinders. These cylinders are ideally hexagonally close packed. As the volume fraction continues to increase, their cross-sections become more oblong. At this point, if the value of χN is sufficiently low, a complex phase known as the bicontinuous or gyroid phase can form. Finally, as the volume fraction approaches $\phi_A \rightarrow 0.5$ a lammelar phase forms. Continuing past $\phi_A = 0.5$, these phases will occur in reverse order with the B block (the minority block now) being the cylinders and spheres with the A block being the matrix. The location of all of these order-order transitions can be seen in the traditional mean-field phase diagram shown in Figure 1.4. Here, the phases are shown as a function of the volume fraction of the A block, ϕ_A, and χN. It can also be seen that with a sufficiently low driving force (χN) or an extreme

enough volume fraction ($\phi_A \rightarrow 0$ or $\phi_A \rightarrow 1$) the BCP will disorder. In this disordered region no regularly repeating structures will appear. However, unless $\chi N = 0$, there will be some level of grouping present in the BCP, but none of this order is long range.

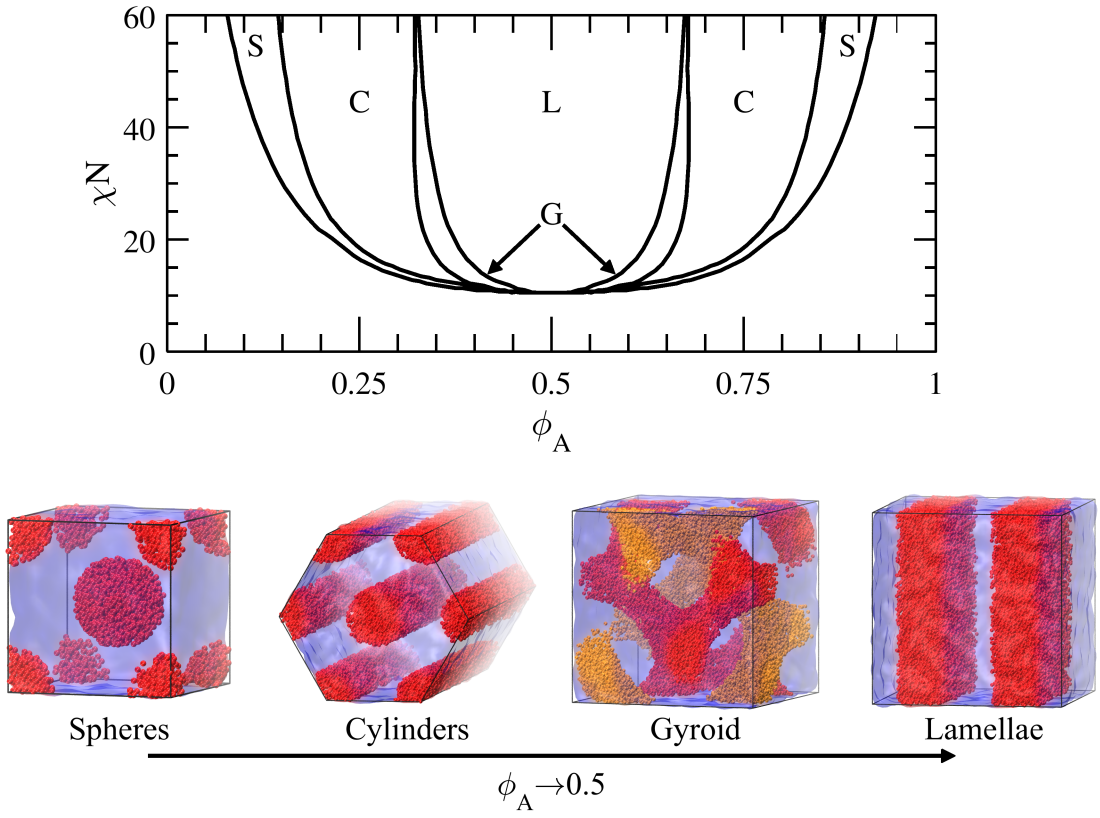

Figure 1.4: The mean field phase diagram[10] and the associated phases. Moving from low volume fraction to high volume fraction the phases are spheres, cylinders, gyroid, and lamellae. The A beads are drawn as red beads (and yellow in the gyroid phase) while the B beads are shown by the blue matrix.

The size scale of the repeat distance of the microphases is approximately equal to the size of a polymer chain itself (or the radius of gyration). The repeat distance is found to increase with χ and N according to the following equation.

$$L_0 \propto N^{\alpha} \cdot \chi^{\frac{1}{6}}, \tag{1.4}$$

where L_0 is the pitch or repeat distance of the features and N is the total degree of poly-

merization of the BCP. In this equation, $\alpha = \frac{2}{3}$ in the strong segregation regime (when the product of the Flory Huggins χ parameter and the N is large), while $\alpha = \frac{1}{2}$ in weak segregation regime (when χN is small).[11] Because the integrated circuit manufacturing industry is ever driving towards smaller features, much work has been done to decrease the pitch of the BCPs. The general approach taken is to try to increase χ as much as possible (which only weakly increases L_0) in order to allow as small a degree of polymerization (which has a strong effect on L_0) as possible while still allowing for phase separation ($\chi N > 10.495$). Typically this is done by forming BCPs out of two highly different homopolymers, such as one homopolymer that has solely dispersion forces and a second homopolymer that has hydrogen bonding.[12] These higher χ block copolymers will be discussed further in Chapter 3.

There are many potential applications for these microphases. Multiple phases of BCPs are being explored for use in solar cells, batteries, and fuel cells.[13] BCPs are currently being used in the field of drug delivery.[14] The membrane field is also currently interested in BCPs.[15] Additionally, in some cases the spherical and cylindrical phases have been shown to greatly increase the resiliency of some coatings.[16]

The cylindrical and lamellar morphologies are of particular interest to the semiconductor manufacturing industry.[17, 1] This is because the cylindrical phase is reminiscent of contact vias while the lamellar phase is reminiscent of line space patterns, both of which are frequently used in optical lithography. The focus of this work will be on lamellae forming diblock copolymers.

1.3 Directed Self-Assembly

In order to be used in integrated circuit manufacturing, the block copolymer will be put into a thin film form, typically by a process known as spin coating. Depending on the substrate two different morphologies can occur. If the substrate is highly preferential to one block of the BCP versus the other, the lamellae will form parallel to the substrate. This is referred

to as horizontal lamellae. Here, the preferred block of the BCP will wet the substrate, making a layer of that block which will then have alternating layers of the different blocks above it. An example of this can be seen in Figure 1.5A. If, however, the substrate is sufficiently neutral (and unpatterned, meaning it gives no guidance to the BCP film) to both blocks of the BCP, vertical lamellae form, perpendicular to the substrate, as can be seen in Figure 1.5B. While these lamellae are vertical there is still a level of disorder in them. This morphology is known as a fingerprint lamellae due to how the patterns it forms, particularly when looked at on a larger scale, are similar to those of a human fingerprint.

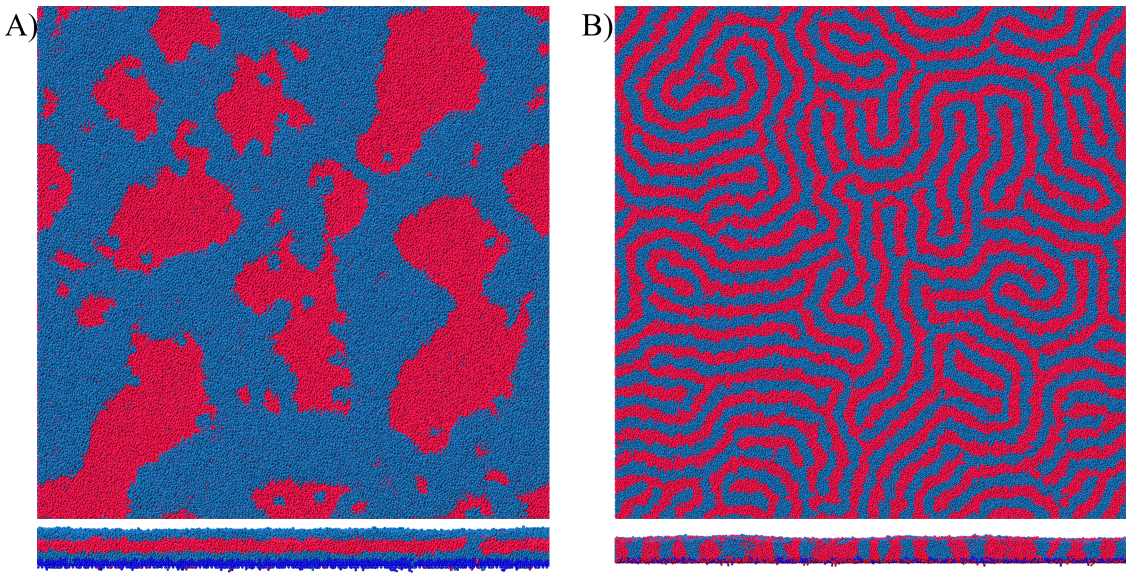

Figure 1.5: An example of A) the horizontal lamellae morphology and B) the fingerprint morphology. The top image is the topdown view, while the bottom image is a cross-sectional image of the same simulation. Blue beads represent A monomers and red beads represent B monomers. Due to the film being an incommensurate film thickness ($0.75\ L_0$), in A) there are two different levels of film thickness present, a thicker "island" portion appearing as blue on the top down view and a thinner "hole" portion appearing as red.

For block copolymers to be useful in the semiconductor manufacturing industry these fingerprinted films are going to have to be guided into desired shapes. To do this a guiding underlayer is placed on the wafer before coating the BCP on top of the wafer. This guiding underlayer will be patterned/designed using optical lithography. The design of the guiding underlayer will then influence the BCP on top of it, guiding the BCP to the desired structure.

There are two primary types of guiding underlayer, chemoepitaxy and graphoepitaxy which will be explained below. Additionally, there are a few newer guiding underlayers that are a combination of chemoepitaxy and graphoepitaxy. These underlayers will be discussed in Chapter 6.

The reason BCPs can be useful in extending optical lithography is because of density multiplication.[18] Instead of making a guiding pattern that would guide every single BCP lamellae, a guiding pattern can be made that will only guide every few lamellae. Lamellae forming diblock copolymers desire to form a large, defect free lamellae region since this is the lowest free energy state.[19] Defects and curvature of the lamellae is very unfavorable. Therefore, since some of the BCP is forced to form straight lamellae above the guiding pattern, the BCP will also form properly above the missing guiding pattern to avoid the formation of defects. This process is called density multiplication, since the density of the pattern that results is some integer multiple of the density of the pattern made lithographically. Through this, optical lithography can make a pattern with a pitch, then use BCP DSA to form features with a fraction of that feature size.

1.3.1 Graphoepitaxy

Graphoepitaxial guiding underlayers use topographic features in the underlayer to help align the BCPs. A common example of this can be seen in Figure 1.6. Here, there is a periodic step height in the underlayer. These raised features are typically preferential to one block of the BCP, while the flat portion of the underlayer is ideally neutral to each block. The block copolymer is then used to fill in the trench. As the block copolymer phase separates, the preferred block will wet the sidewall, thus directing the self-assembly of the BCP. It should be noted that the width of the trench should be some integer multiple of the natural repeat distance of the block copolymer so that the block copolymer can properly fit in the trench. If the trench is too narrow or too wide the block copolymer will likely either have more defects or form a ladder morphology (where the lamellae direction is perpendicular to

the direction of the trench).[20, 21, 22] The degree of density multiplication is the integer multiple of the pitch that the width of the trench is, since this is the number of repeats the block copolymer forms for each pattern made by optical lithography.

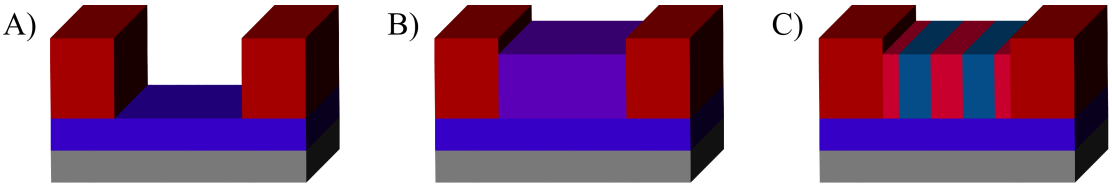

Figure 1.6: An example of a process flow with a graphoepitaxial guiding underlayer. A) A topographic pattern is made using optical lithography. Here the red topographic features are preferential to the red BCP block and the purple base of the trench is neutral to the two blocks. B) A BCP is coated, filling in the trench of the topography. The BCP is shown here as violet to indicate it is currently a mixture of the blue and red blocks. C) After the film is allowed to anneal, the blue and red blocks phase separate with the red block wetting the sidewalls.

1.3.2 Chemoepitaxy

Chemoepitaxial guiding underlayers use regions of differing chemical preference to help align the BCPs. A common example of this can be seen in Figure 1.7. Here, the underlayer consists of a repeated pattern of two different regions. The first is a thin, highly preferential region. This region helps pin down one block of the BCP and is therefore known as the "pinning" stripe. The other region which separates pinning stripes is known as the "background" region. The background region is more neutral to both blocks of the BCP, though is frequently slightly preferential to the block that is not preferred by the pinning stripe. For this underlayer, the pinning stripes will pin down one lamellae, then through directed self-assembly and density multiplication the block copolymer fills in the region between the pinning stripes.

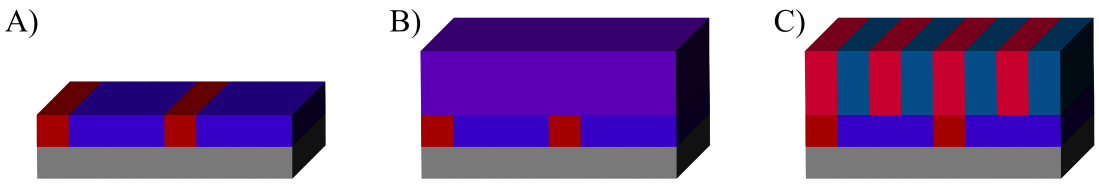

Figure 1.7: An example of a process flow with a chemoepitaxial guiding underlayer. A) A chemoepitaxial pattern is made. Here the red pinning stripes are preferential to the red BCP block and the purple background region is neutral to the two blocks. B) A BCP is coated, shown here as violet to indicate it is currently a mixture of the blue and red blocks. C) After the film is allowed to anneal, the blue and red blocks phase separate with the red block wetting the pinning stripes.

1.4 Ongoing Challenges in BCP-DSA

The primary challenge in BCP-DSA is that defectivity is higher than is allowable. Despite guidance by the underlayer, lamellae do not always form defect free morphologies. Line defects such as dislocations (Figure 1.8) and disclinations may form at the surface or in the through-film morphology. Experimentally these defects occur at frequencies above the 1 defect per 100 cm^2 maximum that the ITRS desires.[23] The cause for the higher defect densities is thought to be one of three sources: 1) non-BCP related procedures (*e.g.* dust particles, errors in patterning the underlayer, etc.), 2) the free energy of the defects are low enough that their equilibrium density is appreciable, or 3) the defects are kinetically trapped (*i.e.* the defects will eventually go away, but it may take a long time). In previous investigations in the free energy of defects it was found that the relative free energies for common simple defects such as dislocations were found to be above $300\ k_B\ T$[24, 25], which yields a very low defect density using Eq. 1.5.

$$\rho \propto exp\left(\frac{-\Delta F}{k_B\, T}\right) \tag{1.5}$$

where, ρ is the defect density, k_B is the Boltzmann constant, T is the temperature, and ΔF is the difference in the free energy of a defect versus the free energy of a defect free state.

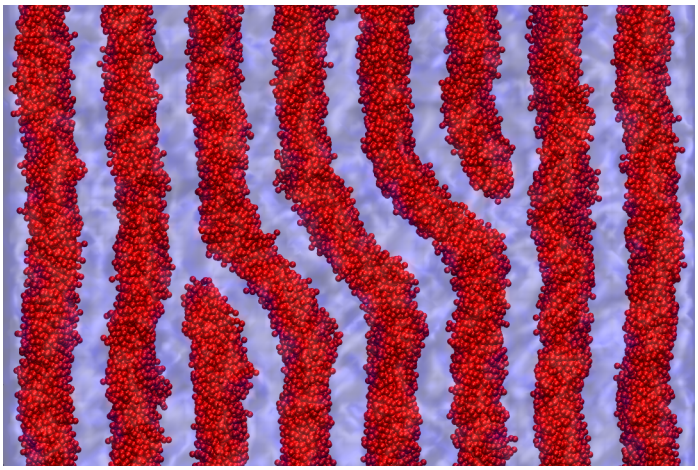

Figure 1.8: A dislocation pair defect is shown as an example of a kinetically trapped defect that can occur in a BCP simulation. Red beads represent type A, while the blue matrix represents type B. In Chapter 4 this defect will be called defect order 5. This defect order is a measure of the number of continuous jog lamellae separating the two dislocations, which here includes three red lamellae and two blue lamellae. Images are rendered using VMD.[26, 27]

The work presented in this thesis is primarily dealing with defectivity in BCPs. In Chapter 3 the design of chemoepitaxial guiding underlayers is explored to find conditions that minimize defectivity. Additionally, the effect that changing the BCP has on defectivity is explored. The free energy of dislocation defects (Figure 1.8) of various sizes is measured on various underlayers in Chapter 4. In Chapter 5 other factors such as the line edge roughness (LER) and the through film shape of lamellae are considered. Finally, in Chapter 6 the design of mixed chemoepitaxial and graphoepitaxial guiding underlayers is explored again looking for conditions that minimize defectivity.

1.5 Modeling of Block Copolymers

Many models exist in the literature to simulate block copolymers and directed self assembly. Self-consistent field theory (SCFT) or mean-field theory is a very important model in this field.[28, 29] In SCFT, a single representative BCP chain is simulated inside a field that represents interactions the chain would have with the rest of the BCP. This field is defined

from the single representative chain in a self-consistent way. This model has many great benefits, such as a fairly quick simulation speed and the fact free energy is easily calculated from the model. The drawbacks to the model are the difficulty in exploring non-equilibrium stuctures and in looking at fluctuations. This model has been the source of the majority of all BCP simulations.

The second main stype of BCP simulation involves looking at an ensemble of BCP chains. Typically, these chains are coarse-grained in such a way that each particle being tracked in the simulation represents one or more monomers. For example, in Figure 1.3A a sample is shown where four monomeric units are combined into a single unified bead. Coarse-graining is useful for many reasons. First, coarse-graining decreases the degrees of freedom in the system significantly, allowing for either faster computations or larger size scale simulations. Second, coarse-graining allows for a larger simulation timestep in molecular dynamics, allowing longer simulation times. This is incredibly valuable since microphase separation occurs on a far larger size scale and a far larger time scale than traditional atomistic simulations can reach. Once coarse-grained, the ensemble of chains will typically undergo either Monte Carlo or molecular dynamics simulations. Both of these methods are valuable since they can give increased information about fluctuations that are difficult to capture using SCFT.

In this work a molecular dynamics model is used. In molecular dynamics, the ensemble of chains are simulated in a deterministic manner. The initial positions and velocities of all particles in the system are given and a set of potentials is defined. Using the potentials, the force on every particle is calculated. The simulation then integrates through time, calculating the position, velocity, and force at every timestep. This model easily takes into account fluctuations. Additionally, while both Monte Carlo and SCFT simulations primarily look at equilibrium structures, this model primarily looks at kinetics. This can be a large benefit when looking at kinetically trapped features. The drawbacks to this model include the fact this model does not easily calculate free energies and is far more computationally expensive

than SCFT.

CHAPTER 2
MODELING DETAILS

In this chapter the coarse-grained molecular dynamics model used throughout this thesis will be introduced. This will include a description of the model used, a description of typical initial simulation states, and the conditions of typical simulation runs. More detailed explanations will be given in subsequent chapters to explain their unique simulation conditions. Finally, a brief section will be devoted to detailing some common analysis methods used throughout this thesis.

2.1 Coarse-Grained Molecular Dynamics Model

This work is performed using a previously developed coarse grained molecular dynamics model.[30] Polymers are coarse grained such that four monomeric units are combined into one unified atom or bead (as shown in Figure 1.3A). This level of coarse graining was chosen such that each bead represents at least one statistical segment length of many common polymers used in BCPs such as poly(styrene) and poly(methyl methacrylate).

In molecular dynamics, one begins with an initial state (the positions and velocities of all beads in a system) and a set of potential energy expressions (*e.g.* a bond potential). The force that every bead in the system experiences is calculated from is the negative gradient of the potential, as shown by the following equation,

$$\vec{F} = -\nabla V \,, \tag{2.1}$$

where $\vec{F}$ is the force vector and ∇V is the gradient of the potential, V. After calculating the force the acceleration can be determined using Newton's second law, $\vec{F} = m\vec{a}$ where m is the mass of the object and $\vec{a}$ is the acceleration vector. Finally, a step can be taken through

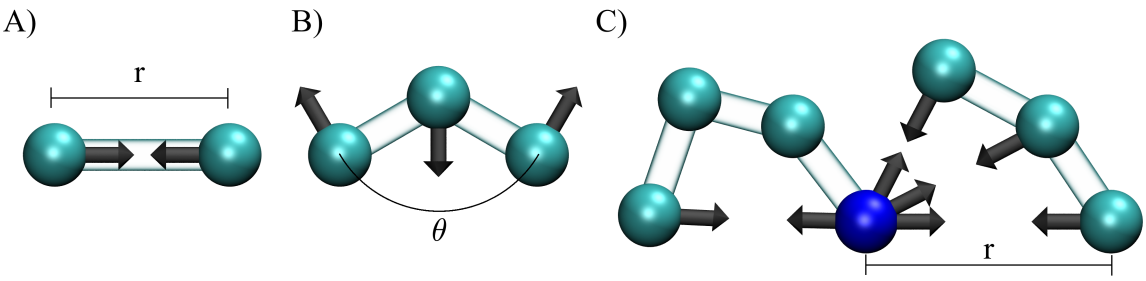

Figure 2.1: The forces from the three basic potentials used in the coarse-grained molecular dynamics model. Dark gray arrows indicate the force vectors. A) The harmonic bond force. B) The harmonic angle force. C) The non-bonded force. The dark arrows here indicate the non-bonded forces from beads interacting with the blue bead.

time by numerically solving the differential equations for the velocity and position. In this thesis the velocity-verlet algorithm is used for integrating the differential equation for each bead.

Three potentials are used in this system, as shown in Figure 2.1. Beads are connected to each other using a harmonic bond potential of the form

$$V_{bond} = \frac{1}{2} \cdot k_{bond} \cdot (r_{eq} - r)^2 \ , \tag{2.2}$$

where V_{bond} is the harmonic bond potential, k_{bond} is the bond force constant, r_{eq} is the equilibrium bond length, and r is the measured length of the bond. For all forcefields in this thesis $k_{bond} = 100$ kcal/(mol nm^2) and $r_{eq} = 0.82$ nm.

Every three consecutively bonded beads has a harmonic angle potential acting on them of the form

$$V_{angle} = \frac{1}{2} \cdot k_{angle} \cdot (\theta_{eq} - \theta)^2 \ , \tag{2.3}$$

where V_{angle} is the harmonic angle potential, k_{angle} is the angle force constant, θ_{eq} is the equilibrium angle between the three beads, and θ is the measured angle. For all forcefields in this thesis $k_{angle} = 5$ kcal/(mol rad^2) and $\theta_{eq} = \frac{2}{3} \cdot \pi$.

A non-bonded potential is present between every pair of beads that are not bonded or

participating in the same angle potential. The form of the non-bonded potential is a Lennard Jones pair potential with 8 and 4 for the exponents as seen in the following equation.

$$V_{ij}(r) = \varepsilon_{ij} \cdot \left[\left(\frac{\sigma_{ij}}{r} \right)^8 - 2 \cdot \left(\frac{\sigma_{ij}}{r} \right)^4 \right] , \tag{2.4}$$

where V_{ij} is the non-bonded potential between beads of type i and j, ε_{ij} is the strength of the non-bonded interaction, σ_{ij} is the radius of the minimum energy, and r is the distance between two beads. The value of the non-bonded potential is zero when beyond a cutoff radius of $R = 4$ nm. The exponents 8 and 4 cause this potential to be "softer" or broader than a typical 12 and 6 Lennard Jones potential. It was found that this broader potential better makes the coarse-grained polymers behave more like the atomistic polymers.

For the majority of this work (with the exception of Chapter 3) $\sigma_{AA} = \sigma_{BB} = \sigma_{AB} = 1.26$ nm and $\varepsilon_{AA} = \varepsilon_{BB} = 0.5$ kcal/mol. The value of ε_{AB} varies depending on the simulation as will be detailed below. The value of the non-bonded potential is zero when beyond a cutoff radius of $R = 4$ nm. These parameters give homopolymers that are roughly equivalent to poly(styrene). Three examples of this non-bonded potentials are shown in Figure 2.2A, while the associated force is shown in Figure 2.2B. The three potentials shown are the potentials used for the density asymmetric BCP in Chapter 3.

The polymers used in this work typically have a degree of polymerization (N) of 64 monomers (16 beads). Each bead in the system has a mass of 418.4 Da.

The value of χ increases proportionally with the difference in like interactions and unlike interactions (indicated by the difference in depth of the energy wells in Figure 2.2), as shown in the following equation.

$$\chi = z \cdot \left[\frac{1}{2} \cdot (\varepsilon_{AA} + \varepsilon_{BB}) - \varepsilon_{AB} \right] , \tag{2.5}$$

where z is the coordination number given by Flory[31, 32] and is effectively a proportionality constant. The value of z is determined in this model by simulating BCPs at various ε_{AB},

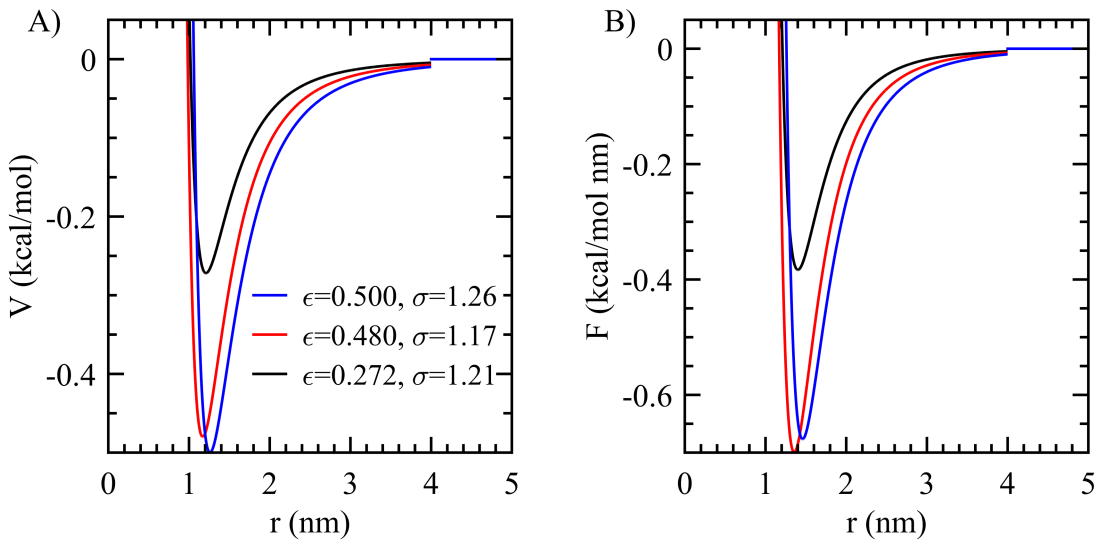

Figure 2.2: A) An example of three non-bonded potentials and B) the associated force.

calculating the resulting scattering profile, then fitting to Leibler's theory to determine χ. Finally, Equation 2.5 is fit to the resulting χ versus ε_{AB} data. This process is detailed more fully elsewhere.[33] For the model parameters listed here, the value of z is approximately 4.3.

Molecular dynamics simulations are run using HOOMD-Blue on an in-house GPU cluster consisting of a mix of Nvidia GTX 580, GTX 680, and Titan Black enabled systems.[34, 35] Simulation results were viewed using either MATLAB[36] or Visual Molecular Dynamics (VMD)[26] utilizing the Tachyon ray tracing library.[27]

2.2 Generating Initial States

There are two primary types of simulations run in this work, bulk simulations and thin film simulations. Bulk simulations are generally used in order to parameterize the BCPs or homopolymers simulated in this work or to extract useful measurements, such as the lamellar repeat distance (domain or pitch) or the density. Thin film simulations are used in order to simulate phenomena interesting to the semiconductor manufacturing industry,

since this is how BCPs will be implemented in their processes. Thin film simulations are composed of two primary parts, a BCP film and an underlayer.

2.2.1 Bulk Simulations

Bulk simulations are generated by first creating a simulation box of the desired dimensions. This box is then filled with randomly placed polymer chains to the desired bulk density. There are instances where chains will be placed unrealistically close together, which is corrected for by a series of two minimizations that will be detailed in Section 2.3.1.

Chains are generated using the following algorithm. First, two beads are created at the equilibrium bond length. The remaining beads of the chain are then added one at a time, each with the constraint that the distance from the previous bonded bead is the equilibrium bond distance and the angle composed of the new bead and the two previous beads is at the equilibrium angle length. This random walk is not self-avoiding, allowing for beads to potentially end up overlapping, which is corrected by the minimizations detailed in Section 2.3.1.

2.2.2 Thin Film Simulations

Thin Film

BCP thin films are generated initially by creating a bulk simulation of the desired dimensions as detailed in the previous section. The z dimension of the simulation box is then increased to a large enough value that beads will not feel the influence of any beads across this boundary. This effectively makes the z dimension of the simulation volume infinite.

Underlayers

There are two types of underlayers used in this work, a brush and a crosslinked mat underlayer. The brush underlayer is formed by generating short, seven bead ($N = 28$) polymer chains composed of the same type of beads as the BCP. These chains are then "grafted" to

a substrate by fixing the position of the end bead in space. All these chain ends are fixed at the same z position, simulating the chain being grafted to a substrate that would be beneath these chains. The chains are initially straight in order to prevent the chains from inverting. The brushes are grafted on a regular square grid with a surface density of 0.44 chains/nm^2. Below these fixed chain ends are another layer of fixed beads that act as an underlayer to help prevent the free end of the brush from inverting during the simulation. These lower beads are placed on a square grid also with a surface density of 0.44 chains/nm^2. These beads are placed offset from the grid the chains are placed on. Brush underlayers are useful for simulating chemoepitaxial guiding underlayers.

In order to simulate a graphoepitaxial guiding underlayer, a second type of underlayer is used. This underlayer is meant to simulate a crosslinked mat underlayer. To generate these underlayers, first a bulk BCP simulation was generated composed of a single long BCP chain. This chain then underwent molecular dynamics for 25 ns to eliminate any density fluctuations. These density fluctuations are spots in the simulation that have a locally higher or lower density than expected due to the random nature of the initial build. The resulting bulk simulation was then "carved" in order to get it to the desired shape by removing beads from undesirable locations. This act of carving will cut the original chain into many smaller chain segments. By doing this, more complicated underlayers can be generated such as ones with topography (for example, Figure 1.6). Generally, the minimum height of the film was set to 4 nm since this is the cut-off for non-bonded interactions. Next, to simulate cross-linking, approximately 20% of the beads in the underlayer were randomly chosen to have their positions fixed in space, meaning these beads cannot move through space when undergoing molecular dynamics. Because removing the beads earlier broke the single chain into many smaller chains, care was taken to make sure every new chain had at least one "cross-linked" bead to prevent the chains from leaving the underlayer. This percent cross-link density was chosen since a higher density of fixed beads can cause a density wave to appear in the BCP film while with a lower cross-link density the film and

underlayer interpenetrate too much.[37]

After generating both a thin film and an underlayer, the thin film is placed on top of the underlayer, as seen in Figure 2.3A. After a brief simulation run, the thin film will collapse down to the underlayer and any unrealistic fluctuations due to the build will damp out, as seen in Figure 2.3B.

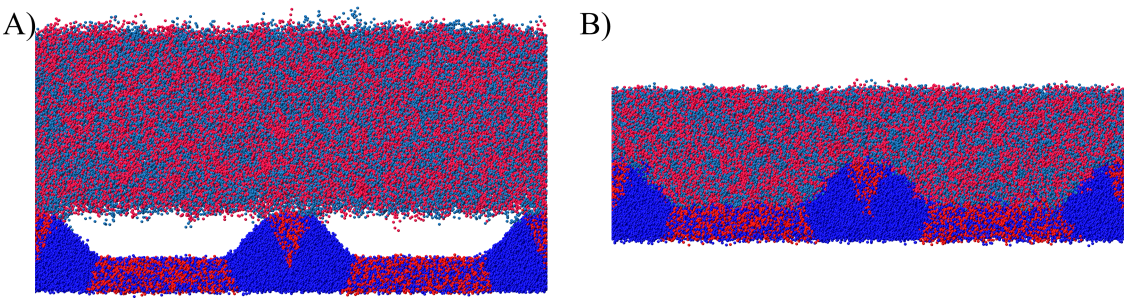

Figure 2.3: Cross-section of the A) an initial build and B) a collapsed state. The underlayer beads are shown in darker blue and red while the film beads are shown in lighter blue and red. Blue indicates A beads, red indicates B beads.

2.3 Typical Simulations

2.3.1 Minimization

Simulations undergo two minimization steps after being built. The first minimization gently pushes apart beads that were placed too close together initially. To do this, σ_{ij} is initially set to a very low value ($\sigma_{ij} = 0.001$ nm) which prevents beads from feeling too high a force from the highly repulsive regime of the non-bonded potential. A series of short minimizations (50 steps each) are run, increasing σ_{ij} by increments of $\Delta\sigma_{ij} = 0.005$ nm in each run until the desired value is reached. Minimizations are run using the HOOMD FIRE (Fast Inertial Relacation Engine[38]) minimizer (parameters: dt=5×10^{-6}, ftol=1×10^{-2}, Etol=1×10^{-7}, finc=1.99, fdec=0.8, alpha_start=0.01, and falpha=0.9).

The second minimization step is a more generic minimizer run at the final parameter values. This minimization runs for 20,000 steps using the FIRE[38] minimizer with parameters dt=5×10^{-4}, ftol=1×10^{-2}, and Etol=1×10^{-7}. In most thin film cases after completing both minimizations a brief simulation is run with $\varepsilon_{AB} = \frac{1}{2} \cdot (\varepsilon_{AA} + \varepsilon_{BB})$ (where $\chi = 0$) for 200,000 timesteps (10 ns) in order to collapse the film to the brush or mat underlayer and allow the film to better equilibrate, eliminating any unrealistic density fluctuations generated during the initial build. The elimination of these density fluctuations can be seen by a decrease and then leveling off of the potential energy, particularly in the non-bonded potential energy.

2.3.2 Simulation Runs

After the two minimization steps, dynamics are run. In order to do this, velocities must be assigned. Here, velocities are assigned randomly such that temperature of the system is initially at the set point ($T = 500K$ typically) and the distribution of the velocities follow the Maxwell-Boltzmann distribution. Simulations are run with either the HOOMD NVT integrator[39, 40] or the HOOMD NPT integrator[39, 41, 42]. For both types of simulation, the integration timestep is 0.05 ps. NVT simulations (constant number of beads, constant volume, and constant temeperature) use a Nosé-Hoover thermostat. The temperature set point is $T = 500$ K, the controller coupling constant is tau = 0.2 timesteps. NPT simulations (constant number of beads, constant pressure, and constant temperature) use an MTK barostat-thermostat. The temperature set point is $T = 500$ K, the temperature controller coupling constant is tau = 2 timesteps, the pressure set point is $P = 1$ atm and the pressure controller constant is tauP = 20.

2.4 Measurements of Bulk Polymer Properties

In order to determine bulk homopolymer properties, a bulk homopolymer simulation is run under NPT conditions. The simulation volume and energy is measured through time

until it is seen that the measured values level off. Once level, the simulation is continued, periodically outputting the positions of all the beads in the system. To determine the density of the simulation the mass of the system is divided by the volume of the system averaged over the final trajectory. To determine the cohesive energy density, total interchain non-bonded potential energy is calculated and divided by the simulation volume. To do this, the total intrachain non-bonded potential energy is subtracted from the total non-bonded potential energy to give the interchain non-bonded potential energy. It was found that using a cutoff corrections for the non-bonded potential had little effect on the cohesive energy density calculations, therefore no cutoff corrections were used.

In order to calculate the pitch or repeat distance of a BCP, a pre-aligned bulk BCP film is run in an NPT simulation. Where normal NPT simulation are run with each of the box dimensions coupled (so all dimensions will proportionally change the same amount when adjusting the volume), these simulations are run with the x dimension moving independently of the y and z dimensions which are coupled. Since the lamellae are oriented such that the repeat distance is in the x dimension and the lamellae themselves are oriented in the y and z plane, the box is able to shrink or grow in the x dimension to account for changes in the pitch. Simulation volumes quickly change to accommodate the correct pitch. This method is found to give equivalent repeat distances to those calculated in previous works by simulating the scattering of the BCP to calculate the pitch.[33]

2.5 Analysis of BCP Films

2.5.1 Generating Images

Most of the analysis done in this work involves the analysis of two dimensional images of simulations. Images are generated by first choosing two dimensions to look at (*e.g.* x and y while averaging through z). Next, a square grid of pixels corresponding to locations in film is generated, generally with a grid spacing of 0.3 nm. At each pixel location, all beads within a set radius (typically 1 nm) of the pixel are found. The number of each type

of bead is then determined (A and B beads in the BCP, C and D beads in the underlayer where C is equivalent to A and D is equivalent to B). The pixel is then given a value based on one of three different number fractions. In most cases the number fraction of A beads in the film is calculated (number of A beads divided by the number of beads in the film). In some cases the number fraction of A beads total is calculated (A and C beads divided by the total number of beads). Finally, in some cases when trying to determine the border between the film and the underlayer, the number fraction of film beads is calculated (A and B beads divided by the total number of beads). These number fractions always have a value between 0 and 1, so images are generated that are grayscale with 0 being mapped to black and 1 being mapped to white. An example of one of these images is seen in Figure 2.4B.

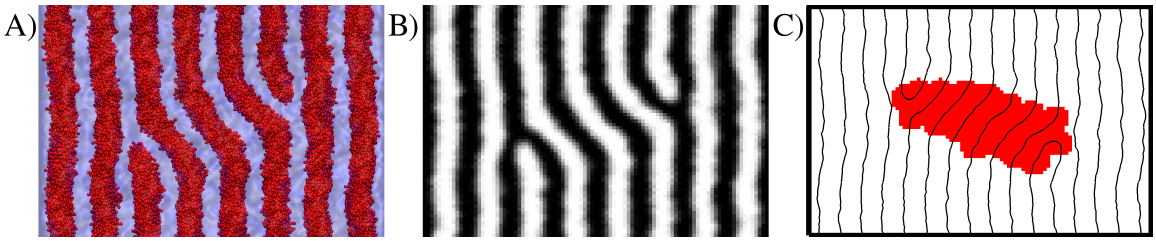

Figure 2.4: A) Simulation state visualized with VMD. Red spheres are A type beads, the blue transparent region are B type beads. B) A two dimensional image generated with MATLAB where each pixel is assigned a value based on the number fraction near the pixel location. White pixels indicate a predominately A region while black pixels indicate a predominately B region, with various shades of gray in between. C) The number fraction = 0.5 contour lines are found. Areas near contour segments that have an angle significantly deviating from a vertical line are considered defective. These defective areas are colored red.

2.5.2 Measuring Defectivity

In order to determine the defectivity of a film after an MD simulation a top down projection (*i.e.* an image of the x and y plane averaging through z) of the simulation was produced, as in Figure Figure 2.4B. Next, contour lines were generated along where the number fraction of A beads in the film was 0.5 in order to trace the interface between the A and B domain, as seen in Figure 2.4C. For well formed, defect free lamellae these contours

should all approximately be in the same direction except for some variation due to line edge roughness. Therefore, any contour that had an angle deviating from the desired angle by $\frac{\pi}{6}$ was noted to be potentially defective. Any pixel that had more than 10 of these potentially defective contour line segments within a $\frac{1}{3} \cdot L_0$ radius was labeled as defective. These are the red colored pixels in Figure 2.4C. After doing this, the defective area fraction was calculated and called the defectivity. The defectivity ranged from 1 (totally defective films) to 0 (defect free, well-aligned vertical lamellae).

2.5.3 Measuring Roughness

Line width roughness (LWR), line edge roughness (LER), and the amount of undercutting and footing in a simulation (referred to here as the variation in line width through depth or VWD) are of interest in lithography since these are known to have a negative effect on device performance.[43] These are the focus of Chapter 5. To measure LER and LWR, first a two dimensional image is calculated in x and y plane. Once the images are generated, the pre-etch edges of the lines are calculated using an arbitrary threshold of where the number fraction of A beads was 0.5 ($n_A = 0.5$). This threshold appears to visually match the line edges. Once the pre-etch lines are determined, LER is calculated by calculating the standard deviation of the line edge. LWR is the standard deviation of the line width (or the difference in two adjacent line edges). While the LER or LWR in a real system would likely change during an etch process, it is assumed that a higher pre-etch LER or LWR will lead to a higher post-etch LER or LWR, allowing the trends reported in this work to be extended to a system with an etch step.

In order to analyze the amount of footing and undercutting in the simulation, the variation in line width through depth (VWD) was calculated. First, the system was analyzed in order to determine which A beads composed the pinned line and which A beads composed the unpinned line. This was done by calculating the center of mass of every chain in the system. Since the center of mass for chains in a well ordered lamellar system falls near

the interface between the A and B domains, this center of mass was to determine whether the A beads on that chain composed the pinned or unpinned line. Once the A beads were assigned to either the pinned or unpinned line, slices were taken through depth. For each slice, the density of A beads in the pinned line, A beads in the unpinned line, and B beads were determined. Using these three bead densities, the volume fraction for each bead type was calculated. Multiplying the volume fractions for each type of A bead by the total repeat distance of the underlayer ($2\ L_0$) then gives the average width of that line type in that slice. It was found that line widths determined using this method were in good agreement with the line widths measured through cross-sectional image analysis, but the data was in general far less noisy.

CHAPTER 3

CHEMOEPITAXIAL GUIDING UNDERLAYERS FOR DENSITY ASYMMETRIC AND ENERGETICALLY ASYMMETRIC DIBLOCK COPOLYMERS

3.1 Introduction

As detailed in Section 1.2, much work is being done to find BCPs with a higher χ parameter to allow lower pitch (L_0) structures to form. BCPs tend to have higher χ values when the blocks interact in dissimilar ways.[12] For example, polystyrene (PS) primarily interacts with itself by dispersion forces, as does poly(methyl methacrylate) (PMMA). However, poly(4-hydroxystyrene) (PHOST) has hydrogen bonding present. Therefore, PS-b-PMMA will likely have a much lower χ ($\chi \approx 0.030$)[44] than PS-b-PHOST ($\chi \approx 0.124$)[45] since PS-b-PHOST is composed of blocks that interact differently.

There has been little modeling research done on BCPs that have density asymmetry or an energetic asymmetry.[46] The majority of modeling research to this point has been done investigating BCPs that are composed of two homopolymers that are identical to each other.[37, 19] Therefore, little is known fundamentally about BCPs composed of blocks that interact in different ways and the effect that such energetic asymmetries has on phase separation or the ability to align BCP films to patterned underlayers. However, it is known to be important since energetically asymmetric BCPs are known to often "skin," preferentially placing the block with the lower cohesive energy density at the free surface.

This is similar to the type of underlayer produced by the LiNe process flow.[47] These are chemoepitaxial guiding underlayer (Section 1.3.2) consisting of a repeating pattern of thin, highly preferential pinning stripes separated by a more neutral background region. Modeling research has been done into these underlayers, though only on BCPs that are symmetric in energy and density.[47, 48, 49] This chapter seeks to explore what problems

might be encountered in the future when using more asymmetric, high χ BCPs.

3.2 Model Description

In order to model these asymmetric BCPs, the parameters for the non-bonded potential (Equation 2.4) are modified. The parameters ε_{ij} and σ_{ij} have large effects on cohesive energy density CED and density (ρ) respectively. Therefore, these values were varied in order to generate three different homopolymers (HPs) which are summarized in Table 3.1. The first HP, HP 1, is the HP typically used in this model. This HP is meant to be roughly equivalent to polystyrene. The second HP described in Table 3.1 was designed to have a similar density to HP 1, but a different CED. The third HP was designed to have a similar CED to HP 1, but a different density.

Table 3.1: Summary of the forcefields for each homopolymer and some resulting properties.

HP	$\sigma_{AA}\,(nm)$	$\varepsilon_{AA}\left(\frac{kcal}{mol}\right)$	$CED\left(\frac{kcal}{mol}\right)$	$\rho\left(\frac{beads}{nm^3}\right)$	$\beta\,(MPa^{-1})$
1	1.26	0.500	12.95	1.37	408
2	1.30	0.537	15.26	1.37	377
3	1.17	0.480	13.20	1.55	469

These HPs were then used to create five diblock copolymers (BCPs), which are summarized in Table 3.2. The symmetric BCP is a BCP where each block is the same homopolymer (HP 1). This is an idealized case where the density and cohesive energy densities of both blocks are identical. Most simulation work to this point has considered idealized BCPs such as this.[37, 19] It should be noted that while the cohesion of HP A with itself is the same as the cohesion of HP B with itself, by altering ε_{AB} there can still be a value of χ present since the cohesion of A with B is lessened. This would be similar to having two blocks that have equivalent cohesive energy densities, but having one block interact primarily through dispersion forces while the other interacts primarily through polar forces

or hydrogen bonding.

Table 3.2: Summary of non-bonded potential parameters for various forcefields and resulting properties.

BCP	HP A	HP B	$\sigma_{AB}\,(nm)$	$\varepsilon_{AB}\left(\frac{kcal}{mol}\right)$	$L_0\,(nm)$	$\frac{CED_A}{CED_B}$	$\frac{\rho_A}{\rho_B}$
Symmetric	HP 1	HP 1	1.26	0.325	12.41	1.00	1.00
$\text{CED}_A < \text{CED}_B$	HP 1	HP 2	1.28	0.345	12.43	0.85	1.00
$\text{CED}_A > \text{CED}_B$	HP 2	HP 1	1.28	0.345	12.43	1.18	1.00
$\rho_A < \rho_B$	HP 1	HP 3	1.21	0.272	12.83	0.98	0.88
$\rho_A > \rho_B$	HP 3	HP 1	1.21	0.272	12.83	1.02	1.13

The next two BCPs are formed using HP 1 and HP 2 which have a cohesive energy density mismatch. The CED ratio here is in the range of many BCPs, though relatively small in comparison to some high χ BCPs. However, this allows the BCP to be simulated without needing to add a topcoat, which greatly simplifies the system.

The final two BCPs are formed using HP 1 and HP 3 which have a density mismatch. The density mismatch is similar to that found between polystyrene and poly(methyl methacrylate). There is also a small difference in the CED of these two HPs. However, since the CED ratio (1.02) is very close to one, it is assumed that the trends observed for these BCPs will be primarily due to the larger difference in densities which have a ratio of 1.13.

All block copolymers were made using a degree of polymerization (N) of 64 monomers (16 beads). Each block of the BCP typically has a degree of polymerization of 32 monomers (8 beads). However, Sec. 3.3.4 and Sec. 3.3.5 both include polymers with varying volume fraction. In these cases, the minority block has 28 monomers (7 beads) and the majority block has 36 monomers (9 beads). The mass of each bead in the system is $418.4Da$.

The value of ε_{AB} was chosen for all BCPs in Table 3.2 such that χ has a value of 0.78 and χN has a value of 50. While this value of χ is high in comparison to many BCPs in use now,[12] it allows for a smaller degree of polymerization while still maintaining a

reasonable value of χN. This makes the simulated BCP have a smaller domain size which in turn allows for smaller simulation volumes and quicker simulation run times. While having a higher χ, lower N will likely alter the absolute defectivity, there should be little effect on the relative defectivity within a series as is discussed in this work.

The underlayers in this work are brush underlayers (Section 2.2.2). In order to simulate a chemoepitaxial guiding underlayer, a pinning stripe is patterned into the brush underlayer by making all the beads in a particular region bead type A, or a number fraction, $n_{A,pinning}$, of 1. Unless otherwise mentioned, the width of the pinning stripe is $0.5\ L_0$. Separating pinning stripes is a background region in which beads are assigned randomly between types A and B such that the overall number fraction of the background region ($n_{A,background}$) is at some set value which is varied in this paper. The background region is always sized so that the overall pattern pitch is $W_{pattern} = W_{pinning} + W_{background} = 2\ L_0$, making the pattern a density doubling pattern.

Well mixed thin films are generated (Section 2.2.2). All simulations were built with x and y dimensions of $6\ L_0 \times 6\ L_0$ where L_0 is the pitch of the BCP as reported in Table 3.2. The thickness of the films is either $0.5\ L_0$, $0.75\ L_0$, or $1.0\ L_0$ depending on the simulation.

Once both minimization steps are complete (Section 2.3.1), the full simulations (Section 2.3.2) are run. These simulations are NVT simulation and are run in two stages. First, the films are run 10 ns (200,000 timesteps) with $\varepsilon_{AB} = \frac{1}{2} \cdot (\varepsilon_{AA} + \varepsilon_{BB})$ (where $\chi = 0$) in order to relax out any unrealistic density fluctuations from the initial build. Second, simulations are run 100 ns (2,000,000 timesteps) with the appropriate ε_{AB} or χ allowing phase separation to occur. After the simulation is completed, the defectivity of the film is measured (Section 2.5.2). Nine replicates are run for each simulation in this work, and the defectivity is averaged over the nine replicates to report.

3.3 Results and Discussion

3.3.1 Defectivity Versus Background Region Composition

Simulations were run for a symmetric BCP of thickness $0.5\ L_0$ on a patterned underlayer with an A pinning stripe ($n_{A,pinning} = 1$). The composition of the background region of the underlayer, $n_{A,background}$, was varied and the defectivity of the resulting film was measured. This data is reported in Fig. 3.1. Four different regimes are observed in this data as will be described below. The general shape of the curve in Fig. 3.1 and the four regimes/morphologies described here are seen in all the following series of simulations.

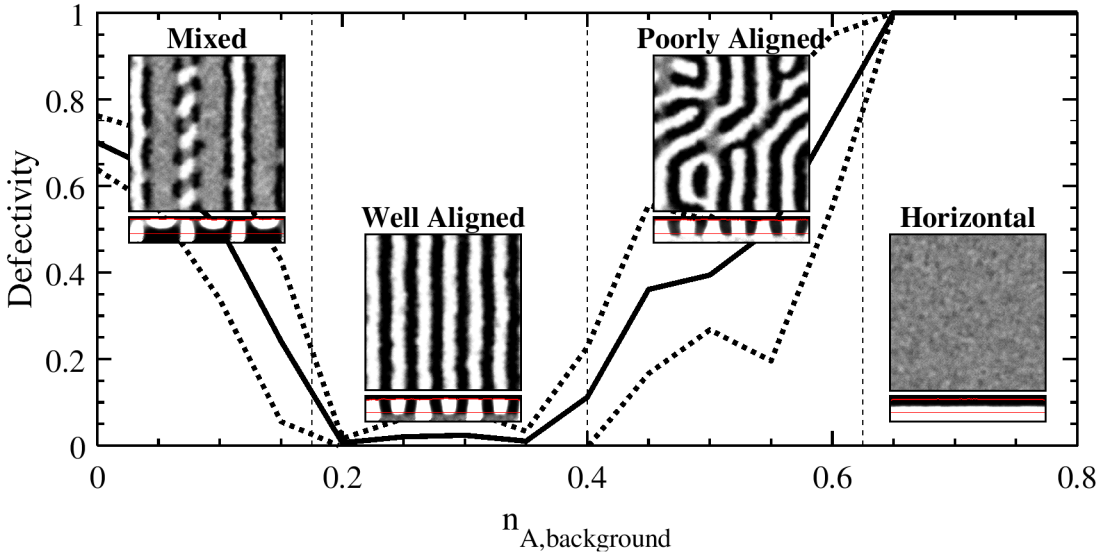

Figure 3.1: The measured defectivity for a symmetric BCP film of thickness $0.5\ L_0$ on a series of underlayers with $n_{A,pinning} = 1$ and a varying $n_{A,background}$. The average defectivity is shown by the solid black line while the single standard deviation errorbars are shown by the dotted line. Four different regimes of film morphology are observed, a mixed lamellae morphology at low $n_{A,background}$, a well-aligned vertical lamellae morphology, a poorly aligned vertical lamellae morphology, and a horizontal lamellae morphology. Examples of these four morphologies are shown in the inset images, with the top image being a top-down view and the bottom being a cross-sectional view. The bottom red line in the cross-sectional view indicates the approximate interface of the brush underlayer and the film while the top red line indicates the approximate location of the free interface.

First, at high background composition, $n_{A,background} \rightarrow 1$, the BCP film is in a regime

where it forms a horizontal lamellae morphology. In this regime, the underlayer is predominately A beads since the composition of the pinning stripe is also $n_{A,pinning} = 1$. Therefore, the film forms horizontal lamellae sheets with the A block wetting the underlayer. Within this regime the defectivity typically has a value of 1.

As the background region composition is decreased, eventually a point is reached where vertical lamellae can form. However, since there is very little contrast between the pinning stripe ($n_{A,pinning} = 1$) and the background region, the underlayer gives very little guidance to the film. Therefore, instead of forming well-aligned lamellae, the resulting film is more reminiscent of a fingerprint pattern. For this reason, this regime is referred to as poorly-aligned vertical lamellae. Defectivity in this region is very high at high background region compositions but decreases as $n_{A,background}$ decreases. This decrease is due to an increase in the contrast in the background region and the pinning stripe. Having a high contrast between the background region and the pinning stripe causes there to be a high energetic penalty for the wrong type lamellae to be over the wrong region. For example, there is a high energetic penalty when a B type lamellae is above an A type pinning stripe. Eventually there comes a point as $n_{A,background}$ decreases that there is enough contrast to essentially eliminate all defects. This is the well-aligned vertical lamellae regime, and is ultimately the target in the underlayer design process.

However, moving past this where $n_{A,background} \rightarrow 0$ a final regime is entered where the film forms a mixed lamellae (ML) morphology, as has been observed elsewhere in the literature.[19] An example of this phase is shown in Fig. 3.1. In this regime the film is attempting to simultaneously form both horizontal lamellae with the B block wetting the underlayer above the background region and vertical lamellae near the pinning stripe. The driving force for the formation of the horizontal lamellae is the highly preferential background region, while the driving force for the vertical lamellae is the high contrast between the background region and the pinning stripe. This contrast offers very strong guidance for BCP chains in the vicinity of the pinning stripe/background region interface,

strong enough to counteract the predominately B underlayer.

It is helpful to categorize defects as one of two types, line defects and morphological defects. Line defects are defects such as jogs or dislocation pairs that exist in vertical lamellae. These are the sorts of defects that exist in the well aligned and poorly aligned vertical lamellae regimes. These line defects decrease with more guidance/constrast in the system, meaning they decrease as $n_{A,background}$ decreases. However, there also exist morphological defects. These are defects where the BCP is forming an incorrect morphology (*e.g.* mixed horizontal and vertical lamellae). These morphological defects occur at extreme values of $n_{A,background}$.

The most desirable background composition will be one that minimizes line defects while still preventing all morphological defects. This composition will be the lowest $n_{A,background}$ that still prevents the formation of the mixed horizontal and vertical lamellae morphology. This implies that one way to decrease defectivity is to destabilize the mixed lamellae morphology. If the mixed lamellae morphology is less stable, it will not form until even lower values of $n_{A,background}$. This allows lower values of $n_{A,background}$ to be reached while still forming vertical lamellae, further decreasing the number of line defects. In later sections it will be suggested that this can be done by altering the film thickness or by altering the volume fraction of the BCP.

3.3.2 Pinning Stripe Width

Simulations were run to calculate the defectivity versus background composition curves for three different pinning stripe widths for symmetric BCPs. The films were all $0.5\ L_0$ thick and had a volume fraction of $\phi_A = 0.5$. These results are shown in Fig. 3.2. All pinning stripe widths measured here other than $W_{pin} = 0.62L_0$ have very similar defectivity windows. Though, the simulation series with a pinning stripe of $W_{pin} = 0.5\ L_0$ may have a slightly larger window for well-aligned vertical lamellae than the other three. While this may be due to the width of the pinning stripe being commensurate with the width of

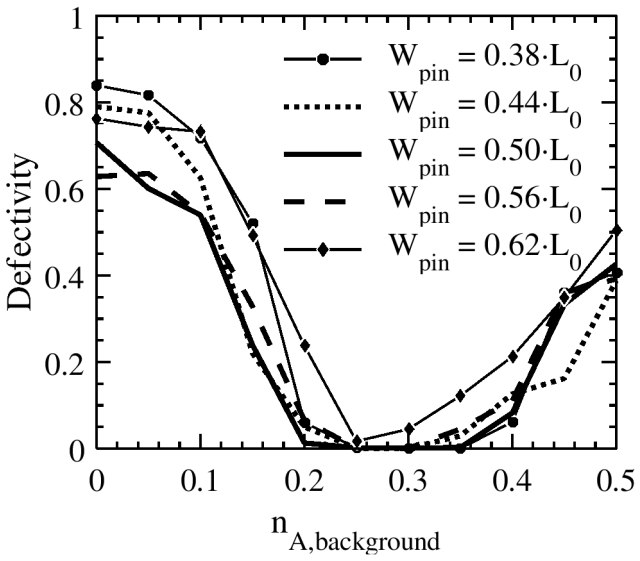

Figure 3.2: Defectivity measurements for a five different pinning stripe widths (W_{pin}) while varying the background region composition ($n_{A,background}$). BCP films are symmetric in energy and density with a volume fraction $\phi_A = 0.5$.

one lamellae, the difference is ultimately very slight and likely within noise. On the other hand, when significantly oversizing the pinning stripe ($W_{pin} = 0.62\ L_0$) the defectivity increased for all background compositions. Morphological defects appeared to occur at higher background compositions than in the other cases ($n_{A,background} = 0.20$ instead of 0.15 for the others). Additionally, in the vertical lamellae never got to as low a defectivity. However, this pinning stripe is fairly large (25% larger than the best case here of $W_{pin} = 0.5\ L_0$). When only 12.5% oversized, the pinning stripe had little effect on the defectivity. This suggests that this process is fairly tolerant of variations in the pinning stripe.

3.3.3 Film Thickness

The effect of film thickness on the defectivity of a symmetric BCP film was explored. The results for three different film thicknesses, t, are shown in Fig. 3.3. First, it takes longer for the influence of the underlayer to propagate through the thickness of the film. This is likely due to the simulations all being run the same length of simulation time (100 ns)

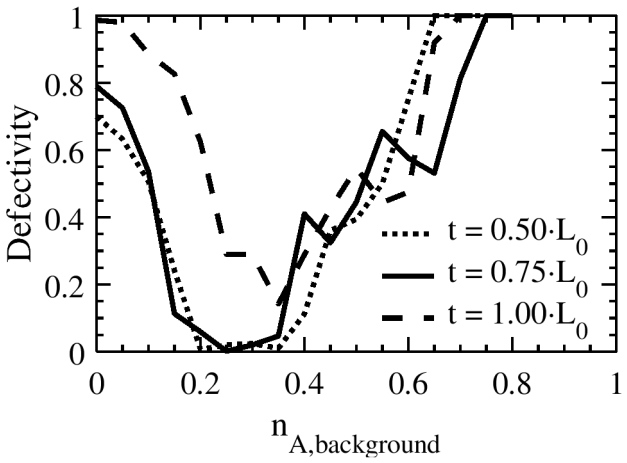

Figure 3.3: Defectivity measurements for a symmetric BCP with three different film thicknesses, t.

when thicker films typically require more simulation time on average to reach a stable state. Thicker films require more time for two main reasons. First, it takes longer for the influence of the underlayer to propagate through the thickness of the film. Second, and related to the first, since initially the films will phase separate before the tops of the film feel the effect of the underlayer, the top of the thick films are likely to initially form a more highly defective state. This initially defective state then takes more time to anneal out, particularly since it is only indirectly influenced by the underlayer. While this makes it difficult to compare quantitatively between film thickness, one can still consider qualitative differences between the trends.

The window for forming well-aligned vertical lamellae is larger for $t = 0.75\ L_0$ than $t = 1.00\ L_0$. This can be explained by looking at the level of frustration in the two respective films. When a lamellae film is a thickness of $n/2\ L_0$, where n is some integer, the film is considered to not be frustrated. This is because at these film thicknesses there exists a possible configuration where the chains pack at the appropriate density to form horizontal stacked lamellae without any islands and/or holes present. However, if the film is frustrated, such as in the $t = 0.75\ L_0$ case, no such configuration exists, causing any horizontal lamellae morphology to consist of islands and/or holes. For a symmetric BCP,

these islands and/or holes are unfavorable since they increase the interfacial area between the BCP film and the free surface. Increasing this interfacial area increases the free energy because beads at the free interface have less beads in close proximity, both because there is a slight decrease in density near the free interface but also because there is a vacuum above these beads. This equates to the beads near the free interface participating in less attractive non-bonded potential pairs, increasing their enthalpy.

Looking only at the contribution of the free interface to the free energy of a symmetric BCP film, varying the film thickness should have no effect on the free energy of the vertical lamellae morphology. This is because the vertical lamellae morphology can form a flat surface at any film thickness. However, the film thickness has a large effect on the horizontal lamellae morphology since a commensurate film can form a flat surface while an incommensurate film must form islands and/or holes. Since the mixed lamellae morphology has a horizontal lamellae component, it too will have a higher free energy when at an incommensurate film thickness. Because of this increase in the free energy of the mixed lamellae morphology, a larger driving force to form mixed lamellae must be present before the film enters that state. Therefore, having an incommensurate film thickness allows a more preferential background region, which in turn allows for lower line defectivity to be present.

The more interesting comparison in this data is between $t = 0.50\ L_0$ and $t = 1.00\ L_0$. Since both of these films have an equal level of frustration one would expect both films to behave similarly. However, while these two films behave in a similar manner at higher background compositions, at low background compositions $t = 0.50\ L_0$ behaves more like the $t = 0.75\ L_0$ case. The mixed lamellae morphology is inherently a high energy state. This morphology has more intrinsic BCP interfacial area than any other, and therefore is resisted. With the increased film thickness, $t = 1.00\ L_0$ is far better suited to disperse this energy than $t = 0.50\ L_0$. Therefore, $t = 0.50\ L_0$ resists forming the mixed lamellae morphology until even lower background region compositions.

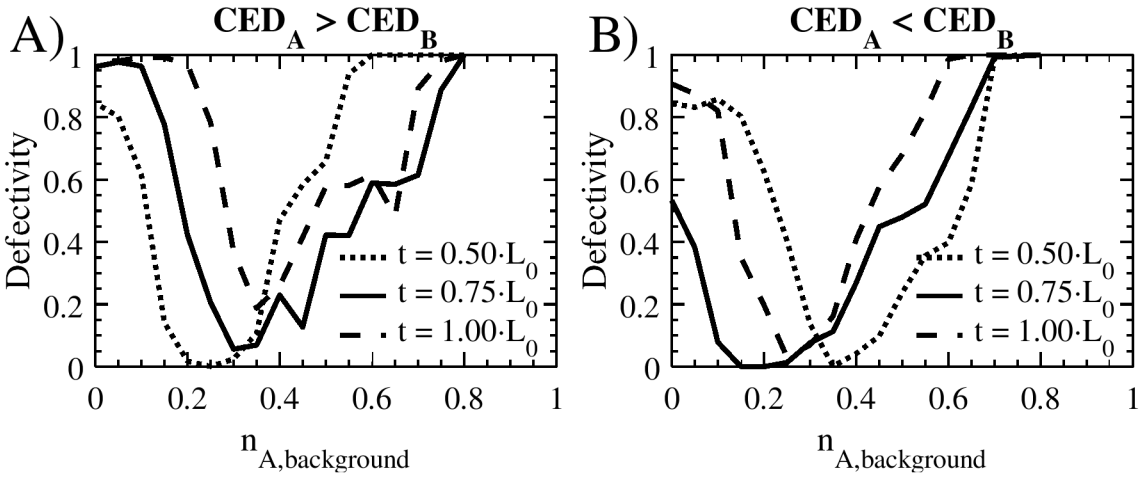

Figure 3.4: Defectivity measurements for two CED asymmetric BCPs while varying film thickness, t.

A BCP that is asymmetric in cohesive energy density (CED) is considered next. Simulations were run in order to determine the window for well-aligned vertical lamellae for three different film thicknesses. These results are shown in Fig. 3.4 for both the case where $\text{CED}_A > \text{CED}_B$ and $\text{CED}_A < \text{CED}_B$ (where the pinning stripe is always A).

In both of these cases, film thickness plays a major role in the location of the well-aligned vertical lamellae window, as has been discussed previously for unpatterned underlayers.[46] This can largely be explained by considering the role the free surface now plays in DSA. With the symmetric BCP, neither block preferred the free surface since the CEDs of the two blocks matched. However, now that there is a mismatch in CED the block that is lower in CED will preferentially go to the surface. As discussed earlier, beads at the free interface experience less attractive interactions with beads in the film. Because of this, there is a larger energetic penalty to place the higher CED block at the free surface since there will be a greater loss of attractive interactions than if the lower CED block were at the free surface. This effect causes the CED asymmetric BCP to skin if the CED ratio is high enough. The drive to skin has a large effect on what morphology forms at what background region composition.

A film of thickness $t = 0.5 \cdot L_0$ allows for three possible non-mixed lamellar config-

urations without islands or holes: vertical lamellae, horizontal lamellae with the A block down (denoted as AB), and horizontal lamellae with the B block down (BA). Looking at just the free interface, when $\text{CED}_A > \text{CED}_B$ the AB configuration will be the most stable morphology since it places the lower CED block at the free surface. To counteract this free interface driving force, the underlayer will need to be more preferential to B type beads (lower $n_{A,background}$) in order to form vertical lamellae instead of the AB configuration. Therefore, for $\text{CED}_A > \text{CED}_B$ (Fig. 3.4A) the window for $t = 0.5 \cdot L_0$ will shift to the left. On the other hand, since $\text{CED}_A < \text{CED}_B$ (Fig. 3.4B) will have a more stable BA morphology, its window would have to shift to higher compositions (to the right).

In a similar way, with a film thickness of $1 \cdot L_0$ there are three possible non-mixed lamellar configurations without islands or holes: vertical lamellae, horizontal lamellae with A on both the top and bottom (denoted as ABBA), and horizontal lamellae with B on both the top and bottom (BAAB). In this case for $\text{CED}_A > \text{CED}_B$ the CED makes BAAB the more stable configuration since it places the lower CED block at the free surface. Therefore, unlike the $t = 0.5 \cdot L_0$ case, the window will shift to a higher background composition.

Comparing between $\text{CED}_A < \text{CED}_B$ and $\text{CED}_A > \text{CED}_B$ for a film thickness of both $t = 0.75 \cdot L_0$ and $t = 1.00 \cdot L_0$, it can be seen that $\text{CED}_A < \text{CED}_B$ reaches a far lower defectivities within its window. This is due to the window of $\text{CED}_A < \text{CED}_B$ being shifted to the left, where there is more contrast between the pinning stripe and the background region. This supports the idea that line defects continue to decrease as more contrast is introduced into the system.

The fact the low defectivity window shifts in opposite directions for films of thickness $n \cdot L_0$ and $(n + 1/2) \cdot L_0$ shows that with a CED asymmetric BCP, the stability of the mixed lamellae morphology has a large dependence on film thickness. Therefore, with the proper choice of pinning stripe and film thickness, one can design an underlayer with far greater guidance while still forming vertical lamellae, thus eliminating more line defects. The ideal cases would be either a film with a higher CED pinning stripe and a film thickness

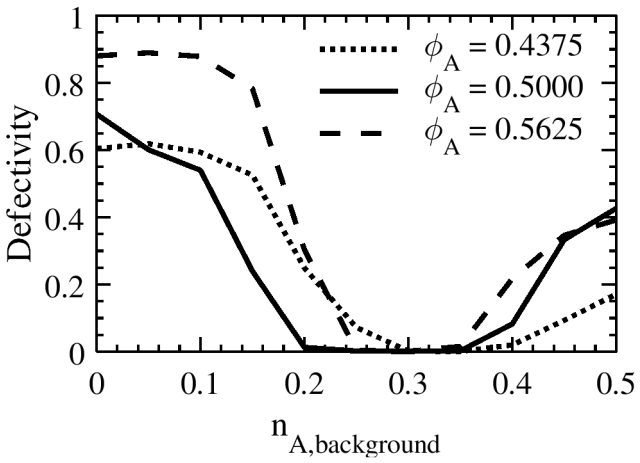

Figure 3.5: Defectivity measurements for a BCP that is symmetric in energy and density, but with varying volume fraction ϕ_A for a film thickness of $t = 0.5 \cdot L_0$.

of $(n + 1/2) \cdot L_0$ or a lower CED pinning stripe and a film thickness of $n \cdot L_0$. While more work needs to be done to confirm the theory, it is hypothesized here that a higher CED pinning stripe will perform better than a lower CED pinning stripe. This thought because a higher CED pinning stripe should provide stronger guidance to the associated lamellae.

3.3.4 Volume Fraction Asymmetry

The volume fraction of a symmetric BCP film was varied. Simulations were run with three film volume fractions, ϕ_A, for a $0.5 \cdot L_0$ thick film on an underlayer with a pinning stripe of $W_{pin} = 0.5 \cdot L_0$. In Fig. 3.5 it can be seen that the volume fraction of the film has a fairly large effect on the defectivity profile. Shifting the volume fraction away from $\phi_A = 0.5$ causes the mixed lamellae regime to extend to higher background compositions. Additionally, it is observed that the well-aligned vertical lamellae regime when $\phi_A = 0.4375$ extends to higher background compositions, and then when the defects start appearing they appear at a slower rate.

It is hypothesized that having a volume fraction other than $\phi_A = 0.5$ increases the kinetics of defect annihilation. It has been shown that a key step in annealing out many

common defects is the formation of a bridge of one domain across another.[50] When $\phi_A < 0.5$ the A lamellae will be more narrow while the B lamellae will be wider. Related to this, the A portion of the chains will be shorter while the B portion of the chain will be longer. With these two facts in mind, there are two ways a volume fraction of $\phi_A < 0.5$ could increase bridge formation. First, the shorter A portion of a chain will be easier to drag through a B domain, though the B domain is wider which may counteract the effect. Second, the longer B chain, while likely harder to drag through an A domain, does not have to be dragged as far since the A domain is narrower.

While it is out of the scope of this paper to work out all the intricacies of this situation, a brief proof of concept was tested. A proxy for bridge formation, and therefore the kinetics of defect annihilation, is a count of how many times a BCP chain, which is typically centered on a lamellar interface, jumps from one interface to an adjacent one. For a chain to jump interfaces it is necessary for one portion of its chain to be dragged through an unfavorable domain (e.g. the A block must pass through the B domain). In order to measure this rate defect-free thin film simulations were built. These films had dimensions of $2 \cdot L_0$ x $6 \cdot L_0$ x $0.5 \cdot L_0$ and were built on a 2x density multiplying underlayer with an A preferential pinning stripe and a background region of $n_{A,background} = 0.5$. Due to these chain jumps being rare, fifty replicates were run for 100 ns each. The positions were recorded every 5 ns, with the final 80 ns of the simulation being analyzed to see when the center of mass of a chain jumped from one interface to another. The results are shown in Table 3.3.

It can be seen that the minority block is far more likely to cross over the majority domain. This supports the explanation that a shorter portion of a chain can jump easier despite it needing to jump a longer distance. Also, it shows that a volume fraction other than $\phi_A = 0.5$ does have increased jumping rates significantly since $\phi_A = 0.5$ had approximately a third of the chain jumps that either of the other volume fractions had. This suggests bridge formation would likely be easier for these polymers. While this is not a perfect proxy for defect annihilation, it does suggest defect annihilation may be improved

Table 3.3: Counts of chains jumping from one interface to another in thin film defect free lamellae simulations. Columns N_A and N_B show the number of A beads and B beads per chain. Columns A (pin), A (back), and B indicate the number of chains jumping across the A domain above the pinning stripe, the A domain above the background region, and the two B domains above the background region.

ϕ_A	N_A	N_B	A (pin)	A (back)	B	Total
0.4375	7	9	4	0	17	21
0.5000	8	8	4	1	2	7
0.5625	9	7	10	9	0	19

by having a volume fraction other than $\phi_A = 0.5$. This is supported further by data in Sec. 3.3.5. However, it is unclear why the defectivity in the case of $\phi_A = 0.5625$ does not decrease as it did in $\phi_A = 0.4375$. This may be due to the presence of the pinning stripe, as it can be seen that chains appear more likely to jump across the A domain located above the pinning stripe rather than the A domain located above the background region.

The BCP film with a volume fraction of $\phi_A = 0.5$ forms well-aligned vertical lamellae at far lower background region compositions than the other two BCP films. This is due to each of these three BCP films forming a slightly different mixed lamellae morphology, as shown in Fig. 3.6. These morphologies are seen when the underlayer is composed of a background region that is sufficiently preferential to B with an A preferential pinning stripe. While these morphologies do occur at other background preferences, they are the most clear with the strong guidance of $n_{A,background} = 0$, the case shown in Fig. 3.6. When the A block (white) is the minority block in the film ($\phi_A = 0.4375$), the mixed lamellae (ML) morphology looks more lamellar. The vertical lamellae above the pinning stripe forms very well with a half lamellae of black on either side of the white lamellae. On the other hand, when the A block is the majority block ($\phi_A = 0.5625$), a different, more cylindrical morphology forms. Near the underlayer/film interface there is good registration of the film with the underlayer pattern as in the earlier case. However, further from the underlayer interface instead of the B domain forming half lamellae, a more cylindrical

shape is formed. This is at least in part due to B being the minority phase, so it can form the cylinders while the A phase forms the matrix around it. Interestingly, these cylinders appear to be roughly half-cylinders, meaning they have more of a semi-circular cross-section. This is due to the chains that compose the cylinders being primarily contributed by the vertical lamellae portion of the film with little contribution from the horizontal region. Because the cylinders are only gaining mass from one side, there is effectively a lower local volume fraction of B in this area than there are for typical cylinders. This helps explain why a lamellae forming BCP with a volume fraction well inside the lamellae phase on a typical phase diagram[6] might have cylindrical components in its morphology. The placement of these B type half cylinders tends to be staggered across the vertical lamellae, causing the vertical lamellae to waver from side to side to accommodate When the volume fraction of the film is $\phi_A = 0.5000$, the film seems to be transitioning between these other two morphologies.

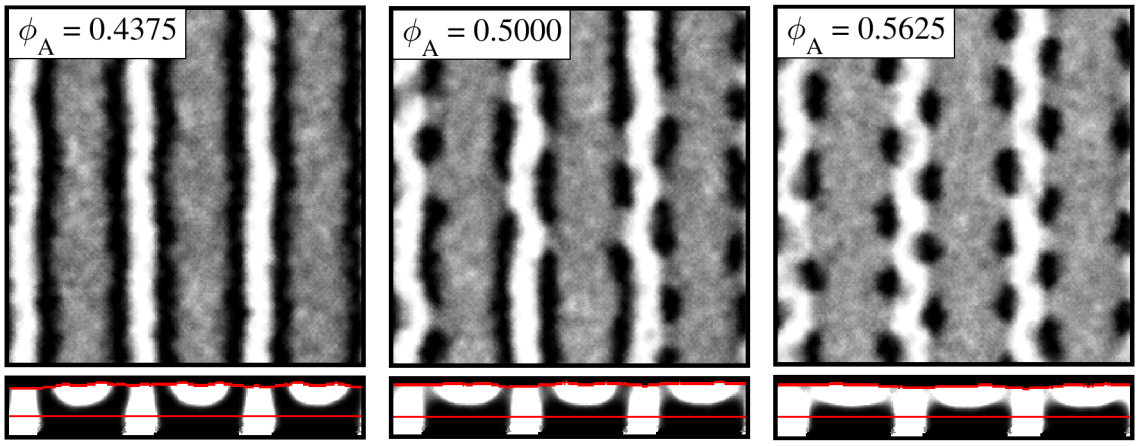

Figure 3.6: Top down and cross-sectional images of simulations for a symmetric BCP film of thickness $0.5 \cdot L_0$ with varying film volume fraction on an underlayer with $n_{A,background} = 0$ and $n_{A,pinning} = 1$. The A block is indicated by white, the B block by black. Both the approximate interface between the film and the underlayer and the interface between the film and the free surface are indicated by red lines.

When $\phi_A = 0.4375$ the lamellar form is more stable, meaning it has a lower free energy, while when $\phi_A = 0.5625$ the cylindrical form has a lower free energy. On the other

hand, when $\phi_A = 0.5000$ it is suspected that the lamellar form and the cylindrical form have similar free energies leading to this hybrid state. More importantly, it is hypothesized that the free energy of this hybrid state for $\phi_A = 0.5000$ is higher than the free energy of either the lamellar form for $\phi_A = 0.4375$ or the cylindrical form for $\phi_A = 0.5625$. If true, this hypothesis would suggest that when $\phi_A = 0.5000$ a greater driving force in the underlayer is required in order to form the ML morphology instead of the well-aligned vertical lamellae morphology. This allows more preferential background regions to be utilized while still forming well-aligned vertical lamellae, as is the case for $\phi_A = 0.5000$ in Fig. 3.5. The more preferential background region drives down line defects that arise from poor guidance.

It should be noted that the measure of defectivity used in this paper will gives a higher value for the cylindrical ML morphology than for the lamellae ML morphology. This is because the lamellar ML morphology has a very well formed vertical lamellae above the pinning stripe which give a low defectivity measurement. On the other hand, the lamellae over the pinning stripe in the cylindrical ML morphology wavers much more, giving a larger defectivity measurement. This can be seen in Fig. 3.5 when $n_{A,background} \to 0$ where the measured defectivity of $\phi_A = 0.4375$ is significantly lower than that of $\phi_A = 0.5625$.

These mixed lamellae morphologies were found for a thin film ($t = 0.5 \cdot L_0$). Thicker films form different, more complex morphologies than these. While these thicker film morphologies are not explored in depth here, it will be shown in Sec. 3.3.5 that the transition volume fraction found for a thin film ($t = 0.5 \cdot L_0$) also shows improvement in the defectivity of a thicker film ($t = 0.75 \cdot L_0$). This suggests that while the transition volume fraction may change with film thickness, it is likely a minor change.

To summarize this section, the free energy of the mixed lamellae morphology is dependent on the volume fraction of the BCP film. This allows the volume fraction to be tuned such that the mixed lamellae will be less stable, allowing for more guidance in the system to decrease line defects without increasing morphological defects. For a symmetric BCP

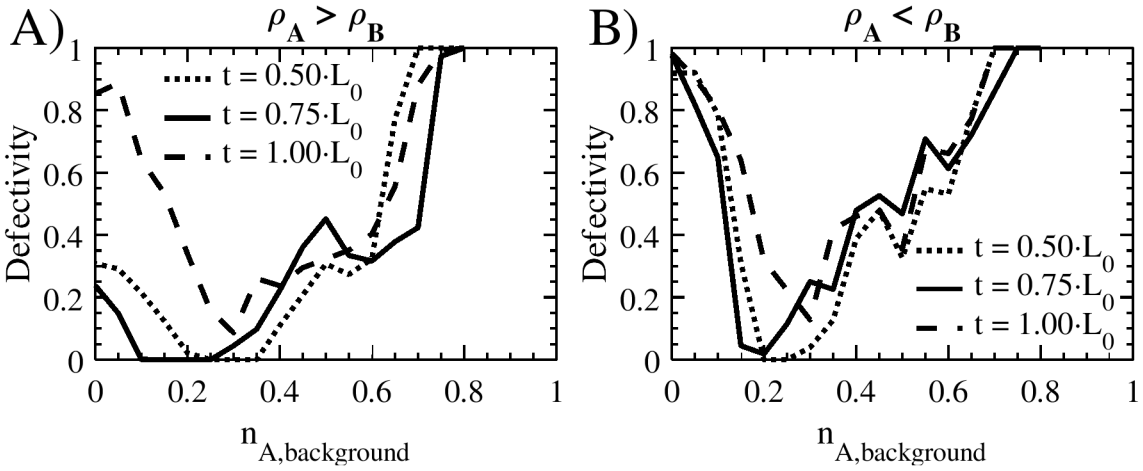

Figure 3.7: Defectivity measurements for two BCPs with a mismatch in density between the blocks while varying film thickness, t.

the ideal volume fraction is found to be approximately $\phi_A = 0.5$.

3.3.5 Density Asymmetry

A BCP that has a mismatch in density is considered next. The ratio of densities in these BCPs are similar to that found in poly(styrene)-b-poly(methyl methacrylate). The results for various thicknesses of this BCP are shown in Fig. 3.7 for both density asymmetric cases, $\rho_A > \rho_B$ and $\rho_A < \rho_B$ (where the pinning stripe is always A). In both cases, it can be seen that films with a thickness of $0.75 \cdot L_0$ can form well-aligned vertical lamellae at lower background compositions due to the film thickness being incommensurate with the pitch. This is similar to how the symmetric BCP responded to thickness changes in Sec. 3.3.3. Because the dependence on film thickness is similar to the symmetric BCP (with the same CED for each block), the small difference in CED present in the density asymmetric BCPs is likely negligible in comparison to the difference in densities.

When $n_{A,background} \rightarrow 0$ the defectivity of $\rho_A > \rho_B$ reaches far lower values than $\rho_A < \rho_B$. This is because $\rho_A > \rho_B$ forms the more lamellar form of the mixed lamellae morphology, while $\rho_A < \rho_B$ forms the more cylindrical form as discussed in Sec. 3.3.4.

The formation of the two different morphologies here is not driven by volume fraction which is roughly 0.47 and 0.53 for $\rho_A > \rho_B$ and $\rho_A < \rho_B$ respectively. Rather, it is believed in this case to be driven by the difference in compressibilities of the two blocks, as shown in Table 3.1 for homopolymers 1 and 3. The half-cylinder morphology is preferred in the case where the B block is more compressible (higher density), while the half-lamellae morphology is preferred when the B block is less compressible. However, the opposite morphology can be formed by varying the volume fraction of the BCP.

In Sec. 3.3.4 it was shown that $\phi_A = 0.5$ is the composition for a symmetric BCP where the mixed lamellae (ML) morphology transitions between the cylindrical and lamellar morphology, and it was hypothesized that this was the least stable ML morphology. For $\rho_A > \rho_B$ and $\rho_A < \rho_B$ this transition region is roughly at $\phi_A = 0.59$ and $\phi_A = 0.41$ respectively. The typical simulation series was run for both of these BCPs for both a film thickness of $t = 0.50 \cdot L_0$ and $t = 0.75 \cdot L_0$, the results of which are shown in Fig. 3.8. It can be seen that the change to the volume fraction did appear to improve the process window. The fact that a volume fraction that is being greatly shifted away from $\phi_A = 0.5$, which was the ideal volume fraction in Fig. 3.5, helps support the proposed hypothesis. It is also worth noting that while this hypothesis was developed looking at thinner films ($t = 0.5 \cdot L_0$), it is remarkable that $t = 0.75 \cdot L_0$ films were also drastically improved by choosing this alternate film volume fraction. This suggests that this volume fraction is either independent or only weakly dependent on the thickness of the film. For both film thicknesses and both BCPs looked at here, the region where the defectivity measures as non-existent appears to be wider. Additionally, when moving away from the defect free vertical lamellae region, the defectivity increases at a slower rate. Near the mixed lamellae morphology region this can be partially accounted for by the different morphology having a different base defectivity. However, it should be noted that the defectivity also increases at a slower rate in the poorly-aligned lamellae region. As discussed in Sec. 3.3.4 for a BCP that did not have a density mismatch, having a volume fraction other than $\phi_A = 0.5$ appears

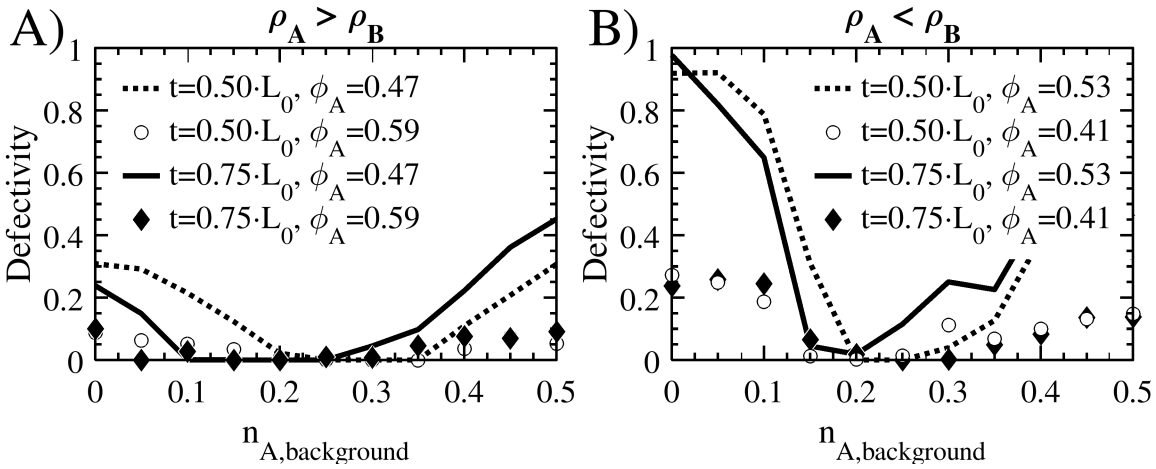

Figure 3.8: Simulation results for density asymmetric BCPs at different volume fractions and film thicknesses. Volume fractions near $\phi_A = 0.5$ are shown by the solid and dashed lines while volume fractions near the transition between ML morphologies are shown by circles and diamonds.

to increase chain jumping, which likely results in faster kinetics of defect annihilation.

3.4 Conclusions

A coarse-grained molecular dynamics model was used to explore how various block copolymers self-assemble on various guiding underlayers. It was found that as the background region composition is varied in the underlayer, films go through four primary morphologies: mixed lamellae (ML), well-aligned vertical lamellae, poorly aligned vertical lamellae, and horizontal lamellae. Furthermore, there appear to be two different forms of mixed lamellae morphology for thin films ($t = 0.50\,L_0$), a cylindrical form and a lamellar form. Two forms of defectivity are discussed: line defects (dislocations, jogs, etc.) in vertical lamellae, and morphological defects (transitioning to an incorrect morphology such as mixed lamellae or horizontal lamellae). Line defectivity decreases with increasing contrast between the pinning stripe and the background region, while morphological defects occur at extremes in background region preference. This suggests the ideal case is having as preferential a background region as possible without forming morphological defects. The film is found to be

fairly insensitive to minor variations in the width of the pinning stripe, though significantly oversizing the pinning stripe increases defectivity.

A frustrated film thickness is found to give a larger window for forming well-aligned vertical lamellae for symmetric BCPs and density asymmetric BCPs. When there is a cohesive energy density asymmetry in the BCP, film thickness has a large effect on the optimal background region composition for forming well-aligned vertical lamellae. The best case scenario found with regards to the size of the process window is using a CED asymmetric BCP with a pinning stripe that is composed of the lower CED block. This allows lower composition background regions to be used before forming the mixed lamellae morphology, which increases the guidance of the system.

Shifting the volume fraction of a symmetric or density asymmetric BCP away from $\phi_A = 0.5$ extends the well-aligned vertical lamellae regime to more neutral background region compositions. It is theorized this is due to an increase in defect annihilation kinetics due to bridge formation in the film being easier. For a symmetric BCP shifting the volume fraction away from $\phi_A = 0.5$ causes the mixed lamellae morphology to occur at higher background region compositions. It is hypothesized that this is due to $\phi_A = 0.5$ being the composition where the ML morphology transitions between the cylindrical and lamellar morphology, making it the least stable ML morphology. At this transition more preferential background regions are required to form the ML morphology, allowing the lower background compositions to be reached while remaining in the well-aligned vertical lamellae region. The same phenomena is observed for the density asymmetric BCP, though a different volume fraction is required due to the asymmetry in the compressibilities of the blocks. The transition volume fraction was determined from a thin film simulation ($t = 0.5\ L_0$), though the same transition volume improved the process window of a thicker film ($t = 0.75\ L_0$). This suggests the transition volume fraction is only minorly affected, if at all, by the film thickness, though more work is needed to confirm this.

CHAPTER 4

FREE ENERGY OF DEFECTS IN CHEMOEPITAXIAL BLOCK COPOLYMER DIRECTED SELF-ASSEMBLY: EFFECT OF PATTERN DENSITY AND DEFECT POSITION

4.1 Introduction

As discussed in Section 1.4, despite the guidance of BCP films by a chemoepitaxial guiding underlayer, lamellae do not always form defect free morphologies. Line defects such as dislocations and disclinations may form at the surface or in the through-film morphology. The cause for the high defect densities is thought to be one of three sources: 1) non-BCP related procedures, 2) the free energy of the defects are low enough that their equilibrium density is appreciable, or 3) the defects are kinetically trapped. In previous investigations in the free energy of defects it was found that the relative free energies for common simple defects such as dislocations were found to be above $300\ k_B\ T$[24, 25], which yields a very low defect density using Eq. 1.5. While the relative free energies for these defects are high, understanding how defect density, defect order, and the pinning stripe's position relative to the defect affects the defect free energy is still desirable. Defect order is defined here as the number of lamellae between the terminating blocks of the dislocation (indicated by the gray dots in Fig. 4.4). Coarse grained molecular dynamic simulations were run on a BCP thin film atop various underlayers. Using thermodynamic integration, the relative free energies were calculated for the various underlayer types and defect orders.

4.2 Model Description

4.2.1 Coarse Grained Molecular Dynamics Model

The coarse grained molecular dynamics model (Section 2.1) is used in this chapter. Thin films (Section 2.2.2) are simulated on brush underlayers (Section 2.2.2). In order to simulate chemoepitaxy, the underlayer types are assigned based on position. The underlayers being simulated are composed of an alternating pattern of a thin, highly preferential pinning stripe and a wider neutral region. The pinning stripes are always $0.5\ L_0$ wide while the background region is $(n - 0.5)\ L_0$ wide, where n is the degree of density multiplication. In this work the background region is always composed of 50% A beads and 50% B beads. The pinning stripe is always 100% of either A or B beads depending on which bead type needs to be the pinning type for the simulation. The majority of films were built with dimensions of $8\ L_0$ x $6\ L_0$ x $0.75\ L_0$, where L_0 is the pitch of the BCP, which is 11.8631 nm for this BCP. Illustrations of three of these underlayers are shown in Fig. 4.1. Figure 4.1A shows an 8x density multiplying underlayer its only pinning stripe located at position 0 (the center of the defect). Figure 4.1B shows the same density multiplication but with the pinning stripe in position 2 (two lamellae from the center of the defect). Figure 4.1C shows the same pinning stripe position as Fig. 4.1B, but on a 4x density multiplying underlayer which has an additional pinning stripe located at position -6.

After the two minimization steps (Section 2.3.1), a brief NVT simulation (Section 2.3.2) is run with χ = 0 for 200,000 timesteps (10 ns) in order to collapse the film to the brush underlayer and allow the film to better equilibrate, eliminating any unrealistic density fluctuations generated during the initial build. For these simulations the temperature set point is $T = 500$ K, the controller coupling constant is tau = 0.2 timesteps, and the integration timestep is 0.05 ps.

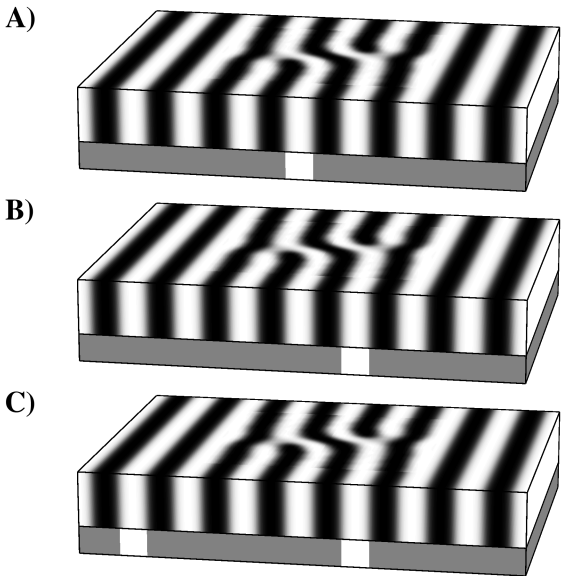

Figure 4.1: Illustrations of three different patterned underlayers used in this work. The top portion of each illustration is the BCP film with a dislocation of order 1. The bottom portion represents the brush underlayer. The background region is represented by the gray region and is neutral to both the white and black blocks of the BCP. The pinning stripe is the white region and is highly preferential to the white block of the BCP. A) An 8x density multiplying underlayer with pinning stripe postion 0. B) An 8x density multiplying underlayer with pinning stripe postion 2. C) An 4x density multiplying underlayer with pinning stripe postion 2.

4.2.2 Thermodynamic Integration

Thermodynamic integration is a method that can be used to calculate the free energy difference between two different states in a molecular dynamics simulation. In thermodynamic integration the molecular dynamics simulation is brought from one state to another in a reversible manner. In this paper, thermodynamic integration is used to calculate the difference in the free energy of a defective BCP film versus a defect free lamellar state. The thermodynamic path used is summarized in Fig. 4.2. A simulation is started in the mixed state at χ = 0. This simulation is then phase separated using only an external potential by ramping the strength of the external potential from A = 0 to A = 1. Next χ is ramped from a value of χ = 0 to χ = 0.55. Finally, the external potential is turned off (by ramping A = 1 to A = 0). This is performed once using a defect free external potential and a second

time using a defect external potential. Since these are constant volume simulations, the free energy measured is the Hemholtz free energy.

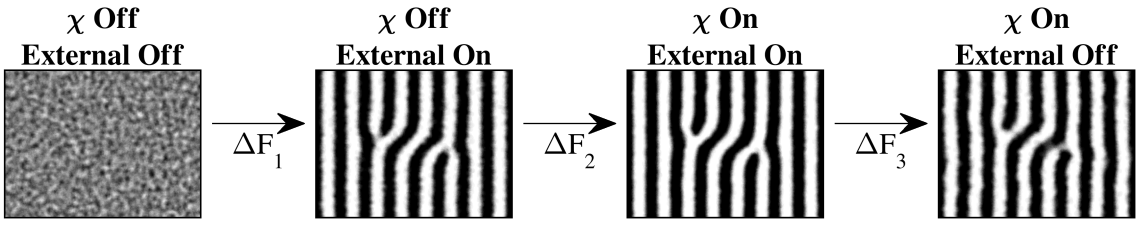

Figure 4.2: Images of the thermodynamic integration pathway used. Simulations start in a mixed state and then phase separated using an external potential. In the next branch χ is turned on which primarily just sharpens the interfaces. Finally the external potential is turned off which allows the film to relax and reach its equilibrium state.

The external potential used to generate defect free lamellae is given by the following equation:

$$V(x) = A \frac{\tanh\left[\frac{1}{2\pi w}\cos\left(\frac{2\pi}{L_0}\,x\right)\right]}{\tanh\left[\frac{1}{2\pi w}\right]}\,, \tag{4.1}$$

where V is the external potential, x is the x position of the bead in the simulation, A is the magnitude of the external potential, w is related to the width of the interface and is given a value of 0.1, and L_0 is the pitch of the BCP. This potential was found to reproduce defect free lamellae well. A one dimensional view of this potential can be seen in Fig. 4.3 while a two dimensional view can be seen in Fig. 4.4 in the defect free case. This potential is also used in all the defective cases in Fig. 4.4 outside the box indicated by the gray corners. The numbers at the bottom of Fig. 4.4 represent the relative position of each lamellae (normalized by $0.5\ L_0$) to the center of the defect. Due to the symmetry of the defect, pinning stripes at equal distance to the center of the defect but on opposite sides of the center are considered equivalent. The external potential used to generate defective lamellae requires the use of a table potential, which can be seen inside the box denoted by the gray corners in Fig. 4.4. The tables for these defects were generated using a defect that formed naturally in a previously run simulation that started from a mixed state and

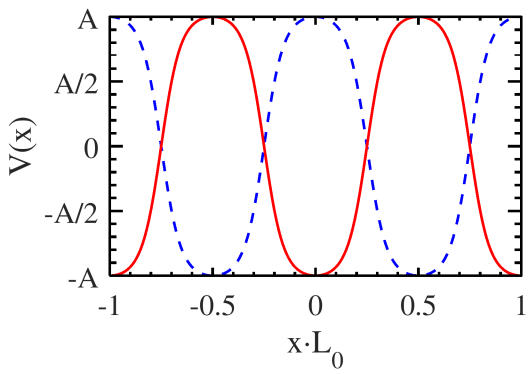

Figure 4.3: The potential used for the defect free lamellae (Equation 4.1) as a function of a beads x position in the simulation volume. The red line indicates the potential an A bead feels while the blue dashed line indicates the potential a B bead feels.

was allowed to undergo phase separation on its own (i.e. without the aid of an external potential). The defect used naturally occurred and persisted for a long period of time. To generate the defect table, snapshots were taken of the simulation through time. These snapshots were then averaged through time in order to generate the average defect state. It was then assumed that the volume fraction could be related to the potential directly. The tables used had a node spacing of $0.08\ L_0$ with bicubic interpolation being used between nodes.

In the first branch, the external potential is turned on by ramping A from $A = 0$ to $A = 1$. It was found that $A = 1$ is sufficient strength for the external potential to fully phase separate the BCP film. The external potential was turned on in 50 steps, with a stepsize of $\Delta A = 0.02$. Each step in A was run for 1,000,000 timesteps, or 50 ns. It was found that equilibrium was typically reached within the first few nanoseconds. The external potential in the simulation was then logged every 100 timesteps. The external potential energy was averaged over the final 45 ns of each step. The integral in Eq. 4.2 was then evaluated using the trapezoidal rule.

$$\Delta F_1^i = \int_{A=0}^{A=1} \frac{\langle V_{ext}\,(A)\rangle}{A} dA\,, \tag{4.2}$$

where ΔF_1^i is the free energy difference between the beginning and ending state of the first branch and $\langle V_{ext}(A)\rangle$ is the average external potential measured when the external strength is A. Here, and for the remaining ΔF's, the superscript i will represent which path the integration is taking (to a defective or a defect free state).

The second branch ramps on χ while keeping the external potential at full strength. The value of ε_{AB} is decreased in this branch in increments of $\Delta\varepsilon_{AB} = 0.005$ kcal/mol. Each step in ε_{AB} is run for 80,000 timesteps, or 4 ns. Every 100 timesteps the non-bonded potential between A and B beads is measured. This value is averaged over the final 2.5 ns to give $\left\langle V^{AB}_{non-bonded}(\varepsilon_{AB})\right\rangle$, which is then used in the following integral to get the free energy of this branch:

$$\Delta F_2^i = \int_{\varepsilon_{AB}=0.5}^{\varepsilon_{AB}=0.35} \frac{\left\langle V^{AB}_{non-bonded}(\varepsilon_{AB})\right\rangle}{\varepsilon_{AB}} d\varepsilon_{AB}\,, \tag{4.3}$$

where ΔF_2^i is the free energy difference over the second branch. This branch requires less timesteps at each step in ε_{AB} because little bulk rearrangement is happening in the film during this time. Instead, the primary changes noticed are a sharpening of the interfaces between lamellae.

The final branch ramps down the external potential strength. The value of A is decreased from $A = 1$ to $A = 0$ in 30 steps. Each step in A is run for 80,000 timesteps, or 4 ns. Every 100 timesteps the non-bonded potential between A and B beads is measured. This value is averaged over the final 2.5 ns to give $\langle V_{ext}(A)\rangle$, which is then used in the following integral to get the free energy of this branch:

$$\Delta F_3^i = \int_{A=1}^{A=0} \frac{\langle V_{ext}(A)\rangle}{A} dA\,, \tag{4.4}$$

where ΔF_3^i is the free energy difference over the third branch. Like the second branch, less timesteps at each step is required because little bulk rearrangement is happening in the

film.

The difference in free energy of one path versus another is given by the following equation:

$$\Delta F_j = \Delta F_j^{M \to D} - \Delta F_j^{M \to DF}, \tag{4.5}$$

where ΔF_j is the difference in free energy of one branch for one path versus another. The two paths are from a mixed state to a defect state ($M \to D$) and from a mixed state to a defect free state ($M \to DF$). This value is useful since it shows how much contribution to the overall free energy difference each branch had. The overall difference in free energy, ΔF, is then determined by adding the three branches,

$$\Delta F = \Delta F_1 + \Delta F_2 + \Delta F_3. \tag{4.6}$$

Thermodynamic integration is a useful tool for measuring free energy in molecular dynamics models. However, there are a few significant drawbacks. First, as is the case in all free energy models, the size of the simulation volume can affect the free energy of the system.[24] This effect is lessened by using larger simulation volumes. Second, thermodynamic integration gives increases in accuracy by increasing the number of integration steps and by increasing the number of timesteps to average over at each integration step. Both of these methods of increasing the accuracy of free energy measurements involves a significant increase in simulation time. Additionally, in this work there is the possibility that a defect will anneal out of a film (leaving the film in a defect free state) when the external potential is turned off. While the defect annealing is a rare event, if the simulation is run longer (to increase the accuracy of the measurement) then the likelihood of this rare event occurring increases. When the defect does anneal, it violates reversibility, invalidating the free energy measurement.

4.3 Results and Discussion

4.3.1 Pinning Stripe Location

Figure 4.5 shows the free energy difference for an 8x density multiplying underlayer for various pinning stripe positions. In these cases, there is only one pinning stripe in the system. The position of the pinning stripes is their distance from the center of the defect (divided by $0.5\,L_0$), as was shown in Fig. 4.4. It should be noted that odd numbered defects have pinning stripes centered on integer values (n), while even numbered defects have pinning stripes on the half values ($n + 0.5$). The individual branches of the thermodynamic integration for the second branch (ramping up χ) and third branch (turning off the external potential) branch are shown in Fig. 4.5A and Fig. 4.5B respectively, while the overall free energy difference is shown in Fig. 4.5C. The first branch of the integration is not plotted since ΔF_1 is not a function of pinning stripe location. This is because the entire first step is done with $\chi = 0$, so there is no differentiation between underlayer beads. The values of ΔF_1 are 895, 898, 957, 1018, 1168 kcal/mol for defects of order 1, 2, 3, 4, and 5 respectively. All points shown in the figure and the data point mentioned above are the average of three replicates.

Looking at the overall free energy in Fig. 4.5C it can be seen that the dislocations have similar trends with the exception of the dislocation with a defect order (DO) of 1. This is due to many DO = 1 simulations annealing out during the third branch, that is to say, the defects were annihilated leaving behind straight lamellae. While defect annihilation (as well as defect growth) is possible for all defect orders, it was only observed in the DO = 1 case due to the close proximity of the pair of dislocations that DO = 1 is composed of. Due to this close proximity, one dislocation will "feel" when the shape of the other dislocation is perturbed by a nearby pinning stripe. For a larger defect order, there are multiple lamellae separating the dislocations that damp out the perturbation from the pinning stripe. However, in the DO = 1 case there is little material to damp it out. While a dislocation pair can

withstand some perturbation in one dislocation, when both are altered it becomes far more likely the dislocation will change in order.

The effect of DO = 1 annealing out in the third branch when a pinning stripe is close can be seen in the third branch of the thermodynamic integration (Fig. 4.5B). During the third branch, there should be almost no rearrangement of beads in the system if the defect that was built using the external potential is close to the true equilibrium defect shape. If there is no rearrangement, the third branch should be constant with respect to the pinning stripe position. This is approximately the case for all defects other than DO = 1, as will be discussed further later. As mentioned before, when the pinning stripe approaches the center of DO = 1, the defect will frequently anneal out while ramping down the external potential. This spontaneous transition violates reversibility which invalidates the free energy measurement from thermodynamic integration in these cases.

On the other hand, for defects other than DO = 1 the third branch is mostly constant with respect to pinning stripe position (PSP). There are some variations, in particular a lowering of ΔF_3 when the pinning stripe approaches the terminating block of the defect. In these cases the defect will necessarily adapt its shape slightly to accommodate the pinning stripe. However, these variations are small in magnitude and happen gradually in a reversible manner, allowing thermodynamic integration to still be valid. Since the ΔF_3 is roughly constant with regard to pinning stripe position, and what few variations are present appear small, it can be assumed that the second branch of the integration, ΔF_2, is the primary contributer to the total free energy with respect to the pinning stripe position. Therefore, while the total free energy of DO = 1 is likely invalid, the second branch of the integration can be looked at as a proxy for the total free energy.

A few observations can be made by analyzing the second branch of the integration (Fig. 4.5A). First, as the pinning stripe moves further from the defect, towards higher PSP values, the free energy begins to level off at its minimum value. This is due to the pinning stripe interacting less and less with the defect, and therefore having a negligible effect on

the free energy. The pinning stripe position where the free energy levels off increases with increasing defect order, but appears to be within $0.5\,L_0$ of the terminating block. While DO = 1 seems to level off around PSP = 3, each increase in defect order seems to increase this transition by approximately 0.5 PSP. This suggests that pinning stripes beyond a distance of L_0 outside of the terminating block (marked by the gray dots in Fig. 4.4) have little effect on the free energy of the defect.

As the pinning stripe approaches the defect, the free energy increases greatly due to the increased interactions of the pinning stripe with the defect. The magnitude of this increase is on the order of 50 to 100 kcal/mol, implying that these defects will almost never occur naturally above the pinning stripe at equilibrium.

For some of the larger defects, such as DO = 3 or 5, there appears to be a maximum in the free energy when the pinning stripe is not at the center of the defect (PSP = 0). The position of these maximums are roughly PSP= 1 and 2 for DO = 3 and 5 respectively, implying the maximum likely shifts further right as defect order is increased. The location of the maximum corresponds to the lamellae interior to the terminating block of the defect, which is at PSP = 2 and 3 for DO = 3 and 5 respectively. Since the pinning stripe being directly under or to the interior of the terminating block consistently gives the maximum in free energy, it suggests a pinning stripe in these locations destabilizes the defect. This pinning stripe location also likely has the highest kinetics for defect annihilation since a pinning stripe in this location will increase the likelihood of bridge formation which is a necessary step in defect annihilation.[50]

The location where the free energy levels off can be a good approximation for what density multiplication is large enough to allow the defect to form. For example, since DO = 1 levels off around PSP = 3, it can be assumed that this dislocation is more likely to form if the density multiplication is 3x or greater since the defect can form entirely between two pinning stripes. However, if the density multiplication is less than 3x then there is guaranteed to be a pinning stripe in either PSP = 0, 1 or 2, which are in the increased free

energy region. Similarly, for DO = 3 the free energy levels off around PSP = 4 and for DO = 5 it levels off around PSP = 5. This implies that decreasing the density multiplication should decrease the number of the larger defects significantly. However, since the maximum in the free energy is not at PSP = 0 for these larger defects, there exists the possibility of a dislocation pair that straddles a pinning stripe. For example, with DO = 5, if the pinning stripe is at PSP = 0, the dislocation pair can fit nicely on a 3x underlayer with one pinning stripe in the center of the defect and another two on the outside of the dislocation pair (at positions -6 and +6). This particular example defect has been observed naturally in simulations using this model and has been shown to be very stable since the defect persisted without changing in defect order for very long simulation times.

Looking at the overall free energy, ΔF, Figure 4.5C, where the pinning stripe is far from the defect (approaching PSP = 8), it can be seen that the free energy is lowest for DO = 1, increases for DO = 2, increases further for DO = 3, stays approximately the same for DO = 4, and then decreases for DO = 5. It is hypothesized that this trend is due to two competing factors. First, increasing the defect order increases the amount of curvature in the BCP system which enthalpically would increase the free energy. Second, the two halves of the dislocation pair likely destabilize each other when they are too close. This hypothesis would lead to the observed results where initially the free energy increases from defect free to DO = 1 to DO = 3 due to the increasing interfacial area. When DO = 4 is reached, the increase in interfacial area is counteracted by the stabilizing effect of the dislocation pairs being further separated. Finally, with DO = 5 the defect begins to get more stable due to the further separation of the dislocation pairs. This has large practical consequences on defect annihilation kinetics. If it is assumed that the pathway to annealing DO = 5 is for the defect to first shrink to DO = 4, then to DO = 3, and so on, as has been observed in simulation,[50, 51] then DO = 4 could be considered a transition state in the process of annealing DO = 5 to a defect free state. While DO = 5 has a much higher free energy than defect free (≈ 300 kcal/mol) and should therefore be virtually non-existent at equilibrium, the fact that the

transition state DO = 4 has a far higher free energy (≈ 340 kcal/mol) suggests there will be very slow kinetics in annealing out DO = 5. This data helps support the theory that defects in BCP films are kinetically trapped.

It has been shown that thermodynamic integration simulations can suffer from a limited simulation volume.[24] This was a concern, particularly for the larger defect orders since it is more likely the defect could see itself across the periodic boundary. Though it should be noted that the presence of a pinning stripe near the periodic boundary of the system lessens this concern since the pinning stripe decreases the amount a defect could influence itself across the boundary. In order to test the simulation volume effect, a limited number of larger simulations were run. These larger simulations were 12 L_0 wide, while the typical simulations were only 8 L_0 wide. These larger simulation took roughly 1.5 times as long as the smaller simulations. A single replicate was run for defect orders 3, 4, and 5 where the size effect should be most apparent. This is also where the free energy begins to level off and then decrease as detailed in the previous paragraph, so these larger simulations should help verify that trend. An underlayer with 12x density multiplication was used, with the pinning stripe located away from the defect on the edge of the simulation. The results of the larger volume simulations showed the same general trends as was observed in the smaller simulations, with DO = 3 and DO = 4 having roughly equivalent free energies ($\Delta F = 256$ and $\Delta F = 250$ kcal/mol respectively) and DO = 5 having significantly lower free energy ($\Delta F = 170$ kcal/mol). However, while the trend is the same the absolute values of the free energy differences were approximately 100 kcal/mol lower than before. This suggests that the smaller simulations are indeed experiencing this size effect, however it appears they do capture trends accurately.

4.3.2 Density Multiplication

Underlayers with 1x, 2x, 4x, and 8x density multiplication were simulated. Additionally an unpatterned underlayer was simulated in order to approximate an infinite density mul-

tiplication. These results are shown in Fig. 4.6 where the free energy differences between a defective film and a defect free film is shown for various defect orders at as a function of density multiplications. The points shown for each density multiplication are the free energy difference corresponding to the lowest average free energy over all pinning stripe positions for that density multiplication. It can be seen that as the density multiplication increases the difference in free energy decreases. This is due to higher density multiplications having less pinning stripes per area and therefore a lowered driving force for pattern correction when a defect is present. Intuition would suggest that the free energy difference should asymptotically approach the unpatterned (infinite density multiplication) case as the density multiplication increases, which appears to be the case in these simulations.

Assuming a Boltzmann's distribution, the defect density can be estimated using the free energy difference and Eq. 1.5. From Fig. 4.6 these free energy differences can be used to determine what the return is for putting in the increased lithographic effort to make a more highly defined underlayer pattern. For instance, for DO = 5, the difference in free energy between 1x and 2x density multiplication is approximately 100 kcal/mol. Since in these simulations $k_B\,T \approx 1$ kcal/mol, it is e^{100} times more likely to find this defect on a 2x density multiplication than 1x. This type of comparison can be useful when looking at higher density multiplications to determine when increasing density multiplication will no longer have an effect on the equilibrium defect density. For all defects shown here the 8x underlayers had nearly the same defect free energy difference as the unpatterned cases, meaning that at equilibrium the defect density for any density multiplication greater than 8x will all be nearly the same. With the exception of DO = 2, decreasing the density multiplication from 8x to 4x increased the free energy difference by 20 kcal/mol or more. This suggests these defects will occur at least 5e8 times more on an 8x underlayer than a 4x underlayer. On the other hand, for DO = 2, the defects are still small enough that a decrease in density multiplication from 8x to 4x has no effect on the free energy, and even higher smaller density multiplications would be needed to affect the free energy.

Figure 4.7 takes a closer look at the effect of density multiplication in regards to pinning stripe position for DO = 3 by looking at the second branch of thermodynamic integration. The previous section has already discussed the 8x underlayers and have explained why having a pinning stripe in positions 1 or 2 (PSP = 1 or PSP = 2) has the highest free energy difference due to its proximity to the terminating block. As the density multiplication decreases the number of pinning stripes present in the underlayer increases. For 4x underlayers there are two pinning stripes throughout our simulation, yet the 4x underlayers mostly follow the same trend as 8x underlayers. This implies that the extra pinning stripe is still too far away from the defect's terminating blocks to cause it any substantial instability.

For 2x underlayers four pinning stripes are present in the simulations underlayer. It can be seen that the free energy significantly increases as the PSP shifts to the right. This trend can be explained by looking at the locations of all the pinning stripes in the system, but especially the two closest to the defects terminating blocks. For 2x density multiplication, the pair of pinning stripes are always PSP = x and PSP = $x \pm 4$ (See Fig. 4.4, Defect Order 3 for reference). In the case of PSP = 0 and ± 4, the closest distance from one pinning stripe to a terminating block is relatively far (L_0). On the other hand, PSP = 1 and -3 has both pinning stripes $0.5\ L_0$ away from the terminating block (one on the inside and one on the outside). While in the 8x simulations a pinning stripe in position 3 does not significantly increase the free energy, a pinning stripe in position 1 does, explaining why this point is higher in free energy than PSP = 0 and ± 4. A similar analysis can be done for PSP = 2 and -2. Since both of these pinning stripes are beneath a terminating block, and from the 8x simulations we see that this is near where the maximum in the free energy occurs, it follows that this underlayer would have the highest free energy of the 2x underlayers.

A similar analysis can be performed for the 1x underlayer. In this case the nearest pinning stripes are at PSP = $x \pm 2$. Using this, when PSP = 0 and ± 2 there are two pinning stripes directly underneath the terminating block as well as one pinning stripe in the center of the defect which contributes greatly to increasing the free energy. When PSP = -3, -1, 1,

and 3 while there are two pinning stripes in highly unfavorable spots (PSP = ± 1) the two other pinning stripes are getting to the region where they will have less effect on the free energy, causing this position to have an overall lower free energy.

4.4 Conclusions

Molecular dynamics simulations were implemented to determine the effect the pinning stripe and density multiplication has on the free energy of dislocation defects of various orders. For all defect orders it was found that the free energy was generally highest when the terminating block of a dislocation was situated above a pinning stripe, suggesting there is little probability of the defect being positioned in these locations at equilibrium. It was found that pinning stripes approximately $1\,L_0$ outside of the terminating blocks of the defect have little effect on the free energy of the defect. If the defect is large enough, there exists a location in the center of the defect where pinning stripes have less of a free energy penalty than underneath the terminating block, suggesting defects can be stable while straddling a pinning stripe. For the defects explored here when the density multiplication was 8x, the thermodynamic driving force for the removal of the defects simulated here was approximately the same as for unpatterned underlayers because the defect was able to fit in an area without a pinning stripe nearby. While increasing density multiplication does theoretically increase the number of defects present due to a decreased free energy difference, the free energy difference is still incredibly high even on an unpatterned underlayer, making their estimated population very small. This bolsters the idea that the high defect densities reported experimentally are due to kinetic entrapment or other non-BCP factors. Increasing the defect order does not appear to increase the free energy monotonically. Instead, a defect of order 5 appears to have a lower free energy than a defect of order 3. It is hypothesized that free energy versus defect order is controlled by two competing factors: the increase in interfacial area for larger defects increases free energy while the greater separation of the dislocation pairs decreases free energy by stabilizing each dislocation.

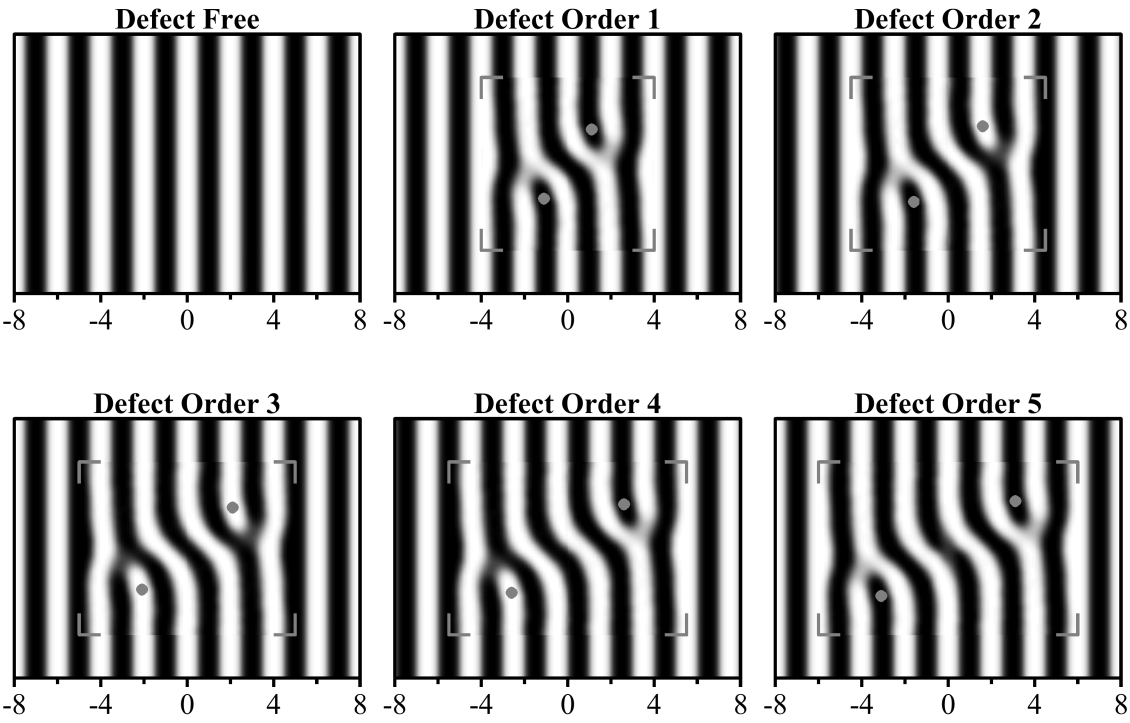

Figure 4.4: The x, y position map of all external potentials used in this paper. Lighter pixels indicate high potential values for A type beads while darker pixels indicate lower values. B type beads feel an opposite potential, with light pixels giving low values and dark pixels giving high values. The defect free potential is only a function of x and is generated by Eq. 4.1. The defective potentials are formed by a combination of a defect free region (outside the box denoted by the gray corners) and a defective region inside. The defective region was formed using a table lookup function with bicubic interpolation. The dislocation order indicates the number continuous (non-branching) jog lamellae between the two dislocations. The x-axis labels indicates the position relative to the center of the defect, which is in units of number of lamellae or $0.5\ L_0$.

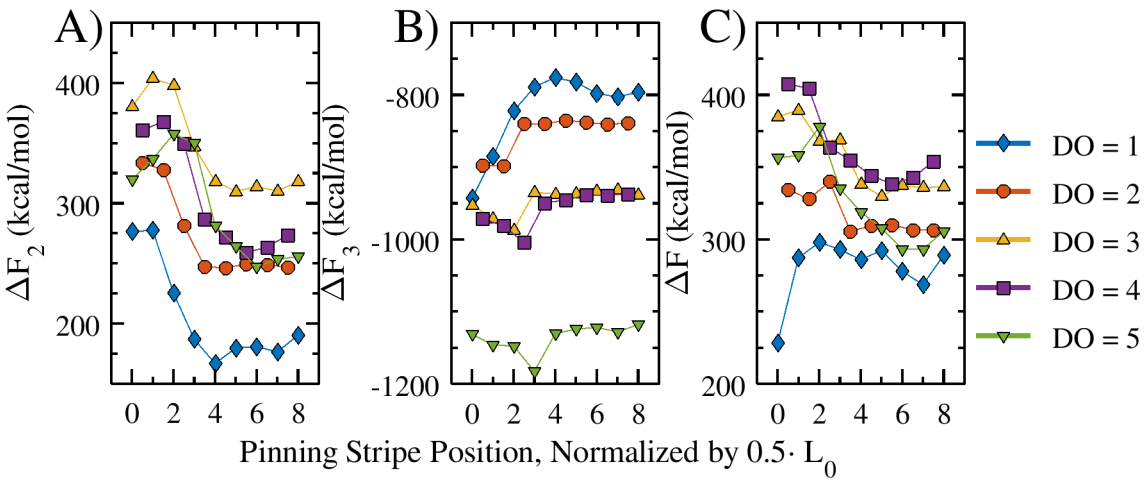

Figure 4.5: Plots showing A) the second branch of the free energy calculation, B) the third branch of the free energy calculation, and C) the total free energy difference between the defect and a defect free state versus the position of the pinning stripe for an 8x density multiplying underlayer.

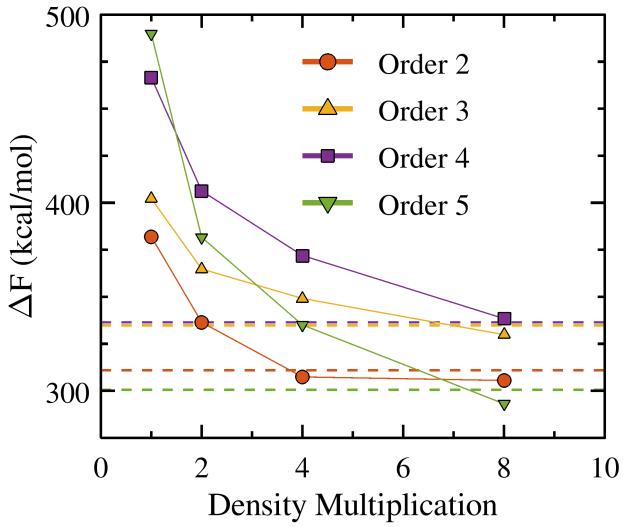

Figure 4.6: Free energy differences for thermodynamic integration for various density multiplications. Each point represents the minimum free energy difference of all pinning stripe positions for that density multiplication. The horizontal dashed lines near the bottom represent the free energy difference of the defect measured on an unpatterned underlayer.

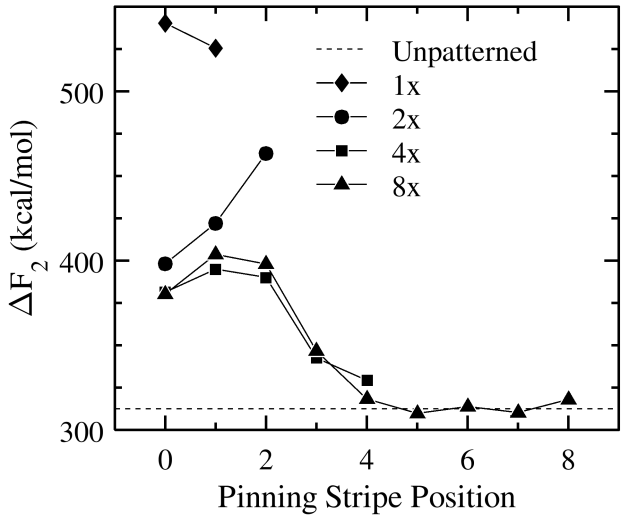

Figure 4.7: Free energy differences for the second branch in the thermodynamic integration for DO=3. The unpatterned underlayer free energy is represented by a horizontal dashed line at the bottom of the graph.

CHAPTER 5
EFFECT OF CHEMOEPITAXIAL GUIDING UNDERLAYERS ON THE PATTERN QUALITY AND SHAPE OF ALIGNED LAMELLAE FOR FABRICATION OF LINE-SPACE PATTERNS

5.1 Introduction

Once the BCP is properly aligned to the underlayer, one block of the BCP can be removed and the remaining block can be used as a mask in subsequent etching, deposition, or doping steps. It is important that the lamellae that formed be as straight as possible along the length of the line, as both line edge roughness (LER) and line width roughness (LWR) adversely affect performance.[43] The lamellae need to also form as straight vertically as possible in order to form a proper mask for the anisotropic etch or ion implantation, therefore it is important that during microphase separation no footing of the lamellae should occur, though little work has been done to explore the footing and undercutting of lines. While some work has been done to explore footing due to the geometry of a chemical pattern with no density multiplication,[52, 53] this chapter seeks to explore the effects varying parameters in a density doubling underlayer (2x density multiplication) has on line quality, both in terms of roughness and footing. The parameters to be explored include the composition of the background region and the width of the pinning stripe.

5.2 Model Description and Experimental Methods

This chapter uses the basic coarse grained molecular dynamics model described in Section 2.1. Instead of initializing thin films simulations to a well mixed state (as described in Section 2.2.2), here they are initialized to a pre-aligned state. To do this, generated chains are rotated before being placed in the simulation volume. The chain is rotated such that the

primary axis of its radius of gyration tensor is placed along the x dimension, the secondary axis is placed along the y dimension, and the tertiary axis is placed along the z dimension. Finally, the chain is placed such that its center of mass is located along where a lamellar interface should be (with the A and B ends of the chains inside the future A and B domains respectively). An example of this is seen in Figure 5.1A.

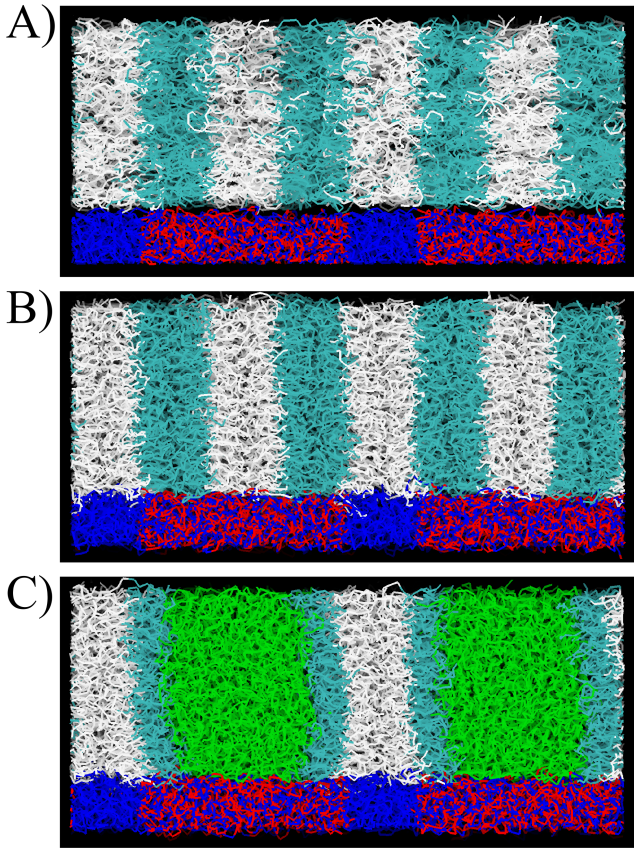

Figure 5.1: Cross-section of the A) initial build and B) final state of a pre-aligned simulation, and C) the cross-section of a simulation with homopolymer. In this view, A beads are represented by white and blue (in the film and underlayer respectively) and B beads are represented by cyan and red. The homopolymer B beads are shown as green.

These films are placed on a flat cross-linked mat, similar to those described in Section 2.2.2, though these are made with a slightly different algorithm which will be discussed below. The cross-linked mat underlayer was chosen in order to allow fine control over the width of the pinning stripe that would be patterned into it.

Underlayers were built in this system to model a cross-linked underlayer using the following process: a small simulation box two inherent pitches wide (23.6 nm), 25 nm long, and 250 nm tall was built. A single very long chain was modeled in this box by taking a random walk, with enough beads in the chain that it would fill a 23.6 nm $\times$ 25 nm $\times$ 15 nm box completely with a density of 1.4 beads/nm^3. This chain then underwent molecular dynamics for 25 ns, in which time the chain completely collapsed upon itself and formed a suspended film, which was to be the basis of the underlayer. This suspended film was roughly flat on both the top and the bottom of the film. Next, this suspended film was replicated in the x and y dimensions to the desired box size, 47.2 nm $\times$ 100 nm. Once replicated, the density of the suspended film through the z dimension was calculated. The top surface of the film ($z = 0$ nm) is defined as the point where the density falls below 0.9 beads/nm^3. All beads below $z = -4$ nm were deleted in order to speed up the simulation by not needing to perform calculations on these lower beads. This depth was chosen since the cut-off for non-bonded interactions is 4 nm, and therefore beads below $z = -4$ nm would not interact with the film if they were included. Removing these beads breaks the single chain that was simulated into many smaller chains, with the chain ends being located near $z = -4$ nm. These chain ends are fixed in space so that none of these chains diffuse into the film and interfere with the simulation. Since all the chain ends are near $z = -4$ nm, this increased fixed bead density should not affect the dynamics of the film. Next, in order to simulate cross-linking, approximately 20% of the beads in the underlayer had their positions fixed, meaning these beads cannot move through space when undergoing molecular dynamics. This number of beads was chosen since a higher density of fixed beads can cause a density wave to appear in the BCP film while with a lower cross-link density the film and underlayer interpenetrate too much.[37] Finally, the underlayer is patterned by changing the bead types of the underlayer based on the position in the x-dimension. For this paper, the underlayer consists of a pinning stripe where 100% of the beads are A beads, followed by a background region where between 15% and 50% of the beads are randomly

chosen to be A beads while the remainder are chosen to be B beads, simulating a perfectly random copolymer. In all cases, the width of the repeating pattern is $W_{pattern} = 23.6$ nm or $W_{pattern} = 2\ L_0$, which is a pitch doubling pattern. The width of the pinning stripe and background region vary depending on the simulation. These underlayers are initially more ideal than can be achieved through experiment, with minimal topography in the underlayer, no LER in the pinning stripe, no interfacial roughness, and a uniformly distributed composition throughout the background region. However, as molecular dynamics are run some LER and interfacial roughness will be introduced into pinning stripe through fluctuations at the pinning stripe/background region interface.

The pre-aligned films were built to fill a 47.2 nm $\times$ 100 nm $\times$ 15 nm periodic box with a density of 1.35 beads/nm^3. The film was placed on top of the cross-linked underlayer.

In order to verify that the pre-aligned films can give reliable data, a small subset of the underlayers used in this paper were built, once with an initially aligned film and once with an initially mixed film. Molecular dynamics were run for both of these cases. Both LER and the variations in line width through depth (VWD) were measured through time for both cases (Section 2.5.3). It was found that only a few nanoseconds of simulation were needed for the pre-aligned films LER and VWD to stabilize, and that the final values reached were in good agreement with those measured for the initially mixed simulations. This confirms that for these measurements building a film pre-aligned does not seem to create any artifacts past the first few nanoseconds. The simulations used in this paper were run for 100 nanoseconds, with only the last 40 nanoseconds being analyzed in order to safely avoid this initial region.

Additional simulations were built like the pre-aligned films, but with the BCP chains that participate in forming the unpinned lines, where the white domain lines above the background region, replaced with homopolymers, as seen in Fig. 5.1C. These homopolymers, seen in green, are composed of B type beads (also shown in cyan and red in the film and the underlayer respectively). These simulations were built in order to separate the effect

of the underlayer properties on the pinned line (the white domain line above the pinning stripe) from the effect of the unpinned line on the pinned line by removing the relatively rigid unpinned line and replacing it with malleable homopolymer.

In order to explore the effect of the width of the pinning stripe and the composition of the background region, a series of simulations were run using 5 pinning stripe widths (W_{pin} =3.54 nm, 4.72 nm, 5.90 nm, 7.08 nm, and 8.26 nm, or $W_{pin} = 0.3\ L_0$, $0.4\ L_0$, $0.5\ L_0$, $0.6\ L_0$, and $0.7\ L_0$) and 8 background compositions ($f_A = 0.15$, 0.20, 0.25, 0.30, 0.35, 0.40, 0.45, and 0.50). Five replicates of each situation were run in order to get better statistics.

When running these simulations, two minimizations were used as described in Section 2.3.1. Once this second minimization is complete, regular molecular dynamics are run in NVT for 100 ns (2,000,000 timesteps).

Once the simulations are completed, analysis is done in order to measure LER, LWR, and the variation of width through depth (VWD) as described in Section 2.5.3. However, the images being analyzed in calculating LER and LWR are generated in a slightly different method than shown in Section 2.5.1, as will be described here. A topdown two dimensional projection of the films in the simulations is generated, where each pixel is 0.1 nm $\times$ 0.1 nm. For each cell on this image, which correspond to an x and y position in the simulation, the local volume fraction of A beads (f_A) is calculated by calculating the local density of A beads and the total local density at that point. The volume that the beads take up in the image do not accurately represent the true volume of the atoms in the system because each bead is a coarse grained representation of the center of mass of a much larger number of atoms, thus the images can show a large amount of empty space that is not present in a real system. To avoid this, the beads are treated as a mass field instead of a point mass. This mass field has the form of a two dimensional Gaussian function with a standard deviation of 0.3 nm and a cutoff of 0.9 nm. By doing this, if a pixel is placed in between beads, instead of seeing 0 density of beads, it will weakly feel the effects of all neighboring beads.

Samples of these images can be seen in Fig. 5.4. Once the images are generated, LER and LWR are generated as described in Section 2.5.3.

The potential a bead would feel due to the underlayer was calculated using a simplified model where the underlayer is described as a continuous slab with uniform density of ρ instead of a collection of discrete beads. The potential a bead above the underlayer would feel from the underlayer (ignoring interactions with the film) would be determined by calculating the following integral:

$$V_{ijk}(x,z) = \int_{r=1nm}^{r=4nm} \varepsilon_{ij} \cdot \left[\left(\frac{\sigma_{ij}}{r} \right)^8 - 2 \cdot \left(\frac{\sigma_{ij}}{r} \right)^4 \right] \cdot \rho \cdot f_{jk}(x) \cdot A_k(x,z,r) \cdot dr \,, \quad (5.1)$$

where $V_{ijk}(x,z)$ is the potential a bead of type i would feel at a position x, z from underlayer beads of type j in either the pinning stripe or the background region (indicated by the subscript k), f_{jk} is the volume fraction of type j in either the pinning stripe or the background region, and $A_k(x,z,r)$ is the surface area of a sphere with radius r and center x,z that intersects the pinning stripe or background region. A_k only considers the surface area within the volume of the underlayer so that the interaction of the film with itself is neglected. A two dimensional view of a single step in the integration in Equation 5.1 is shown in Fig. 5.2 for two separate (x,z) locations. The area term in Equation 5.1 is shown in Fig. 5.2 where the blue highlighted section of the circle indicates the cross-section of the area of the sphere intersecting the background region, and the yellow highlighted section indicates the cross-section of the area of the sphere intersecting the pinning stripe. The lower bound of the integral in Equation 5.1 of $r = 1$ nm was chosen in order to avoid the highly repulsive section of the potential, and the upper bound of $r = 4$ nm was chosen since this is the normal cutoff used in this model. This integral was calculated for all x positions of a bead across both the pinning stripe and the background region at a height of $z = 0.001$ nm. Once the potential across the underlayer is determined separately for $j =$ A and $j =$ B bead types, these potentials are summed. Finally, the potential calculated for the

i = A beads is subtracted from the potential calculated for the i = B beads. This difference in potential helps indicate whether an A bead would be in at a lower energy state (positive values) or a B bead would be at a lower energy state (negative values) at a given x position. Examples of these differences in potential can be seen in Fig. 5.8 and Fig. 5.9B.

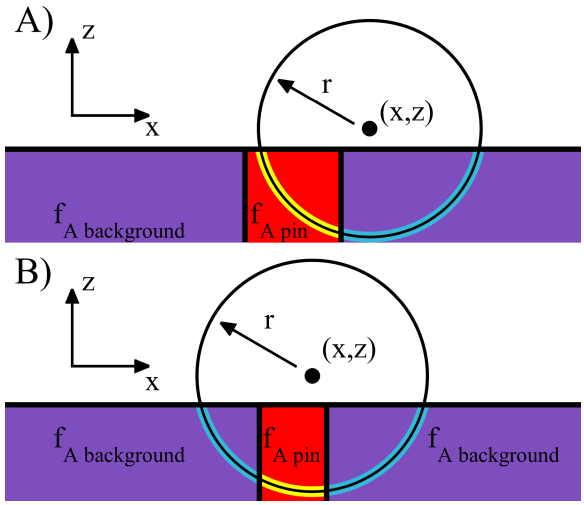

Figure 5.2: Cartoon showing two examples of a two dimensional view of one step in the integral from Equation 5.1 when calculating the potential at a point (x,z). In both cases, the yellow highlighted portion of the circle indicates the surface area intersecting the pinning stripe (A_{pin}), and the blue highlighted portion of the circle indicates the surface area intersecting the background region ($A_{background}$).

5.3 Results

5.3.1 Line roughness versus stripe width and composition

The first aspect of line quality explored was the effect of underlayer properties on the LER of the BCP lines. In Fig. 5.3 the LER is reported for simulations exploring the effect of the width of the pinning stripe and the composition of the background region for both the pinned A line (Fig. 5.3A) and the unpinned A line (Fig. 5.3B). Increasing the composition of the background region from being preferential to B ($f_A = 0.15$) to being neutral to both A and B ($f_A = 0.5$) increases the LER of both the A domain line above the pinning stripe, or the pinned line (PL), and the A domain line above the background region, or

the unpinned line (UPL). The increase in LER when increasing the composition of the background region is caused by a decrease in energetic contrast between the pinning stripe and the background region. As the energetics of the pinning stripe and background region become more similar (i.e. the contrast between them decreases), the penalty for the A domain being over the background region decreases. This decrease in energetic penalty allows the LER to increase without increasing the energy of the system as significantly as would occur if the background region were highly preferential to the B domain.

Undersizing the pinning stripe also appears to increase the LER of the system, since in this case the center of the line can now be offset from the center of the pinning stripe while still having the entire pinning stripe covered by the PL, thus not paying the energetic penalty of placing one of the adjacent B domain lines over the pinning stripe. To illustrate this line placement error, Fig. 5.4 shows a top-down image of two simulations, with Fig. 5.4A showing a simulation with a preferential background region ($f_A = 0.15$) and a pinning stripe that is one half pitch wide ($W_{pin} = 0.5\ L_0$) and Fig. 5.4B showing a simulation with a neutral background region ($f_A = 0.5$) and an undersized pinning stripe ($W_{pin} = 0.3\ L_0$). The approximate edges of the pinning stripes in these simulations are shown as red lines. As can be seen in Fig. 5.4A, with a half pitch wide pinning stripe and a preferential background region the edges of the PL are in close agreement with the edges of the pinning stripe along the length of the simulation. However, in Fig. 5.4B it can be seen that on an underlayer with an undersized pinning stripe and a neutral background the PL wavers much more. There is typically a significant energy penalty for the PL to uncover the pinning stripe. However, since the pinning stripe is narrower than the PL, the pinning stripe can remain fully covered by the PL while allowing the PL to waver. The wavering of this line increases the LER of the PL in this situation, and this increase in LER propagates to the unpinned line.

In Fig. 5.3 it can be seen that the LER of the pinned and unpinned lines are positively correlated, however the LER of the UPL is consistently higher than the LER of the PL. While the PL has the underlayer interactions to help keep the line relatively straight, the

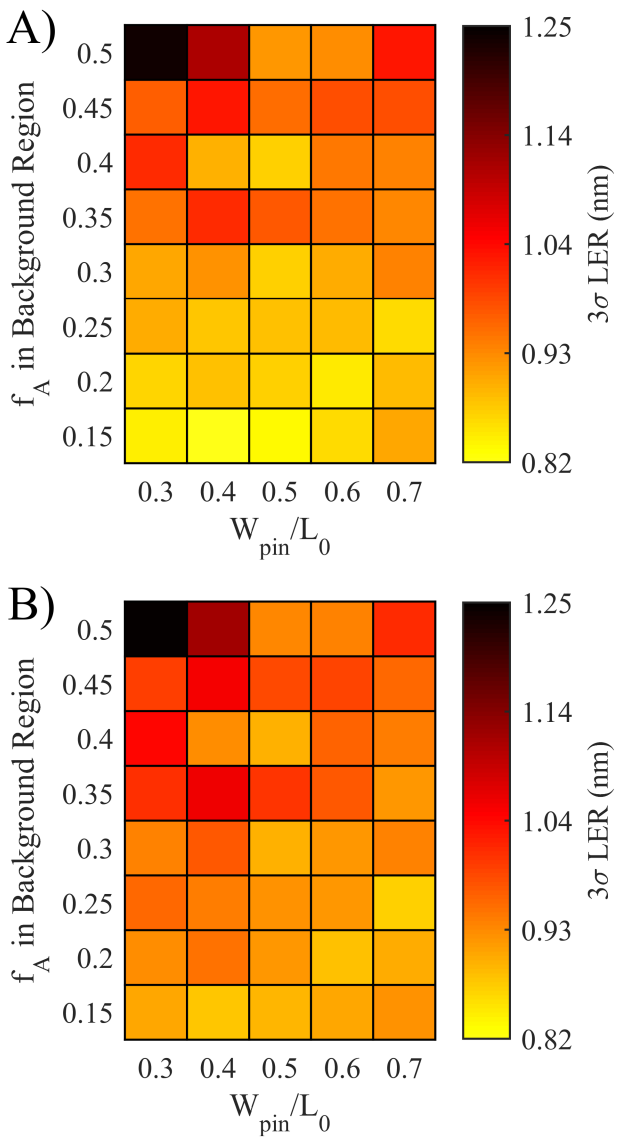

Figure 5.3: 3σ LER versus composition of the background region and the width of the pinning stripe for A) the pinned line and B) the unpinned line.

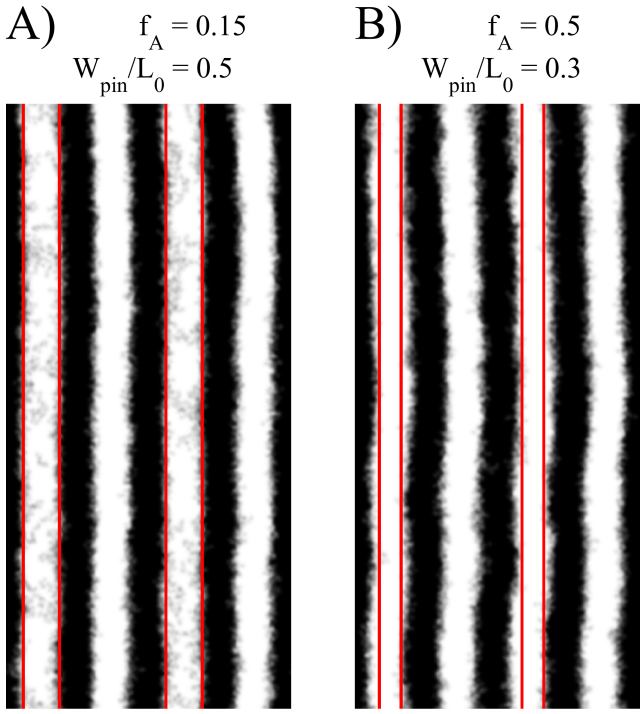

Figure 5.4: Generated images of a simulation A) with a pinning stripe with a width of a half pitch ($W_{pin} = 0.5\ L_0$) and a preferential background region ($f_A = 0.15$), and B) with an undersized pinning stripe ($W_{pin} = 0.3\ L_0$) and a neutral background region ($f_A = 0.5$). Red lines are drawn in to indicate the location of the pinning stripe.

only driver to keep the UPL straight is the PL on either side; therefore, the UPL has increased roughness due to decreased guidance. If higher density multiplication than the 2x used here were to be simulated, it is expected the LER of the UPL would likely increase for UPLs with greater distance from the PL, due to a decrease in correlation between line edges with distance. However, since 2x density multiplication was used here, the UPL is still highly correlated with the PL, causing its LER to only be slightly higher than the PL.

The LWR for both the PL and the UPL were measured for varying underlayer properties. It was found that LWR did not significantly change when varying the underlayer properties, with all 3σ LWR values falling in the range of 0.79 nm and 0.85 nm. The fact that LWR seems to remain constant with respect to underlayer properties while LER changes suggests that the roughness in one line edge must be highly correlated with the adjacent line edge. This can be seen in Fig. 5.4B where the lines seem to become more sinusoidal in nature, which increases LER and while keeping LWR similar.

5.3.2 Line shape versus stripe width and composition

The cross-sectional images of films were analyzed to look at the effect of background region composition and pinning stripe width on the shape of the lines formed. A sample of these cross-sections is shown in Fig. 5.5 which shows the final timestep ($t = 100$ ns) for the first replicate of a subset of the array of simulations. As can be seen from the generated cross-sectional images, an over-sized pinning stripe ($W_{pin} = 0.7\ L_0$, right column) significantly perturbs the shape of the pinned line away from the desired straight sidewalls when approaching the film/underlayer interface by causing the line to foot. In a similar manner, with a more highly preferential composition of the background stripe ($f_A = 0.15$, bottom row) the unpinned line begins to deform near the film/underlayer interface by undercutting.

To quantify the deformation of the lines, the width of the lines through the depth of the film was measured. Some representative line widths through depth are shown in Fig. 5.6.

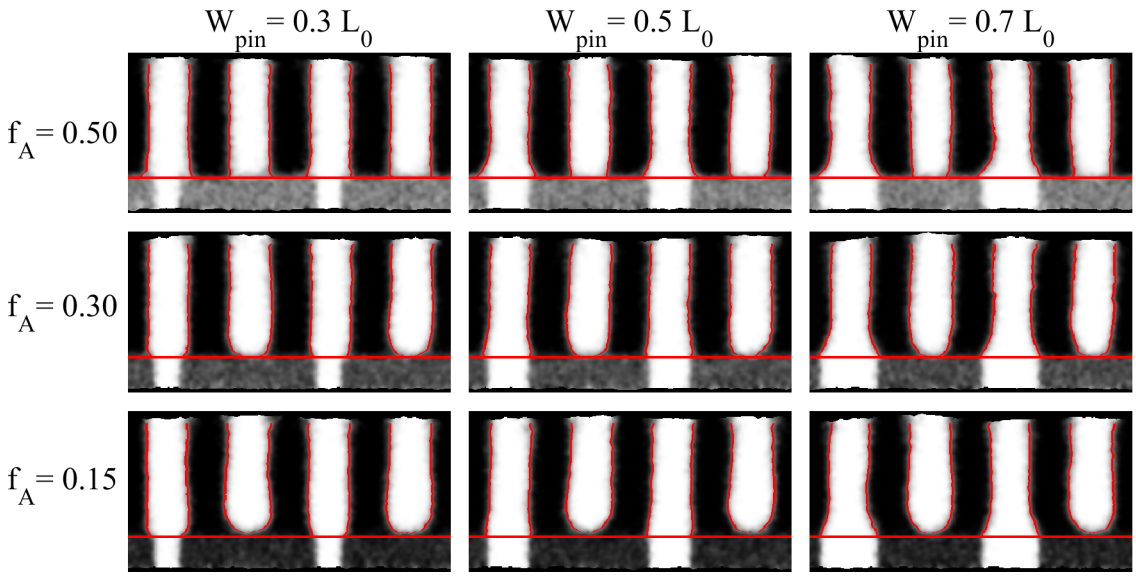

Figure 5.5: Generated cross-sectional images of series of simulations varying background stripe composition (f_A) and pinning stripe width (W_{pin}). The red lines indicate the film/underlayer interface as well as the border between A lines (white) and B lines (black).

In Fig. 5.6A, it can be seen that with a neutral background region and an undersized pinning stripe (upper left simulation in Fig. 5.5) both line widths appear to vary through depth far less than in the other two instances shown which have a preferential background region and a larger pinning stripe. In Fig. 5.6B, the line widths for a preferential background region and a pinning stripe of width $W_{pin} = 0.5L_0$ are shown (middle simulation in Fig. 5.5). This is likely close to the optimal process conditions for aligning a BCP film[49] and are decent at decreasing LER (Fig. 5.3), however, it can be seen that in this case there is still some footing of the PL, even with a pinning stripe width that is commensurate with the natural width of the line. Finally, in Fig. 5.6C, it can be seen that an oversized pinning stripe with a preferential background region (middle right simulation in Fig. 5.5) causes greatly increased footing of the PL. However, while the PL does foot below around $z = 3.5$ nm, above $z = 3.5$ nm the width of the PL is actually less than the width of an unperturbed line. This is due to mass conservation, when the base of the line expands, assuming constant density, the mass must come from the top of the film, causing the line to shrink higher in

the film. The opposite trend is seen in the unpinned line, which undercuts below $z = 3.5$ nm but is swollen above $z = 3.5$ nm.

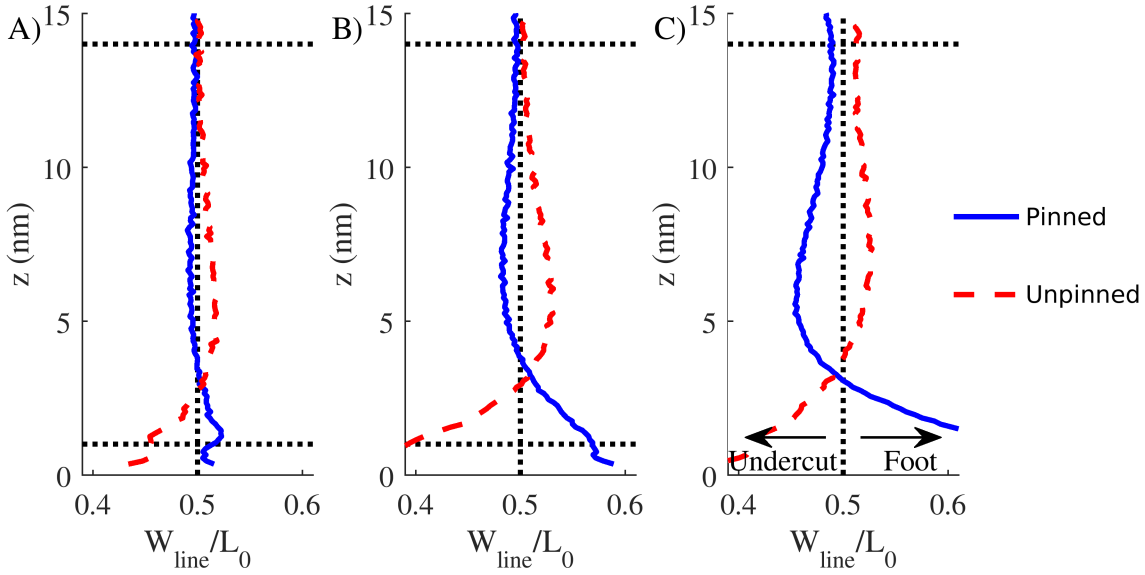

Figure 5.6: Line width measured through depth of a film for three simulations: A) An undersized pinning stripe, $W_{pin} = 0.3\ L_0$, with a neutral background region, $f_A = 0.5$. B) A regularly sized pinning stripe, $W_{pin} = 0.5\ L_0$, with a preferential background region, $f_A = 0.3$. C) An oversized pinning stripe, $W_{pin} = 0.7\ L_0$, with a preferential background region, $f_A = 0.5$.

In order to determine the degree of the deformation of the lines, the variation in the line width through depth (VWD) of the pinned and unpinned lines was measured. The VWD was calculated by taking the standard deviation of the line width measurements between $z = 1$ nm and $z = 14$ nm. This range was chosen in order to avoid the noise that appears in the system when nearing the substrate ($z = 0$ nm) or the free interface ($z = 15$ nm). These cutoffs are shown in Fig. 5.6 using horizontal black dashed lines. The calculated VWD are plotted in Fig. 5.7, with Fig. 5.7A showing the results for PLs and Fig. 5.7B showing the results for the UPLs. As can be seen, increasing the width of the pinning stripe has a very large effect on the VWD of the PL, because increasing the width of the pinning stripe increases footing in the PL, as seen in Fig. 5.6C. Increasing the pinning stripe width also increases the VWD in the UPL, though not to the same degree as for the PL since the UPL

is not in contact with the pinning stripe and is only indirectly influenced by the PL. It is the footing of the PL that causes the UPL to undercut due to the PL compressing the chains of the UPL.

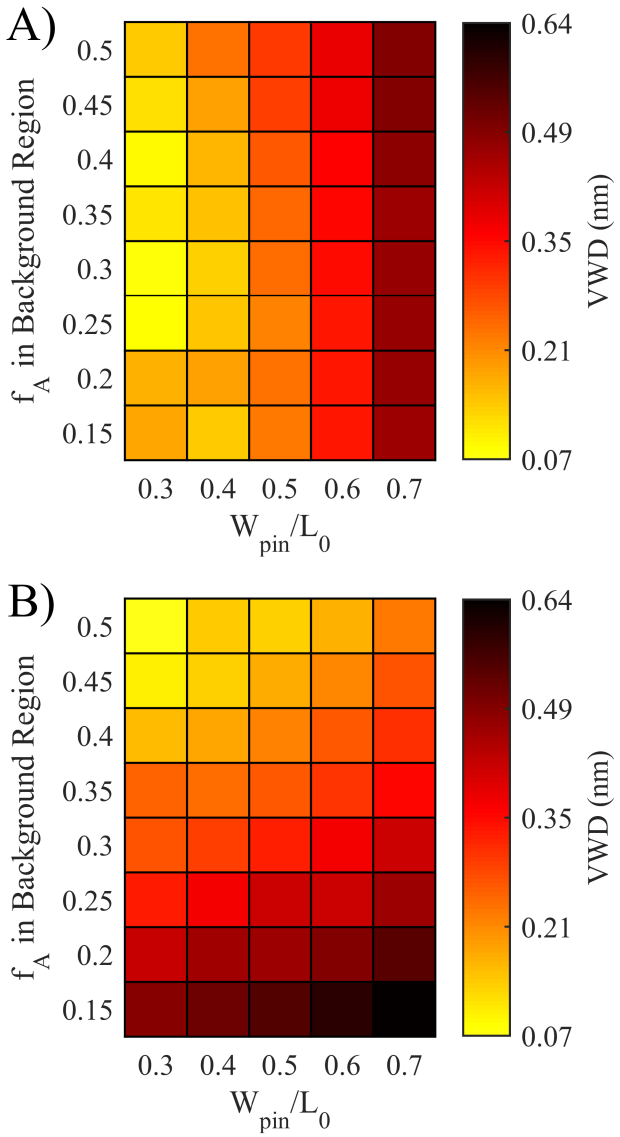

Figure 5.7: Plots of the standard deviation in the width through depth (VWD) of the A) pinned lines and B) unpinned lines, varying the width of the pinning stripe and the composition of the background region (f_A).

Decreasing the volume fraction of A beads in the background region (f_A) has a larger effect on the unpinned line than altering the pinning stripe width. When the background

region becomes less preferential to the A domain ($f_A < 0.5$), there is an energetic penalty to place an A bead in contact with the background region instead of a B bead, therefore the unpinned line begins to undercut in order to minimize contact with the less preferential substrate. The PL, however, does not experience a significant change when altering f_A, with the VWD only slightly increasing as f_A increases. With regards to the PL, for a regularly sized pinning stripes ($W_{pin} = 0.5\ L_0$), decreasing f_A increases the energetic penalty for footing to occur, therefore the VWD in the PL end up decreasing with lower f_A. For an oversized pinning stripe ($W_{pin} = 0.6\ L_0$ and $0.7\ L_0$), altering the composition of the background stripe does not allow the PL to foot much more, since there is already significant footing due to the oversized pinning stripe. This footing due to the oversized pinning stripe leads to the chains composing the PL to be stretched, so stretching them further due to the background composition is difficult. Due to this effect, altering the composition of the background region does not significantly change the degree of VWD seen in the PL on an oversized pinning stripe. Undersized pinning stripes ($W_{pin} = 0.3\ L_0$ and $0.4\ L_0$) see an opposite trend, with larger VWD occurring as f_A lowers. Since the pinning stripe is smaller than the PL, when the background region is preferential to the other block, instead of footing as was seen in the case of larger pinning stripes, it is energetically favorable for the PL to undercut near the substrate so that the A domain is not in contact with the background region. However, as the background region becomes more neutral ($f_A \rightarrow 0.5$) this energetic penalty is lessened, and the PLs are able to form straighter, with less VWD.

As mentioned before when discussing Fig. 5.6B, when the pinning stripe width was $W_{pin} = 0.5\ L_0$, a width commensurate with the nominal width of a line, all background compositions show footing in the pinned line to some degree. While in some cases this footing might be caused by the undercutting of the unpinned line, the footing is also present with a background composition that was neutral to both blocks ($f_A = 0.5$), which should have a straight unpinned line. The footing present in these simulations is likely caused by

chemical interactions with the pinning stripe. In this model, beads within 4 nm of the pinning stripe still had non-bonded interactions with the pinning stripe, despite being above the background region (see Fig. 5.2A). Since the strength of the non-bonded potential generally decreases with distance, a bead above the background region will only weakly feel the pinning stripe, except for beads sufficiently close to the interface of the pinning stripe and background region. For these beads, the chemical interactions with the pinning stripe can be strong enough to overpower the chemical interactions with the background region, making the region near the pinning stripe but above the background region be preferential to the pinned line. This preferential region would then be wider than the pinning stripe, and would explain the footing present in the case of a neutral background region and a pinning stripe that has a width of $W_{pin} = 0.5\ L_0$.

To illustrate how the preferential region might be wider than the pinning stripe, the potential that both an A and a B bead would feel across an underlayer was calculated using Eq. 5.1. The difference in these potentials was taken and plotted in Fig. 5.8. A positive difference in potentials means an A bead would be at a lower energy than a B bead in that position, and therefore that position is energetically favorable for the A bead. Therefore, the region of the curves in Fig. 5.8 that are positive are the preferential region for an A bead. In Fig. 5.8A, these curves are shown for a constant background composition, varying the pinning stripe width. The edges of the pinning stripe are indicated by the vertical colored lines along the curves. It can be seen that for both $W_{pin} = 0.5\ L_0$ and $W_{pin} = 0.35\ L_0$ the preferential region around the pinning stripe is larger than the pinning stripe itself. This result suggests that to have a preferential region (not a pinning stripe) with a width of $W_{pref} = 0.5\ L_0$, which might be ideal for eliminating footing, one must undersize the pinning stripe. For the composition shown in Fig. 5.8A ($f_A = 0.3$), the pinning stripe width must be approximately $W_{pin} = 0.35\ L_0$. However, the composition of the background region has a large effect on the width of the preferential region, as can be seen in Fig. 5.8B, which plots the difference in potential for various background compositions at a constant

pinning stripe width of $W_{pin} = 0.5\ L_0$. It can be seen that decreasing the composition shrinks the preferential region by lowering the difference in potential reached above the background region when far from the pinning stripe.

It should be noted that in Fig. 5.8A it can be seen that as the width of the pinning stripe decreases, the maximum difference in potential decreases due to the fact that above a narrow pinning stripe beads will have more chemical interactions with the neighboring background regions. A smaller difference in this potential indicates that there would be less energetic penalty for placing the wrong domain block above the pinning stripe as well as there being less energetic penalty for placing the pinned line above the background region, which will cause the underlayer to have less effective guidance since defects will have a lower free energy. This decrease in the energetic penalty will lead to an increased LER, which would explain some of the variation seen in Fig. 5.3.

As the width of the pinning stripe continues to decrease, eventually a point is reached where the pinning stripe is small enough that no position above the pinning stripe is preferential to the pinned line. This occurs when the pinning stripe is narrow enough that beads above it are close to the background region on either side of the pinning stripe, such as in Fig. 5.2B. This can cause the background region interactions with the bead to overpower the pinning stripe interactions. The result is a constantly negative difference in potential, as seen in Fig. 5.8A when the pinning stripe has a width of $W_{pin} = 0.5\ L_0$. Here, no point on the underlayer is preferential to an A bead over a B bead. This would likely lead to horizontal lamellae formation depending on factors such as the film thickness and background region composition.

For this simulated BCP the pinning stripe must be significantly undersized for the underlayer to fail to guide the film. However, for future BCPs that have a smaller domain, the underlayers ability to align the BCP might be more of a concern. Decreasing the domain of the BCP would decrease the size of the pinning stripe if the target width remains W_{pin}. Decreasing the pinning stripe width, as shown, decreases the ability for the underlayer to

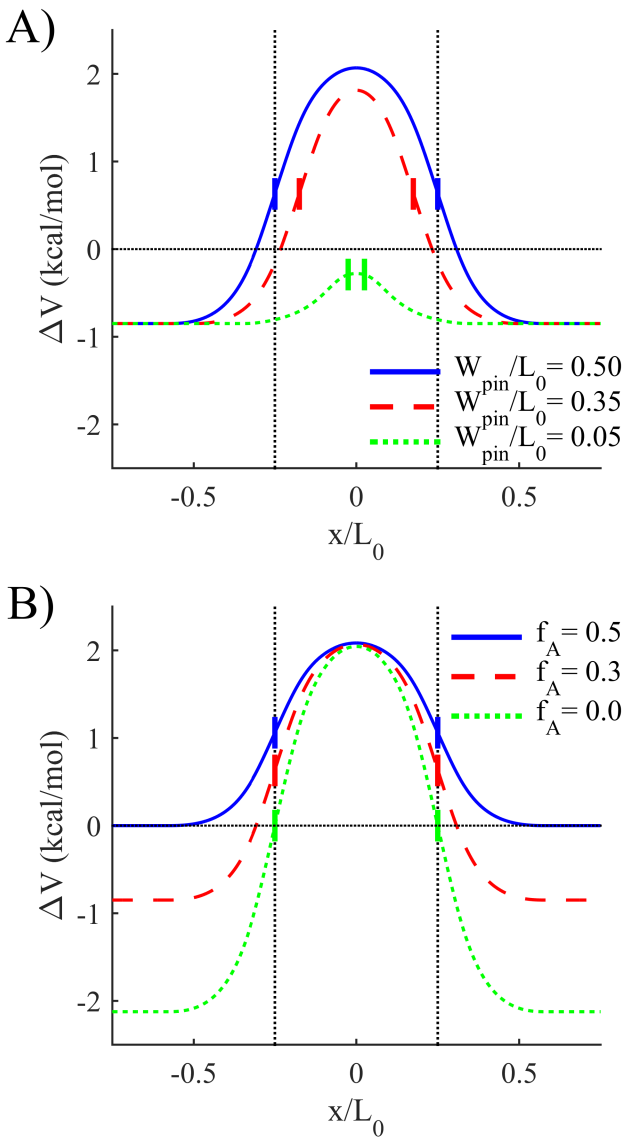

Figure 5.8: Difference in potential for an A and B bead across the surface of a chemo-epitaxial guiding underlayer, plotted A) for various pinning stripe widths at a constant background composition of $f_A = 0.3$ and B) for various background compositions at a constant pinning stripe width of $W_{pin} = 0.5\ L_0$. Colored vertical lines indicate the edge of the pinning stripe for each case.

align the BCP. This effect will be complicated by the fact that a smaller domain BCP will likely have a larger χ (to accommodate a smaller degree of polymerization while remaining above the order-disorder transition). A higher χ value should increase the ability for the pinning stripe to guide the BCP. However, the new BCP might additionally have a different interaction range (which is related to σ and the integration bounds in the non-bonded potential used in this simplified model). Between these three effects - decreasing the width of the pinning stripe, increasing χ, and changing the interaction range - it is very difficult to predict if the shrinking pinning stripe width will be an issue or not. If the point is ever reached where the half-pitch pinning stripe width is incapable of properly guiding the BCP film, alternative guidance schemes could be implemented, such as using a pinning stripe with a width of $W_{pin} = 1.5\ L_0$ for a 3x or higher density multiplication.[47]

If it is assumed that footing of the pinned line is minimized when the width of the preferential region is $W_{pref} = 0.5\, L_0$, the optimal combinations of the background composition and width of the pinning stripe can be computed. These optimal combinations are shown in Fig. 5.9A, where it can be seen that increasing the width of the pinning stripe requires decreasing compositions of the background region to maintain a constant width of the preferential region. Figure 5.9B shows the difference in potential curves for three combinations of pinning stripe width and background composition that give a preferential region with a width $W_{pref} = 0.5\ L_0$, which can be seen by the fact all three of these curves intersects $\Delta V = 0$ at $x = 0.25\ L_0$. As can be seen, shifting to wider pinning stripes and lower background compositions greatly increases the absolute difference in potentials, both above the pinning stripe and above the background region, suggesting that near this end of the design space there will likely be lower LER and defectivity. However, it is also important to note that not all of these composition/width combinations will be capable of aligning a BCP film from a mixed state, as can be seen elsewhere.[49]

The combinations of background region composition and pinning stripe width determined by the model are shown against the measured VWD for the PLs of the previous

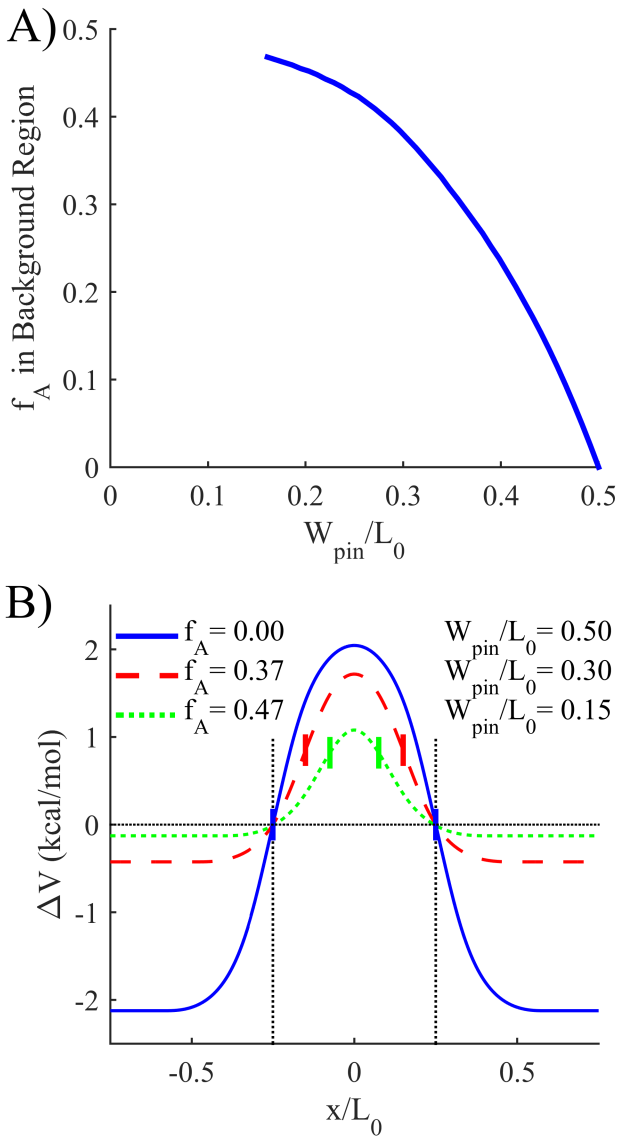

Figure 5.9: A) The combinations of background region composition and pinning stripe width yielding a preferential region with a width of $W_{pref} = 0.5\ L_0$. B) The difference in potential for three pinning stripe width and background composition combinations that give a preferential region with a width of $W_{pref} = 0.5\ L_0$.

simulations in Fig. 5.10A. As can be seen, the theoretical combinations are indeed near the minimum VWD, but there still appears to be some error present. This error is likely due to the UPLs being neglected in the simplified model. In order to better validate the simplified model, a series of simulations were built where the BCP chains that make up the UPL were replaced by homopolymer chains (such as is seen in Fig. 5.1C). In these simulations, a section of homopolymer separates PLs from each other. This removes any effect that the UPL might have, since the homopolymer is able to easily accommodate any morphology the PL desires to form, so that the only effect on the PL shape is the underlayer properties. These simulations were built using the same underlayers as before, and the measured VWD is shown in Fig. 5.10B. It can be seen that for these simulations, the simplified models prediction of the optimal background region composition and pinning stripe width appear to perfectly match with the minimum VWD. This shows the simple model is accurately capturing the physics of a system with no UPL present, meaning the simple model effectively captures the effect of the background region composition and pinning stripe width on the PL.

Since the only difference between Fig. 5.10A and B is the presence of the UPL in the simulation, observing the difference between these two results can help elucidate the effect that the UPL has on the PL. The first effect that can be seen is that with no UPL present, the VWD of the PL is in general higher than when the UPL is present. Lamellae will ideally have a constant width because otherwise there is increased interfacial area which has an energetic penalty. In a normal simulation (with no homopolymer), any variation in the width of one line must be accommodated by neighboring lines, which increases the energetic penalty and makes variations in the line width less likely. The homopolymer between PLs however can easily accommodate variations in the width of the PL with minimal energetic penalty, which explains why the measured VWD would be higher in Fig. 5.10B. This difference makes a direct comparison of the values of VWD between Fig. 5.10A and B unfair, though it is still possible to compare trends within one figure to the other.

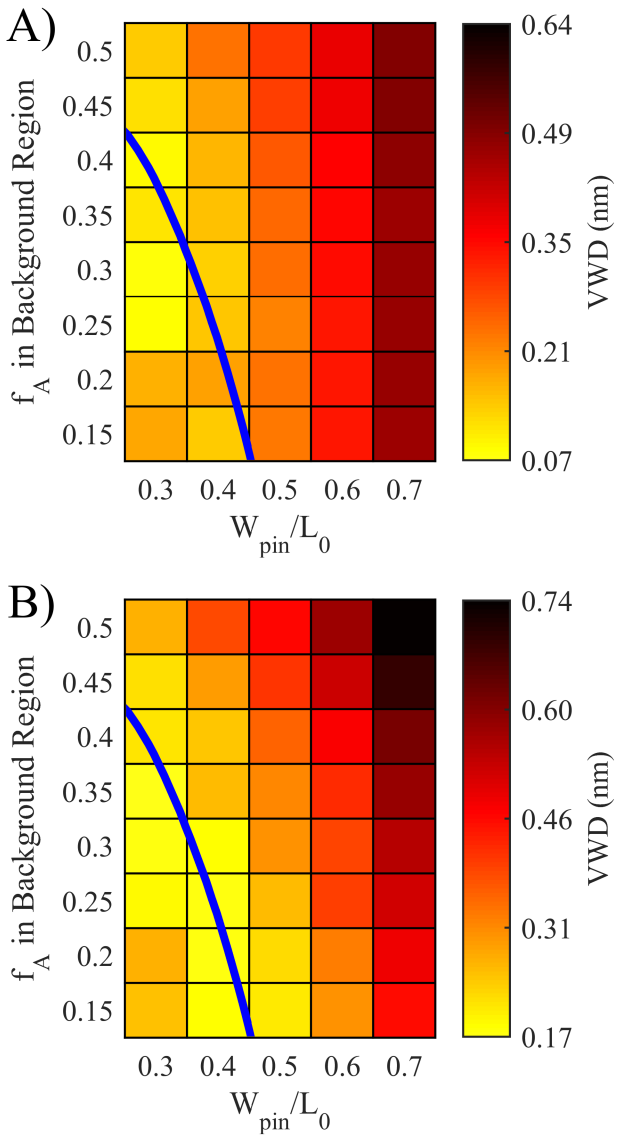

Figure 5.10: Plots of the standard deviation in the width through depth (VWD) for A) the pinned lines in a regular simulation and B) the pinned lines in a simulation where the lines are separated by a region of homopolymer in order to decouple the effects of the pinning stripe and the unpinned lines on the shape of the pinned line. The combinations of the background composition and pinning stripe width that theoretically give a preferential region width of $W_{pref} = 0.5\ L_0$ is shown by the blue line.

A second difference between Fig. 5.10A and B is that in general Fig. 5.10A does not show much dependence on the background composition for most pinning stripes, while in Fig. 5.10B there is a strong dependence on background composition. Figure 5.10B shows that making a more neutral background region with a larger pinning stripe (i.e. the upper right corner) increases VWD, while a more preferential background composition decreases VWD. This increase in VWD is due to the PL footing to a greater degree, which is due to the increased width of the preferential region predicted by the simplified model. However, this effect is not seen when the UPL is present in the simulation in Fig. 5.10A. This is due to the combination of two effects. First, at neutral compositions (higher f_A) the UPL would normally form straight sidewalls. This limits the ability of the PL to foot, leading to lower measured VWD at neutral compositions than is predicted by the simplified model. Second, at preferential background compositions, where the simplified model predicts the PL to form straighter sidewalls, the UPL desires to undercut. The UPL undercutting deforms the PL, causing it to have higher VWD than predicted. The combination of these two effects causes the measured VWD for the PL to be roughly constant with respect to background composition for larger pinning stripe widths.

5.3.3 Comparison of LER and line shape

In Fig. 5.11 a comparison is made between the effect of pinning stripe width and background composition on both LER (Fig. 5.11A) and on the variations in line width through depth (Fig. 5.11B). In both cases, the larger of either the pinned or the unpinned measurement is plotted, as this corresponds to the worst case scenario. LER is minimized when the background region is more preferential and the pinning stripe is either regularly sized or possibly oversized due to the increased guidance the underlayer exerts on the film. On the other hand, VWD is minimized with a more neutral background composition (which minimizes the undercutting of the unpinned line) and when the pinning stripe is smaller (minimizing the footing of the pinned line and approaching a preferential region of

$W_{pref} = 0.5\ L_0$). This shows that there is a tradeoff between LER and line quality through depth. Decreasing LER by making a more preferential background region increases the undercutting of the unpinned line, and decreasing LER by increasing the pinning stripe width increases the footing of the pinned line. This tradeoff should be kept in mind when designing new processes, and decisions on the underlayer properties should be chosen based on the requirements of the system, such as if LER or sidewall shape is more important to the process.

The BCP used in these simulations has a fairly high χ and low degree of polymerization, both of which can lead to lower LWR values. Therefore, while this work did not see a large effect of underlayer properties on LWR, for a lower χ BCP with a higher degree of polymerization, LWR might need to optimized in addition to LER and the VWD.

5.4 Conclusions

Simulations were run to analyze the quality of lines formed on flat chemoepitaxial guiding underlayers with varying composition of the background region and width of the pinning stripe, while keeping a constant repeat distance of $W_{pattern} = 2\ L_0$ (2x density multiplication). It was found that decreasing the width of the pinning stripe increases the LER of the lines because the lines have less energetic penalty for the center of the pinned line to deviate from the center of the pinning stripe. As the background region becomes more neutral to both blocks of the BCP, the LER also increases due to the smaller energetic penalty for the pinned line to be above the background region instead of the pinning stripe. The underlayer properties were found to have little effect on the LWR of the resulting film.

As the composition of the background region becomes more preferential to one of the blocks, the amount of undercutting in the unpinned line increases. As the width of the pinning stripe increases, the amount of footing of the pinned line increases. It was additionally found that with a neutral background region composition and a pinning stripe width of $W_{pin} = 0.5\ L_0$ (the width of the pinning stripe is commensurate with the nom-

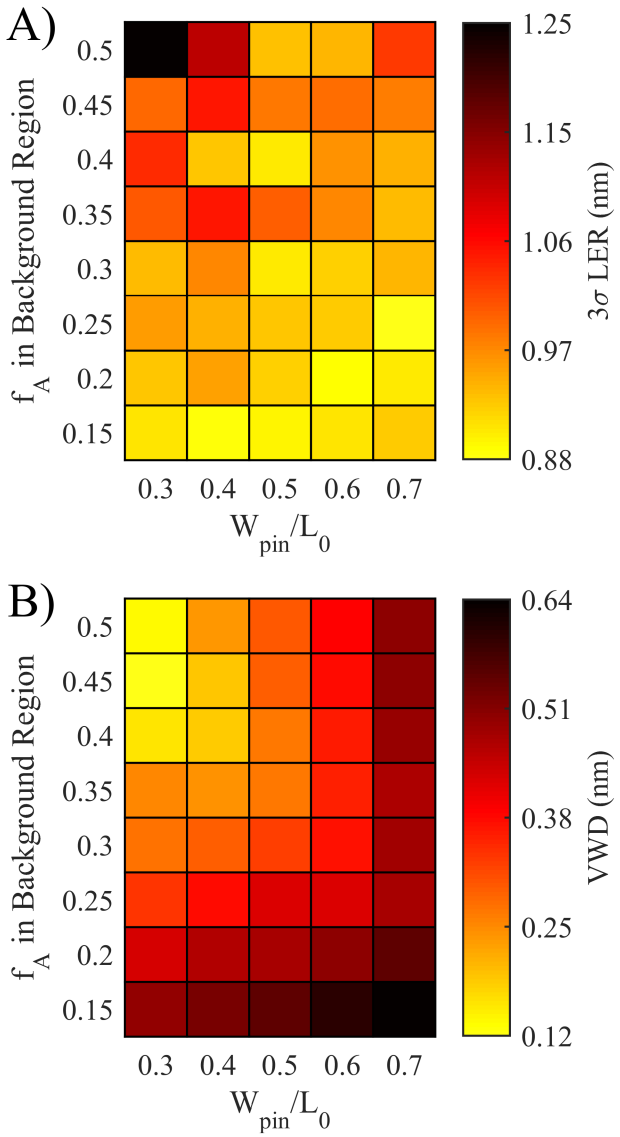

Figure 5.11: A comparison in the effect of pinning stripe width and background composition on A) LER and B) variations in line width through depth (VWD). In both cases, the value with the higher LER or line width variation through depth between the pinned and the unpinned line was plotted.

inal width of one line) the pinned line still exhibited footing. A simple model to explore this effect was discussed, and the cause was found to be that the pinning stripe creates a preferential region that is slightly wider than the pinning stripe. The cooperative effect that the unpinned and pinned lines have on respective undercutting and footing was found to be very significant in determining an optimal background composition and pinning stripe width.

When determining the optimal background composition and pinning stripe width, multiple factors must be considered. Parameters must be chosen such that the underlayer is able to guide the BCP film to a defect free state. Furthermore, parameters should be chosen to minimize the LER of the formed lines, which can be achieved by increasing the guidance of the system by making the background region more preferential and the pinning stripe near the optimal width of $W_{pin} = 0.5\ L_0$. The shape of the sidewalls of these lines also needs to be considered: it was found that an undersized pinning stripe and a more neutral background region give the straightest sidewalls. The optimal conditions for LER and line quality are in conflict, so some compromise will have to be made depending on the requirements of the process when choosing processing conditions.

5.5 Acknowledgements

We would like to acknowledge Intel for funding the initial stages of this research and funding the building of the GPU cluster used to run the simulations.

CHAPTER 6
BLOCK COPOLYMER DIRECTED SELF-ASSEMBLY USING CHEMOEPITAXIAL GUIDING UNDERLAYERS WITH TOPOGRAPHY

6.1 Introduction

In recent years, a few hybrid approaches to guiding underlayers in block copolymer directed self-assembly (BCP DSA) have been introduced. These underlayers combine principles of both chemoepitaxy (Section 1.3.2) and graphoepitaxy (Section 1.3.1). There are three specific processes that produce hybrid underlayers like these. First, it is now believed that the LiNe process flow produces underlayers that have some topography in them.[54, 55] Here, the pinning stripes are raised, with the region beside the pinning stripe sloping to meet them. Additionally, it is thought that the pattern produced is triple toned, meaning there is a neutral background region, a preferential pinning stripe, and an oppositely preferential sloped sidewall. Here, the BCP covers the underlayer entirely, unlike in a traditional graphoepitaxial system. A second hybrid approach is that produced by the SMART process.[56] These underlayers are more similar to graphoepitaxial systems in that they have straight sidewalls for the topography produced, however here the BCP is also present on top of the mesas. The trenches and the mesas here must both be an integer multiple of the BCP pitch. The BCP will align inside the trench as is done in graphoepitaxy. The BCP inside the trench will then provide guidance to the BCP on top of the mesa. Finally, a third hybrid approach is that produced by the COOL process.[57] The COOL process makes an underlayer similar to those produced by the simplified LiNe process, except the pinning stripe is raised and has preferential sidewalls.

While much work has been done experimentally on these hybrid approaches,[54, 55, 56, 57, 58] little has been done in simulation. Therefore in this chapter the coarse-grained

molecular dynamics model will be used to explore various aspects of these hybrid underlayers. This includes geometric factors such as the height, width, and shape of the topographic features. The chemical factors will also be explored, meaning the chemical preference of both the top of the mesa and the bottom of the trench. In all these factors, the defectivity of the resulting BCP film will be measured to test the performance of the underlayer.

6.2 Model

The underlayers used in this work are built as a cross-linked mat, described in detail in Section 2.2.2. These underlayers are "carved" into the desired shape. The minimum height of the underlayer (meaning the distance from the bottom of the underlayer to the bottom of a trench) was set to 4 nm (the cut-off for non-bonded interactions). Two examples of this carving can be seen in Fig. 6.1.

The chemical preference of the underlayer was controlled by altering the composition of various regions of the underlayer. The underlayer was composed of the same type beads as the BCP film itself. To alter how preferential a region of the underlayer was, the number fraction of A beads in the region ($n_{A,region}$) was varied. With a number fraction of zero, there are no A beads in that region, only beads of type B. Therefore, this region will be preferential to the B type beads in the film as long as $\chi > 0$. To make a neutral region, the number fraction is set to 0.5.

The different regions of the underlayer are illustrated in Fig. 6.1. These regions of chemical preference are called the top, the sidewall, and the bottom (denoted by subscripts t, s, and b respectively). These regions are separated in Fig. 6.1 by bold black lines. It is important to note that these regions of chemical preference are likely not this shape in experiment. However, this is done in simulation since this is the ideal achievable chemical preference. Additionally, the regions near the center of the topographic features will only be minimally felt by the film due to the cutoff in the non-bonded interactions.

Polymer thin films are generated as described in Section 2.2.2. These films are designed

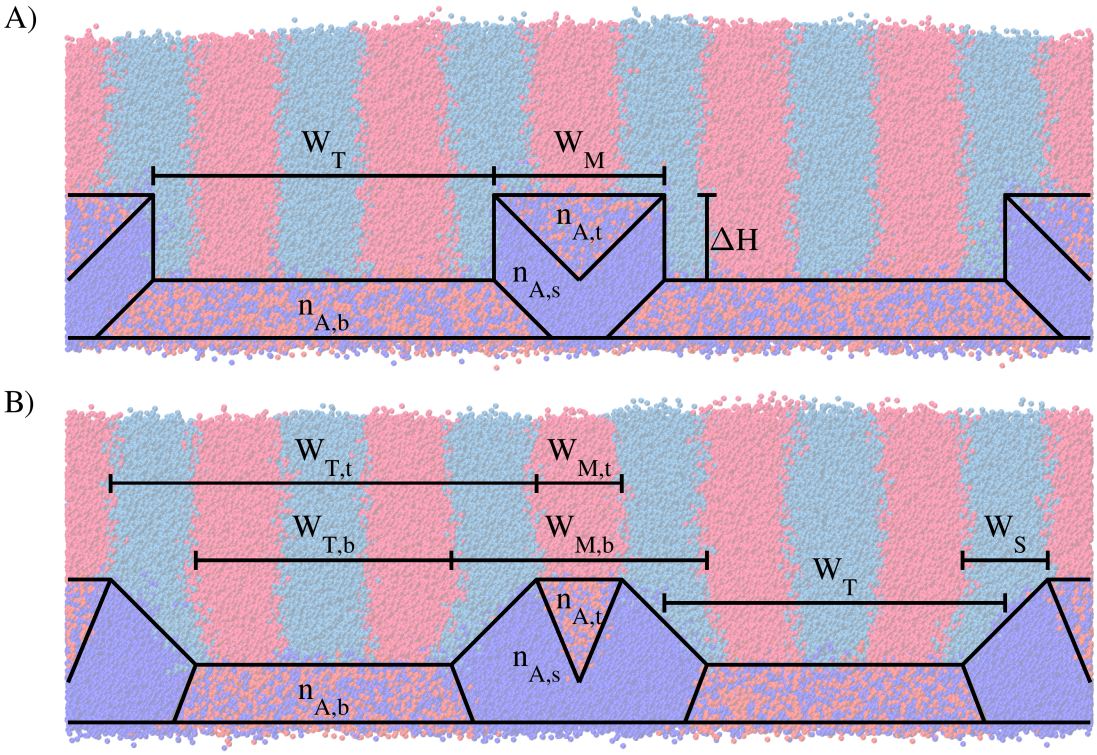

Figure 6.1: Example cross-sections of typical simulations, labeling all relavant parameters varied in this work. The underlayer beads are shown in darker blue and red while the film beads is shown in lighter blue and red. Blue indicates A beads, red indicates B beads. A) An example of an underlayer with straight sidewalls. B) An example of an underlayer with sloped sidewalls.

such that the film will always be $0.75\ L_0$ thick above the top of the topography. Therefore, the initial film was built thick enough to account for all the BCP that would fill in the trenches of the topography.

Simulations are run in two minimizations steps and two molecular dynamics steps. The two minimization steps are as described in Section 2.3.1. Molecular dynamics are run under NVT conditions as described in Section 2.3.2. The first molecular dynamics step is run for 200,000 timesteps (10 ns) at $T = 500$ K and with $\varepsilon_{AB} = 0.5$ kcal/mol (where $\chi = 0$). This step allows the film time to collapse to the underlayer, filling in the topographic features while still mixed. The second molecular dynamics step is run for 2,000,000 timesteps (100 ns) with $\varepsilon_{AB} = 0.35$ kcal/mol (where $\chi = 0.67$). In this step the BCP undergoes DSA. The final simulation state is then output to be analyzed.

The defectivity of the final simulation state is analyzed and the defectivity is measured (as described in Section 2.5.2). Since this is a molecular dynamics simulations, this measurement is just a kinetic snapshot of the defectivity. Further annealing time should lower defectivity further. This measurement merely reveals which underlayers get to lower defectivity in a short simulated annealing time. However, since free energy measurements suggest that defects in BCP DSA are largely kinetically trapped,[24, 25] this kinetic snapshot of defectivity is of value. It is important to note that for most of this work only the surface level defectivity is considered, meaning only the portion of the film above the top of the topography. While the lamellae within the trenches generally have a defectivity lower than or equal to the defectivity of the surface lamellae, they may have an undesirable through film shape that will make pattern transfer difficult.

6.3 Results and Discussion

Simulations were run varying many aspects of the geometry and the chemical preference of topographic features of the guiding underlayer. In all cases, the defectivity of the films after 100 ns simulations was measured in order to see the relative effectiveness of the

guiding underlayer. While this measurement is not of the equilibrium state, it does give some information as to the ability of underlayers to either anneal out defects or prevent the initial formation of defects, which is of great value. It should be noted that while this is 100 ns of simulation time, this is likely a longer amount of actual annealing time since the coarse-graining increases the actual diffusion rate of the polymers. The discussion of the underlayers will be broken into two main sections, underlayers with vertical sidewalls, and underlayers with sloped sidewalls.

6.3.1 Vertical Sidewalls

Height of Topographic Features

The first factor to look at when considering the geometry of the guiding underlayer is the height of topographic features. Here, simulations were run to measure the defectivity of films as a function of the topographic height (ΔH). This was done for underlayers with vertical, preferential to A ($n_{A,s} = 1$) sidewalls and a neutral top and bottom ($n_{A,t} = 0.5$ and $n_{A,b} = 0.5$). These results are shown in Fig. 6.2, with Fig. 6.2A showing the defectivity of the film above the top of the topography, while Fig. 6.2B shows the defectivity of the BCP within the trenches of the topography. Since the top of the film does interact with the film inside the trench, these two measurements are not entirely disconnected. Rather, a low defectivity in the trench should help lower the defectivity in the top portion of the film. Additionally, if the top of the film is highly defective, it will likely increase the defectivity of the film inside the trench despite the guidance of the trench sidewalls.

Three different underlayer styles were looked at. First, a 2x density multiplying underlayer (with a trench width of $W_T = 1\ L_0$ and a mesa width of $W_M = 1\ L_0$) was explored. Here, the defectivity is initially high with little topographic height ($\Delta H \rightarrow 0\ L_0$). As the topographic height increases, the defectivity begins to decrease. This is due to preferential, vertical sidewalls gaining more surface area as the height increases, thus increasing the guidance of the system. Initially there is little sidewall, therefore the underlayer is insuffi-

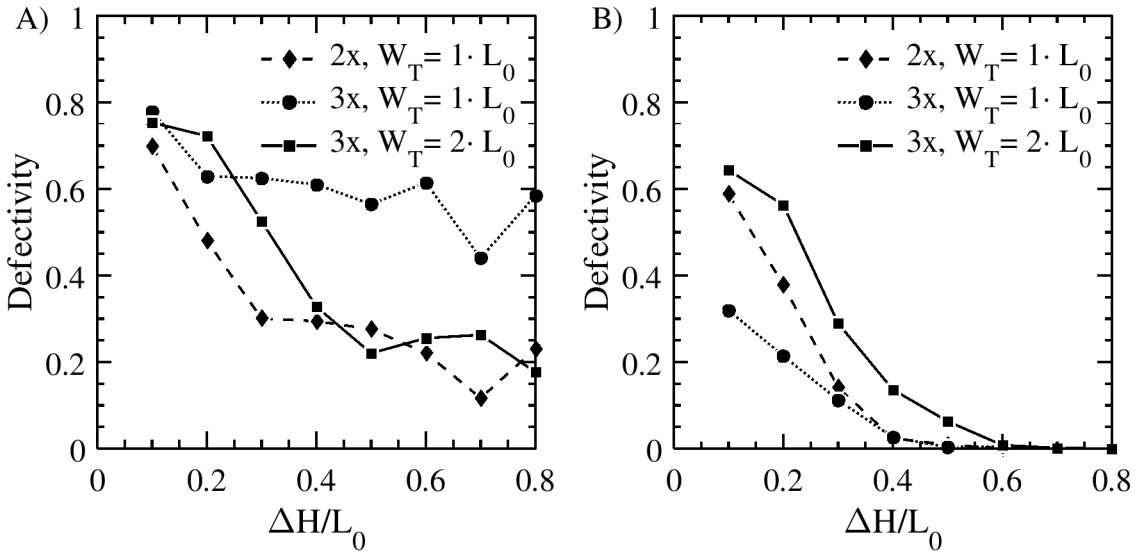

Figure 6.2: A) The defectivity of the BCP film above the top of the mesa versus topographic height for three different underlayer styles. B) The defectivity of the BCP film inside the trenches versus topographic height for three different underlayer styles.

cient to properly align the film. As the height increases, the sidewalls can sufficiently pin down the appropriate block, leading to a defect free pattern of the film within the trench (see Fig. 6.2B at $\Delta H > 0.4\ L_0$). This then helps guide the remain BCP above the topographic feature into a defect free state. Once the topographic height is sufficiently high to eliminate defects within the trench, further increases should have little benefit. This appears to be true in Fig. 6.2A for the 2x case. The defectivity leveling off at larger ΔH, while making it more difficult to reach extremely low defectivities, does have two benefits. First, larger topographic features will require more material to make which will add some cost. Second, and more important, taller topographic features will have a worse aspect ratio, thus making the pattern more difficult to fabricate due to the possibility of pattern collapse. Therefore, in this style of underlayer it is desirable to target as short a topographic feature as possible that still lowers the defectivity sufficiently.

The other two cases that were considered were for a 3x density multiplying underlayer, one with a narrow trench ($W_T = 1L_0$, $W_M = 2L_0$) and one with a wide trench ($W_T = 2L_0$,

$W_M = 1\ L_0$). From this data it can be seen that for a 3x underlayer it is far worse for defectivity to have a narrow trench than a wide trench. While the 2x case and the narrow trench 3x case have the same trench width ($W_T = 1\ L_0$) and a similar behavior of the BCP inside the trench (Fig. 6.2B), the 2x case has far lower defectivity. This suggests that it is difficult for the narrow trench 3x case to induce order in the BCP film above the mesa. On the other hand, the wider trench 3x case reaches fairly low defectivities quickly. This occurs despite the defectivity inside the trench of the wide trench 3x case lagging behind the defectivity of either the 2x case or the narrow trench 3x case. In this case, since the trench is wider ($W_T = 2\,L_0$) a larger topographic feature is required to effectively guide the BCP inside the trench to a defect free state. However, once a defect free state is obtained in the trench, the order only need propagate the relatively short distance across the mesa ($W_M = 1\ L_0$), as it does in the 2x case. This is why the defectivity of the wide trench 3x case follows a similar trend to the 2x case, just offset to account for the additional height needed to order the film inside the trench. This will be discussed in further detail in Section 6.3.1.

Trench Width

General Defectivity versus Trench Width Curve

The defectivity was measured as a function of the width of the trench for both a 2x and 3x density multiplication. This was done here using underlayers with neutral top and bottom surfaces ($n_{A,t} = 0.5$ and $n_{A,b} = 0.5$), preferential sidewalls ($n_{A,s} = 1$), and a topographic height of $\Delta H = 0.5\ L_0$. Only ten replicates of each simulation were run for this series. These results are shown in Fig. 6.3.

As is expected, the defectivity generally reaches a minimum when the trench width is commensurate with an integer multiple of the BCP pitch (L_0). Additionally, it appears the trench width can vary approximately 10% from an integer multiple of the pitch before defectivity increases for this BCP. At an integer multiple of the pitch, the width of the trench

allows the formation of defect free vertical lamellae. However, if the trench is mis-sized, the lamellae must either compress or stretch in order to form in the proper orientation within the trench. Both stretching lamellae and compressing lamellae raise the free energy of vertical lamellae.[59] This increase in the free energy makes competing states more favorable for the system. There are two primary competing states. First, there is the "ladder" state, where instead of the lamellae forming parallel to the sidewalls, they form perpendicularly.[21] Since the repeat direction of the lamellae is now in the direction of the trench, the stress is removed. A second state would be the "horizontal" state. Here, the lamellae will lay down (forming parallel to the floor of the trench). Since the repeat direction of the lamellae is now normal to the base of the trench, the stress is again removed. It should be noted that this state is also likely stabilized by the height of the topographic features here being $\Delta H = 0.5\ L_0$ which is commensurate with a half domain of lamellae. Altering the topographic height so that it is incommensurate with a half pitch would likely destabilize this orientation.

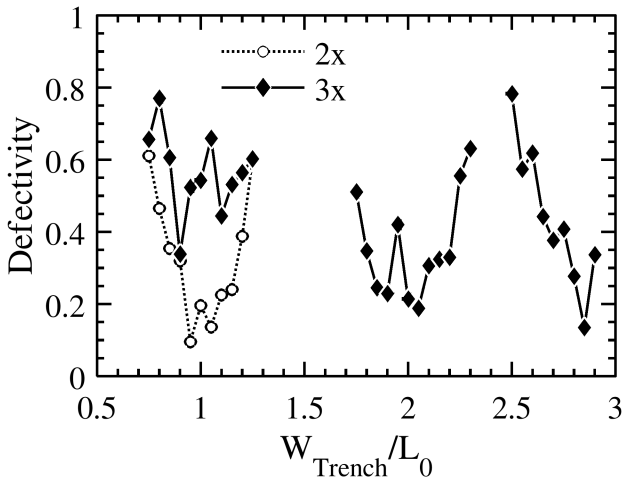

Figure 6.3: Defectivity data for two different density multiplications versus trench width with vertical preferential sidewalls and a topographic height of $\Delta H = 0.5\ L_0$.

The 3x density multiplication data in both Fig. 6.2 and Fig. 6.3 shows that a trench width of $W_T \approx 2\ L_0$ has far lower defectivity than $W_T \approx 1\ L_0$. This raises the question of

what the optimal width of the trench and mesa would be for higher density multiplications. It is hypothesized here that the ideal choice of trench and mesa widths is that which best separates the "guiding regions" of the underlayer. The region of guidance for this variety of underlayer is inside the trench, beside the guiding sidewall. If it is assumed this region of guidance is centered a half chain away from the sidewall (or a distance of $L_0/4$), then the separation distance between guiding regions is equal to

$$S_T = W_T - L_0/2, \quad S_M = W_M + L_0/2 \tag{6.1}$$

where S_i is the separation distance between the guiding regions across the trench or mesa (T of M respectively). In order to maximize the separation between the guiding regions, these two separation distances should be equal, or the difference between S_T and S_M needs to be as close to zero as possible. By substituting in the defintitions of S_T and S_M it can be seen that

$$S_T - S_M = W_T - W_M - L_0 \tag{6.2}$$

The only condition where $S_T - S_M = 0$ is when $W_T = W_M + L_0$. For an odd density multiplication (nx) this can be done while W_T and W_M are integer multiples of L_0 (the conditions that minimize defectivity) if

$$W_T = \left(\frac{n-1}{2} + 1\right) \times L_0, \quad W_M = \frac{n-1}{2} \times L_0. \tag{6.3}$$

For a 3x density multiplying underlayer, this results in $W_T = 2\ L_0$ and $W_M = 1\ L_0$ as was shown to be the lower defectivity case in both Fig. 6.2 and Fig. 6.3. However, for an even density multiplication, no integer multiples of L_0 satisfy this condition. The value of $S_T - S_M$ that is closest to zero occurs in the following two conditions,

$$W_T = W_M = \frac{n}{2} \times L_0, \tag{6.4}$$

$$W_T = \left(\frac{n}{2} + 1\right) \times L_0, \quad W_M = \left(\frac{n}{2} - 1\right) \times L_0. \tag{6.5}$$

It is suspected that the conditions in Eq. (6.5) will be superior to Eq. (6.4) since it shortens the width of the mesa while expanding the width of the trench, though more simulation work at larger density multiplications needs to be done to confirm this.

COOL Process

There is a process flow for designing guiding underlayers that use both chemoepitaxy and graphoepitaxy known as the COOL process.[57] The geometry of these underlayers are similar to those discussed here, but specifically with a mesa width of $W_M = 0.5\ L_0$ and a trench width of $W_T = n\ L_0 - W_M$ where n is the degree of density multiplication. For a 3x density multiplying underlayer this would be the case where $W_T = 2.5\ L_0$. Using the COOL process, reasonably defect free lamellae arrays have been obtained experimentally.[57] However, as can be seen in Fig. 6.3, this is an underlayer that appears to maximize the defectivity of the films in this model.

There are a few possible reasons for this discrepancy which will be detailed here. First, the experimental COOL processes are typically done with a higher density multiplication than used here. This gives a much larger area over which the stress of compressing the lamellae in the trench can be distributed. With a density multiplication of 5x, the width of the trench can vary by approximately $0.5\,L_0$ before defectivity increases assuming the 10% tolerance found above is true. This would allow a trench width of $W_T = 4.5\ L_0$, which would be the condition for the COOL process.

Second, the topographic features made experimentally by the COOL process may be slightly different than what is thought. As suggested in Fig. 6.3, as $W_T \rightarrow 3\ L_0$, the defectivity lowers. As the trench widens (and therefore the mesa narrows) the lamellae are not being compressed as much within the trench. Additionally, the lamellae wetting the sidewalls does not have to contort as much to meet above the topography. This drives down

defectivity.

An additional possibility is that instead of undersizing the mesa, the COOL process may instead be altering the shape. Instead of making a rectangular relief pattern, the shape of the topography could either have a domed top or be more triangular in shape (see Fig. 6.4B). A triangular topography was specifically probed in recent papers.[58] Additionally, using this model it was found that a film could reach fairly low defectivities using a triangular topography. This is shown in Fig. 6.4A where the defectivity was measured as a function of the width of the base of triangular guiding features. Defectivity is generally low in this case unless the base of the mesa was too wide ($W_{M,b} = 1L_0$) or too narrow ($W_{M,b} \rightarrow 0L_0$). With too narrow a base, the guiding topographic feature is so thin it is near being nonexistent. Because of the thinness of the feature, it will exert less potential/force, thus guiding the film less. With too wide a base there are two factors that increase defectivity. First, the lamellae are being compressed more near the base of the topography, increasing defectivity. Second, since the same topographic height is being used here ($\Delta H = 0.5\ L_0$), increasing the width of the topographic feature makes a far shallower slope for the triangle. This in turn makes the lamellae pinned by the sidewalls orient more like a horizontal lamellae, which would make that competing morphology be more stable.

With these triangular morphologies, the lamellae wetting the two sides of the triangle merge at the peak of the triangle and then proceed vertically upward from there. This is a very smooth transition in comparison to that done by the rectangular topographic feature that was discussed earlier, and is likely part of why the triangular morphology tends to have lower defectivities. Additionally, while the triangular morphology may compress lamellae more near the base of the triangle than the rectangular morphology does throughout the trench, this highly compressed region is relatively small, and the stress is quickly relieved when moving further up through the film. Finally the triangular topography will likely be far more structurally resistant to things such as pattern collapse during fabrication than the rectangular features. For all of these reasons, it is likely that a more triangular topography

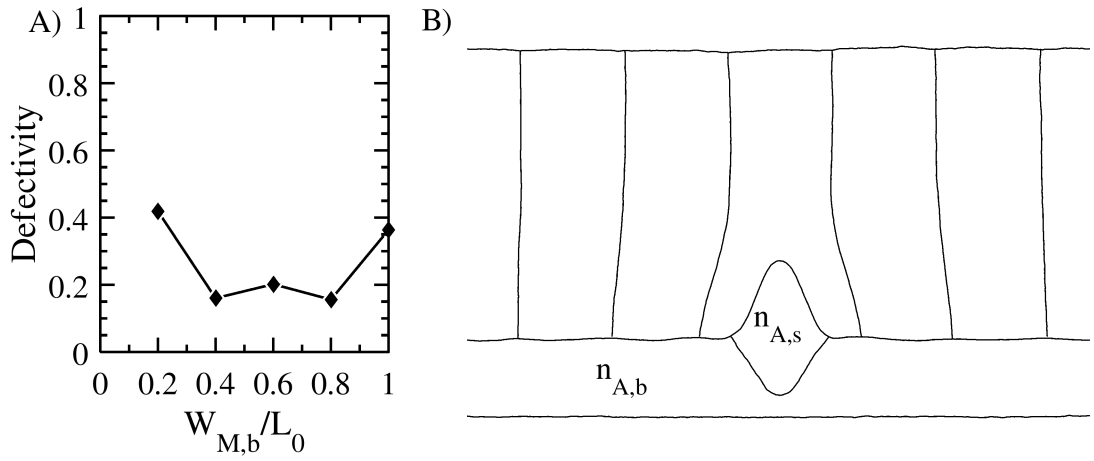

Figure 6.4: A) Defectivity data versus the base width of the mesa for a triangular morphology. B) The average cross-sectional shape of lamellae formed on underlayers $W_{M,b} = 0.6\ L_0$. Black lines indicate the location of interfaces between different regions.

may be better for use in topographic guiding underlayers than narrow rectangular features.

Preference of Underlayers

Another important factor in the design of these hybrid underlayers is the chemical preference of the different regions. Here, the chemical preference of the top of the mesa and the bottom of the trench are considered. These results are shown in Fig. 6.5. In Fig. 6.5A the composition of the bottom of the trench was held neutral ($n_{A,b} = 0.5$) while the composition of the top of the mesa was varied from preferential to B ($n_{A,t} \rightarrow 0$) to preferential to A ($n_{A,t} \rightarrow 1$). In Fig. 6.5B the composition of the top of the mesa was held neutral ($n_{A,t} = 0.5$) while the composition of the bottom of the trench was varied from preferential to B ($n_{A,b} \rightarrow 0$) to preferential to A ($n_{A,b} \rightarrow 1$). This was done for both a 2x density multiplying underlayer (with $W_T = 1\ L_0$ and $W_M = 1\ L_0$) and a 3x density multiplying underlayer (with $W_T = 2\ L_0$ and $W_M = 1\ L_0$).

In all cases, there is a window for lower defectivity when closer to a neutral composition ($n_A = 0.5$), while the defectivity will increase at extremely preferential compositions ($n_A = 0$ or $n_A = 1$). This is to be expected since extremely preferential regions will

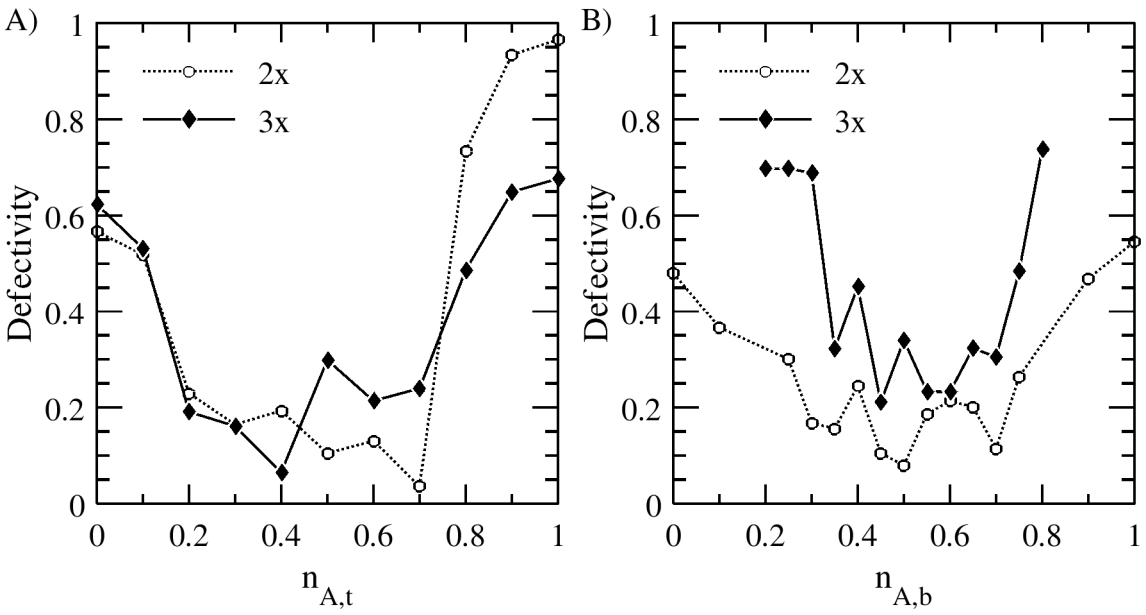

Figure 6.5: Defectivity data versus A) the number fraction of A beads in the top of the mesa ($n_{A,t}$) and B) the number fraction of A beads in the bottom of the trench ($n_{A,b}$). These results are shown for both a 2x density multiplication and a 3x density multiplication with $W_T = 2\ L_0$ and $W_M = 1\ L_0$.

encourage the formation of horizontal lamellae, while neutral compositions allow for the formation of vertical lamellae. In general, these lower defectivity windows correspond well to the compositions where lamellae form vertially on flat, unpatterned underlayers. For the BCP used here on a flat substrate, the composition window is $0.30 > n_A > 0.70$ for a commensurate film thickness ($1\ L_0$) and $0.25 > n_A > 0.75$ for an incommensurate film thickness ($0.75\ L_0$). This is in good agreement with the data shown in Fig. 6.5.

Varying the composition of the bottom of the trench has a far weaker effect on defectivity in the 2x density multiplying case than the 3x density multiplying case. This is due to the trench being far wider in the 2x case ($W_T = 1\ L_0$) than the 3x case ($W_T = 2\ L_0$). Because of this, the guiding sidewalls have far more power in the 2x case to overpower the preferential bottom of the trench. However, in the 3x case, since the sidewalls are further apart the horizontal lamellae morphology is far more favorable since the preferential trench bottom is so wide. Both the 2x and 3x cases have similar windows for low defectivity when

varying the composition of the top of the mesa. This is likely due to the width of the mesa being the same in these two cases ($W_M = 2\ L_0$). If the mesa were wider, it is suspected that the window for low defectivity would be narrower.

Within the lower defectivity windows there appears to be little dependence of defectivity on chemical preference. All variations are well within the noise, with the possible exception of the 2x density multiplication while varying the composition of the top of the mesa. Here, the defectivity appears to decrease until $n_{A,t} = 0.7$, after which the defectivity drastically increases. It is suspected this is due to how the chemical preference of the underlayer is made in the simulation. Beads near the border between the sidewall and the top of the mesa will feel both regions. Therefore, making the top of the mesa slightly preferential to the same type of bead as the sidewall will increase the guidance of the sidewall, lowering defectivity. While this is likely an artifact of the simulation, a similar phenomenon is likely to occur in real systems.

6.3.2 Sloped Sidewalls

General Results

To this point, the sidewalls of the topography have all been perfectly vertical. However, perfectly vertical sidewalls may be difficult to manufacture. Therefore, simulations were run to test how having a sloped sidewall would affect DSA. The first group of simulations were run with a constant topographic height ($\Delta H = 0.5\ L_0$) while varying the average width of the trench, $W_T = (W_{T,t} + W_{T,b})/2$, and the width of the sidewalls, $W_S = (W_{T,t} - W_{T,b})/2$, for a 3x density multiplying underlayer. These results are shown in Fig. 6.6.

Along the horizontal $W_S = 0\ L_0$ the sidewalls are vertical, and the data given is the same as that in Fig. 6.3. It can be seen that the defectivity can actually lower when the sidewalls become sloped, such as when $W_T = 2\ L_0$ and $W_S = 0.5\ L_0$ ($W_{T,b} = 1.5\ L_0$ and $W_{T,t} = 2.5\ L_0$). This case is of interest because the width of the trench at both the

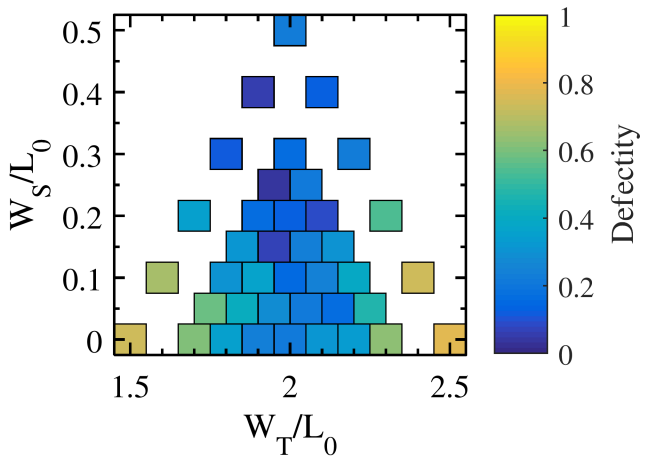

Figure 6.6: Defectivity data for simulations with sloped sidewalls. The defectivity is plotted versus the width of the sloped sidewall ($W_S = (W_{T,t} - W_{T,b})/2$) and the average width of the trench ($W_T = (W_{T,t} + W_{T,b})/2$).

bottom and top are extreme enough that the defectivity would be high if the sidewalls were vertical in either case. This helps suggest that the important parameter is the average width of the trench. Another observation about this specific situation is that that the width of the sidewalls are both the same as the width of one lamellae ($W_S = 0.5\ L_0$). Therefore, when looking from a top down view, this pattern looks similar to a traditional chemoepitaxial guiding underlayer, except with two pinning stripes.

It should be noted that BCP chains are pinned down in a very different fashion here than they are with straight sidewalls. With a straight sidewall, half of a BCP chain is pinned against the sidewall, with the chain generally oriented normally to the sidewall surface (as can be seen in Fig. 6.1A). Here only half a lamellae is being pinned, though it is pinned along a significant portion of its length. This was also the case with the triangular morphology as shown in Fig. 6.4B. This is how a traditional graphoepitaxial guiding underlayer pins down lamellae. However, with a sufficiently sloped sidewall, the chains are oriented parallel to the sidewall surface, causing the lamellae formed to initially propagate normal to the sidewall (as can be seen in Fig. 6.1B or later in Fig. 6.9B). Here both halves of the lamellae are being pinned (half a chain from each side), and therefore only

the base of the lamellae is being pinned by the sidewall. This is similar to how a purely chemoepitaxial guiding underlayer pins down lamellae. Therefore, by altering the slope of the guiding sidewall, these hybrid underlayers can transition from being more graphoepitaxial to chemoepitaxial. Due to this, it is expected many of the previous results (altering the height of the topography, altering the chemical preference of various regions) may be different with sloped sidewalls.

It is important to note that these underlayers with sloped sidewalls will necessarily deform the lamellae within the trenches. Examples of this can be seen in Figs. 6.1B, 6.4B, and 6.9B. These deformations may increase the difficulty subsequent of pattern transfer steps.

While the majority of this work has been done assuming $W_{T,b} < W_{T,t}$ (where the sidewall that creates a foot for the mesa), a couple instances where $W_{T,b} > W_{T,t}$ (where the sidewall undercuts the mesa) were run. It was found that a straight sidewall ($W_{T,b} = W_{T,t} = 2\ L_0$) had a relatively low defectivity value of 0.2135. However, the defectivity increased to 0.4457 when the underlayer had a slight undercut ($W_{T,t} = 2\ L_0$ and $W_{T,b} = 1.9\ L_0$) This suggests it is bad to have a sidewall that undercuts the mesa.

Height of Topography

Simulations were run in order to determine the optimal height of the topographic features for underlayers with sloped sidewalls. Three cases were considered with varying sidewall widths ($W_S = 0.5\ L_0$, $0.4\ L_0$, and $0.4\ L_0$ respectively) and varying chemical preference of the bottom of the trench ($n_{A,b} = 0.5$, 0.5, and 0.35 respectively). These results are shown in Fig. 6.7. Here, all three cases show a similar behavior, with a minimum in the defectivity occuring somewhere in the range of $0.1 > \Delta H > 0.3$.

The defectivity increases at large topographic heights for two main reasons. First, the area of the sidewall wet by the pinned lamellae increases in width, W_{eff}, meaning the hypotenuse of the guiding sidewall (where $W_{eff} = (W_S^2 + \Delta H^2)^{1/2}$). Since this effective

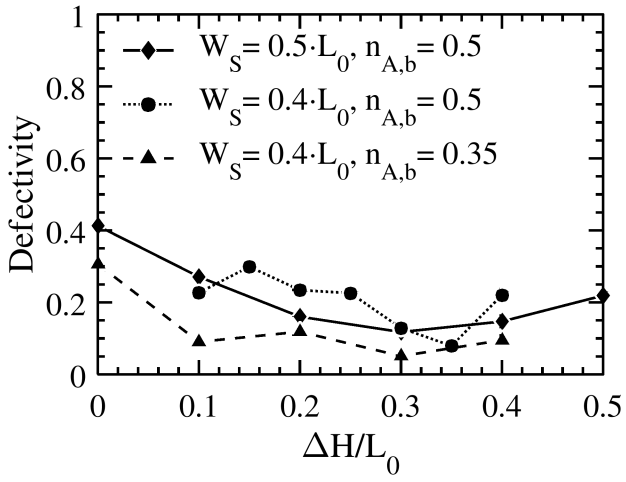

Figure 6.7: Defectivity of sloped sidewall simulations versus topographic height. Simulations were run for two different pinning stripe widths and two different preferences of the bottom of the trench.

width increases, the pinned lamellae will become more stretched at its base which will increase defectivity. For the wider sidewall ($W_S = 0.5\ L_0$) the effective width of the sidewall is always $W_{eff} \geq 0.5\ L_0$. On the other hand, for the thinner sidewall ($W_S = 0.4\ L_0$) the effective width of the sidewall will be equal to a half pitch when the height is $\Delta H = 0.3\ L_0$, which is approximately where the minimum in defectivity occurs. This suggests the ideal shape of the topographic features is one which makes the effective width of the sidewall the width of one lamellae.

Second, as the height increases, the lamellae within the trench begin to be compressed. Since the lamellae pinned to the sidewall initially orients normal to the sidewall, any lamellae within the trench will be slightly compressed to accomodate the pinned lamellae's direction. Related to this, the lamellae on top of the mesa will initially be stretched. One possible solution to this problem is to move the sidewalls closer together by slightly expanding the trench (W_T), though further work needs to be done to validate this theory.

Preference of Underlayer

With straight sidewalls it was found that the bottom of the trench should ideally be more neutral (Fig. 6.5B). However, with sloped sidewalls it can be seen (Fig. 6.7) that the series with a slightly preferential trench bottom ($n_{A,b} = 0.35$) performed better than those with a neutral trench bottom ($n_{A,b} = 0.5$). This is logical since the sloped sidewall simulations have more similarities with purely chemoepitaxial underlayers. It has been shown that with chemoepitaxial guiding underlayers, defectivity decreases when the background region (analogous to the bottom of the trench here) is slightly preferential to the block of the BCP that is not preferred by pinning stripe[47] (analogous to the guiding sidewall here). This occurs because the increased contrast between the bottom of the trench and the guiding sidewall better pins down lamellae, increasing guidance and lowering defectivity. The same phenomenon can be seen in Fig. 6.8 where the lowest defectivity occurs when $n_{A,b} \approx 0.3$ or 0.4, where the bottom of the trench is slightly preferential to the block not guided by the sidewalls.

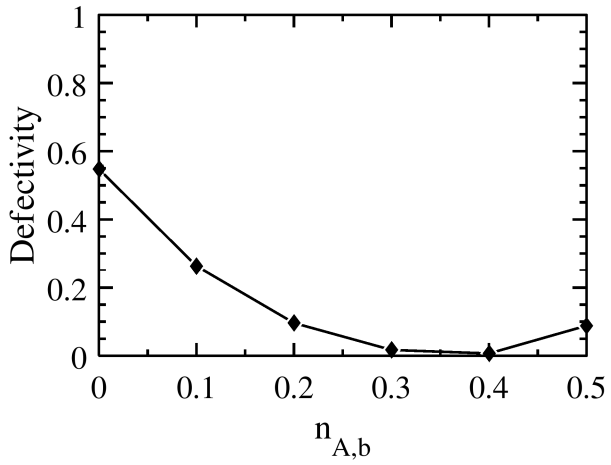

Figure 6.8: Defectivity versus the chemical preference of the bottom of the trench ($n_{A,b}$) for a sloped sidewall simulation. All simulations have $W_{T,b} = 1.5\ L_0$, $W_{M,t} = 0.5\ L_0$, $\Delta H = 0.5\ L_0$, $n_{A,t} = 0$, $n_{A,s} = 1$

The effect of varying the composition of the top of the mesa can be seen in Fig. 6.9A

for a 3x density multiplying underlayer with $W_{T,b} = 1.5\,L_0$, $W_{M,t} = 0.5\,L_0$, $W_S = 0.5\,L_0$, $\Delta H = 0.2\,L_0$, and $n_{A,b} = 0.5$. When $n_{A,t} \to 1$ the defectivity drastically increases. Here there is a very wide section of the underlayer that is strongly preferential to one block which leads to the lamellae forming horizontally. This should not happen as easily with a larger amount of topography in they system, but with $\Delta H = 0.2\,L_0$ horizontal lamellae can still form. On the other hand, when $n_{A,t} \to 0$ the underlayer is three toned and has a high amount of guidance, decreasing defectivity. In Fig. 6.9B it can be seen that the shape of this lamellae varies with the preference of the top of the mesa. When the mesa is preferential to B ($n_{A,t} = 0$, red lines) the interface of the lamellae meet up with the interface between the sidewall and the top of the mesa. On the other hand, when the mesa is more neutral ($n_{A,t} = 0.5$, black lines) the interface of the lamellae begins to bend, forcing the lamellae above the top of the mesa to form a more U like shape. In theory, when the top of the mesa is more preferential to A ($n_{A,t} \to 1$) the bending of this lamellae on top of the mesa will become more extreme, until eventually horizontal lamellae form as was seen in Fig. 6.9A.

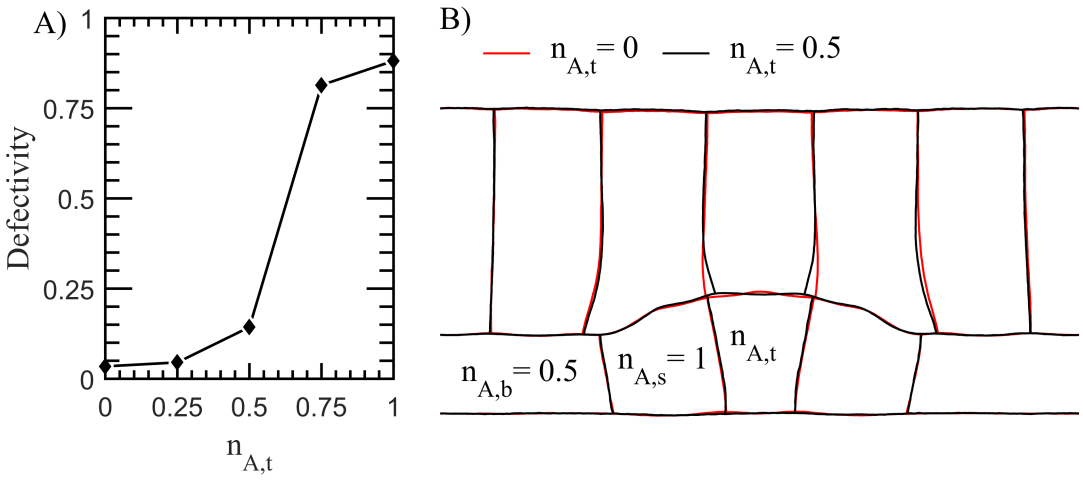

Figure 6.9: A) The defectivity of a sloped sidewall simulation versus the composition of the top of the mesa. B) The average cross-sectional shape of lamellae formed on underlayers with $n_{A,t} = 0$ (red) and $n_{A,t} = 0.5$ (black). All simulations have $W_{T,b} = 1.5\,L_0$, $W_{M,t} = 0.5\,L_0$, $\Delta H = 0.2\,L_0$, $n_{A,b} = 0.5$, $n_{A,s} = 1$

6.4 Conclusions

A coarse-grained molecular dynamics model was used to explore both the geometric aspects as well as the chemical preferences of these hybrid underlayers and the result these variables have on the defectivity of the resulting BCP film. It was found that underlayers with vertical sidewalls behave in manners similar to more purely graphoepitaxial guiding underlayers, while underlayers with sloped sidewalls behave in a manner similar to chemoepitaxial guiding underlayers.

With vertical sidewalls it is found that larger topographic step heights decrease defectivity, though with diminishing returns. The width of the trench should be an integer multiple of the natural repeat distance of the block copolymer, though the width of the trench can have approximately 10% error before significantly affecting the defectivity. It was hypothesized that the width of the guiding regions should be spread out in order to lower defectivity. Finally, the chemical preference of both the top of the mesa and bottom of the trench have little effect on the defectivity so long as the preference is neutral enough to prevent the formation of horizontal lamellae.

A variety of sloped sidewalls were explored. Sidewalls that undercut the mesa were found to increase defectivity. It was found that there are trapezoidal shaped topographies that can offer low defectivity. This was particularly true when the top of the mesa as well as the width of the sidewalls were approximately the width of one lamellae. In these cases it was found that there was an optimal height of the topography for minimizing the defectivity. The optimal height is hypothesized to be the height that makes the effective width of the sidewall the same width as a lamellae. Additionally, it was found that a slightly preferential bottom of the trench and a very preferential top of the mesa helped further lower defectivity. An additional sloped sidewall case where the topographic feature was triangular in shape was explored. It was found that this triangular topographic feature yields far lower defectivity than a similarly sized rectangular topographic feature.

CHAPTER 7
PROTRACTED COLORED NOISE DYNAMICS APPLIED TO LINEAR POLYMER SYSTEMS

7.1 Introduction

Relative to small molecules, the molecular simulations of polymers require longer simulation times due to their large molecular weight and chain entanglements. Such entanglements significantly increase the viscosity and decrease the diffusivity of the system which increases the needed simulation time. The large scale of the polymer chains also increases the required length scale of the simulations. Mesoscale models attempt to overcome these limitations via coarse-graining,[60, 61, 62] which treats multiple atoms as a single particle or element, or by using mean-field approaches to calculate forces.[63, 64] Such mesoscale models speed up simulations by reducing the computational requirements of the force calculations, and increase the integration time step required. However, additional simulation efficiency is needed to address the long relaxation times inherent in polymer simulations. This is particularly true for the simulation of evolving polymer morphologies such as those observed in block copolymers (BCPs). Annealing of defects in such morphologies is challenging because of the energetic incompatibility of the two blocks, indicated by a relatively high Flory-Huggins enthalpy of mixing parameter (χ), of the two differing blocks in the polymer. The product of this parameter and the number of monomeric units in the blocks (χN) must be sufficiently high to result in phase separation, but this increases the transition energy of the defect annealing because the blocks must diffuse through domains of each other.[50] Coarse-grained simulations of defects using relatively short BCPs at realistic χN values would require simulations on the timescale of months or years to anneal a single defect. Field models, such as Self-Consistent Field Theory (SCFT),[64] do not always ac-

curately model certain phenomena such as fluctuations,[65] or non-polymeric objects,[66, 67] and often have difficulty addressing dynamics or non-equilibrium states and properties[68]. If atomistic and/or coarse-grained simulation techniques could be extended into longer time and/or length scales, then new phenomena could be more accurately studied.

Previously, we developed a simulation method called Protracted Colored Noise Dynamics (PCND) that adds a stochastic component to the deterministic equations of molecular dynamics (MD). [69, 70, 71] It is similar to Langevin, Brownian, or dissipative particle dynamics (DPD) except that the stochastic force is applied to increase local phase space sampling rather than to simulate the surrounding viscous solvent. Efficient phase space sampling is achieved by (i) increasing the magnitude of the stochastic force, (ii) decoupling the magnitude of this force from the damping coefficient, and (iii) employing time-correlated or colored noise in the stochastic component in contrast to the white noise of these other stochastic methods. Decoupling of the damping coefficient from the magnitude of the colored noise no longer enforces temperature control, so the damping coefficient is determined by a separate integral thermostat model. This decoupling violates the fluctuation-dissipation theorem and consequently perturbs the dynamics of the system. For this reason PCND is only useful for finding important structures. Ultimately, the dynamics of these new structures will be sampled using MD. The efficiency of PCND was originally demonstrated using a Lennard-Jones (LJ) system where PCND crystallized the system over three orders of magnitude faster than MD.[70] This work adapts PCND for application to linear polymers, and evaluates the effectiveness of this application by examining the speed with which it anneals defects in self-assembled BCP lamellae.

7.2 Simulation Methods

7.2.1 Generation of colored noise

In the original demonstration,[71] PCND used stochastic noise in the form of additional force vectors on the atoms whose correlation decayed exponentially with time. The mag-

nitude of this time-correlated noise $\varepsilon(t)$, is obtained via Equation 7.1, where ξ is the root mean square magnitude of the forces, τ is the correlation time, and $\eta(t)$ is white noise (which is uncorrelated in time).

$$\frac{d\varepsilon(t)}{dt} = \frac{\xi\tau^{0.5}\eta(t) - \varepsilon(t)}{\tau}, \tag{7.1}$$

This results in the statistical properties described by Equations 7.2 and 7.3.

$$\langle\varepsilon(t)\rangle = 0, \tag{7.2}$$

$$\langle\varepsilon(t)\,\varepsilon(s)\rangle = \xi^2 \exp\left[-\frac{|t-s|}{\tau}\right], \tag{7.3}$$

The distribution of initial values, ε_0, is given by Equation 7.4.

$$P(\varepsilon_0) = \frac{1}{2\pi\xi^2} \exp\left[-\frac{\varepsilon_0^2}{2\xi^2}\right], \tag{7.4}$$

These forces were generated, both by Jenkins $et\ al.$ and in the rest of this work, using the algorithm of Fox $et\ al.$[72] The algorithm generates an initial condition ε_0 by using the Box Mueller algorithm seen in Equation 7.5.[73]

$$\varepsilon_0 = \xi\left[-2\ln(a)\right]^{0.5}\cos(2\pi b), \tag{7.5}$$

The variables a and b are uniformly distributed random numbers between 0 and 1. The noise is then integrated through time using Equations 7.6, 7.7, and 7.8.

$$E = \exp\left[-\frac{\Delta t}{\tau}\right], \tag{7.6}$$

$$h = \xi \left[-2\left(1 - E^2\right) \ln\left(a\right)\right]^{0.5} \cos\left(2\pi b\right) \,, \tag{7.7}$$

$$\varepsilon_{t+\Delta t} = E \cdot \varepsilon_t + h \,, \tag{7.8}$$

Again, a and b are uniformly distributed random numbers between 0 and 1. These uniformly distributed random numbers are generated every timestep for all bodies for which the stochastic force is being applied. For the simulations in this work, random numbers are generated using a Mersenne Twister[74] algorithm (MT19937 implementation) for each instance. The algorithm is seeded at the beginning of the simulation with the current time in seconds from midnight January 1, 1970 UTC.

In the original application of PCND to a Lennard-Jones glass, the governing equation (Equation 7.9) is very similar to the modified Langevin equation. The acceleration of the atom or coarse-grained particle ($\ddot{x}$) is determined by the gradient of the potential energy ($U\left(x\right)$), the stochastic noise term, $\varepsilon\left(t\right)$, and a damping term ($\zeta\left(t\right)\dot{x}$). The difference between Equation 7.9 and the Langevin equation is that the noise term is colored noise as opposed to white noise, and the damping coefficient ($\zeta\left(t\right)$) is determined by an integral controller. [70, 71]

$$m\ddot{x} = -\nabla U\left(x\right) + \varepsilon\left(t\right) - \zeta\left(t\right)\dot{x} \,, \tag{7.9}$$

This resulted in a reduction in the crystallization by a factor of approximately 3000 after a brief optimization of parameters.[71]

7.2.2 PCND Applied to Linear Polymer Systems

The application of PCND to a LJ glass increased the intensity and the time correlation of thermal fluctuations uniformly throughout the system. However, this will not be effective given the anisotropic diffusion modes of large polymer chains. The dominant diffusion mode for the large polymer chains is the reptation mode suggested by de Genne in which

the polymer chain slithers along its contour amidst entanglements with other chains.[75, 76] Phase separated block polymers similarly require concerted motion along the backbone because chains are stretched perpendicular to an interface and must move across that interface.[77, 78] To enhance reptation and sampling over such energy barriers we apply the PCND stochastic force along the polymer contour. Using homogeneous fluctuations would be inefficient in the case of entangled polymers because such entanglements would block diffusion in that direction, and in phase separated polymers because it would result in diffusion along an interface.

The magnitude and one dimensional direction of the stochastic force $\varepsilon(t)$ is calculated via Equations 7.4 through 7.8 and then applied along the direction of the backbone of the chain. This direction was calculated by taking the vector between two adjacent beads in the polymer backbone. Every interior bead in a single chain experiences a force of equal magnitude, but the direction of this force applied to the bead is along a vector that connects these two adjacent beads as seen in Figure 7.1. The change in the sign of this stochastic force, as seen in Figure 7.2, corresponds to a change in direction of the force along the backbone. In this work, the end bead does not experience any stochastic force due to PCND. A force that is applied randomly, or along the direction of the last bond would also be possible. This specific application of these forces is visualized in Figure 7.1.

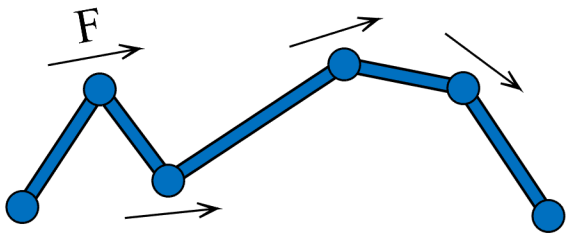

Figure 7.1: Visualization of how stochastic forces are applied in polymer PCND. The forces are applied along the backbone of the chain, that is, the force on an interior bead is applied along the vector between the two adjacent beads. The magnitude of the force is the same for every bead on the chain and can change sign with time.

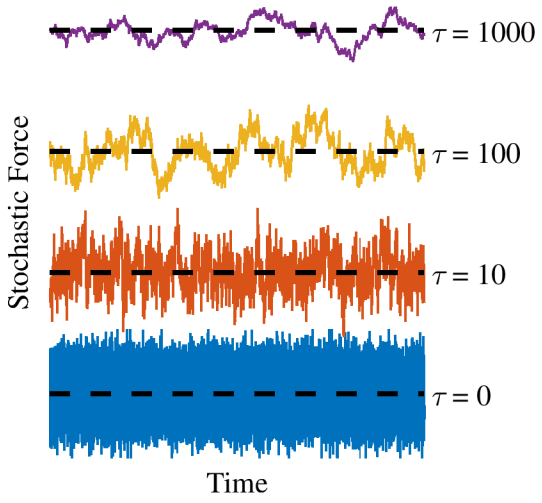

Figure 7.2: Representative plot of the magnitude of the force over time for a single chain at various values of τ. The dashed black line indicates where the force is zero for each series. As τ increases, the force magnitude is correlated over longer times. The various τ series are offset for clarity.

As in the LJ glass case, the timescale over which the force changes values is determined by the parameter τ, or the correlation time. The root mean square of the force is determined by the parameter ξ. The effect of τ on the stochastic force is visualized in Figure 7.2 where the magnitude of an example stochastic force for a single chain is calculated through time for various τ values. The series are offset for clarity. When τ is zero, the noise is completely random, and as τ increases, the correlation time of the force increases, that is, the force changes directions more gradually. It should be noted that in all four cases shown here the root mean square of the force was $\xi = 0.1$, despite visually looking otherwise. The reason for this is that extreme values are emphasized graphically in the low correlation samples because of the abundance of data points.

7.2.3 Coarse-grained Molecular Dynamics Model

All simulations here are bulk (Section 2.2.1) NVT simulations (Section 2.3.2), run using the built in HOOMD-Blue Nosé-Hoover temperature controller with a temperature controller

time constant of $\tau = 0.2$ timesteps and typically with a set point of $T = 500$ K though some simulations were at the elevated temperatures when indicated. This temperature is typical of the thermal annealing temperature used for BCPs in microelectronics processing.

7.2.4 Implementation of PCND in HOOMD

The stochastic force algorithm was programmed into HOOMD-blue[34, 35] by modifying the existing code. PCND was introduced as an additional angle term, which applied a force to the center bead of an angle based on the direction of the vector between its two adjacent beads. The force is propagated through time using Equations 7.5-7.8. When no time correlation was used, very large forces occurred in small numbers that resulted in significant errors within the simulation. In order to remove these errors, a cutoff was used. If the change in the force was greater than $(-2 \ln 0.001)^{0.5}$, then the change in the force was set to $(-2 \ln 0.001)^{0.5}$.This occurs at a frequency of less than 1×10^{-4} in cases with no time correlation, and with frequency less than 1×10^{-11} (no occurrence was found for multiple calculations that sampled 1×10^{11} time steps) in all correlated cases, indicating that this case does not occur in any of the simulations shown here.

The efficiency of this implementation was also computed by running a simulation of 57,888 beads in 3,618 chains of 16 beads per chain for 1,000,000 timesteps. The fraction of time spent calculating each step is shown in Figure 7.3. The PCND calculation is about 4% of the overall calculation time, indicating a relatively efficient process. The other columns in Figure 7.3 refer to the bond force and energy calculation, the angle force and energy calculation, the integration, the Lennard Jones neighbor list calculation, the Lennard Jones force and energy calculation, and the overhead of memory transfers and other process required by HOOMD's algorithms. Greater optimization is possible, as this modification did not fully utilize all of HOOMD's built-in optimizations, nor was an optimization of the interface between HOOMD's built in code and the added PCND code performed.

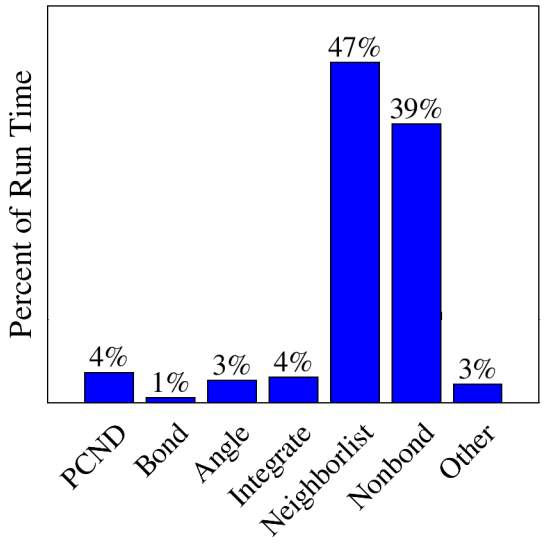

Figure 7.3: Time spent for various calculations during MD simulation in HOOMD. PCND accounts for approximately 4% of the overall calculation time.

7.2.5 System and Metrics for Testing PCND

BCP domain size

The domain size of BCP simulations was measured by first calculating the radial pair distribution function for AA pairs, $g_{AA}(r)$. Next, the structure factor $S(q)$ was calculated with a Lorch window function as calculated using Equation 7.10.[79, 80] The location of the peak gives the plane to plane repeat distance of the polymer. For a lamellar morphology, the plane to plane repeat distance is equivalent to the domain size or repeat distance of the BCP. The structure factor is essentially equivalent to the result of a scattering experiment, which are often used to measure the ODT or domain size in experimental systems.[81, 7, 82, 83]

$$S(q) - 1 = 4\pi\rho_0 \int_0^R \frac{\sin qr}{qr} \left[g(r) - 1\right] \frac{\sin \pi \frac{r}{R}}{\pi \frac{r}{R}} dr \,, \tag{7.10}$$

Homopolymer

Bulk homopolymer using the A bead described above was simulated in order to measure the rate of diffusion under various PCND conditions as well as the measure the chain statistics. Simulations were run 50 ns recording the state every 1 ns. Analysis was made over the last 40 ns after all measured properties appear to cease changing. Diffusion was measured by measuring the mean squared displacement (MSD) of the center of mass of chains, then calculating the slope of the MSD. The radial pair distribution was calculated for each recorded state and then averaged over time.

BCP Defect Annihilation Kinetics

To determine the kinetic rate of defect annihilation in BCP simulations, defects were intentionally built into initial simulations and then allowed to heal, as done previously.[50] Simulation volumes were five times the natural lamellar repeat distance of the BCP in the x dimension, three times the natural repeat distance of the BCP in the y dimension, and equal to the natural repeat distance of the BCP in the z dimension. They were initialized with chains randomly placed in the simulation volume as described in section 7.2.3. After initial minimization, an external potential was applied to produce a defect (see Peters $et\ al.$[50] for details of external potential). Once the defect formed, the external potential was turned off and the simulation continued, allowing defect annihilation. Twenty replicates were run at various values of χN, ξ, and τ. Simulations were run until the defect annealed out or until the simulation reached 500 ns, whichever came first. The defect heal rate was calculated using Equation 7.11.

$$R_{tot} = \frac{F_H}{t_{ave}}\,, \tag{7.11}$$

R_{tot} is a measure of the total rate of defect healing, F_H is the fraction of defects healed in the maximum simulation time and t_{ave} is the mean time to heal the defect in the simulations that did heal within the maximum simulation time of 500 ns. In general, F_H is one because

all of the defects annealed within the simulation time, so R_{tot} is simply the average rate for these simulations to anneal. In the case of the elevated temperature simulation no simulation healed in the 500 ns.

7.3 Applications of PCND for polymer systems

7.3.1 Homopolymer Diffusion

The effect of PCND on the diffusion of bulk homopolymers is shown in Figure 7.4. The diffusion rate was measured for homopolymers of length $N = 64$ for various τ and ξ. Increasing either τ or ξ increases the diffusion rate. In Figure 7.4A the increase in diffusion with respect to τ roughly follows a power law, and in Figure 7.4B the increase in diffusion with respect to ξ roughly follows a power law. Increases in ξ yield large increases in diffusion, while increases in τ initially increase diffusion but have diminishing returns. While PCND does increase diffusivity, very large parameters would be required to increase diffusivity by a full order of magnitude. The increase in diffusion is of a similar order to the increase in diffusion that can be found by increasing the temperature of the system, as indicated by the red line in Figure 7.4. However, PCND and elevating the temperature increase diffusion in slightly different ways. An increase in thermal energy increases the translational motion of all beads in the system slightly randomly. On the other hand, introducing PCND coordinates the movement of chains which will preferentially encourage the reptation mode of movement.

7.3.2 Homopolymer Chain Statistics

Various chain statistics were measured for bulk homopolymer and are shown in Figure 7.5. Simulations were run under standard conditions (black line) and compared to elevated temperature simulations (red line) and simulations with PCND (green and cyan lines). Neither set of PCND parameters shown here has much effect on bond length distribution, the bond angle distribution, or the radial pair distribution function of the beads. On the other hand,

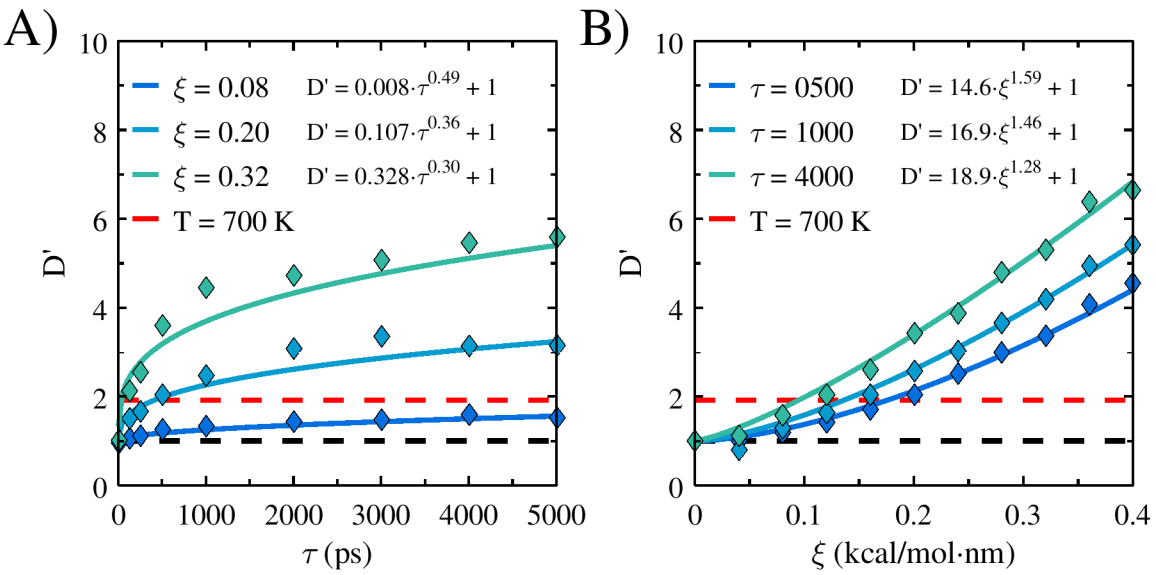

Figure 7.4: Plot of the relative diffusion constant of bulk homopolymer with $N = 64$ A) as a function of τ for various ξ and B) as a function of ξ for various τ. The relative diffusion constant shown, D', is the measured diffusion constant of the simulation divided by the diffusion constant of the same homopolymer run without PCND under typical conditions ($T = 500$ K), which is 3.7×10^4 cm^2/s. The actual data is shown by the diamonds and a power-law fit to this data is shown by the solid line. The equations associated with these fits appear in the figure. Additionally, the relative diffusion constant without PCND at an elevated temperature ($T = 700$ K) is shown by the red dashed line.

increasing the temperature naturally has a large effect on all of these distributions. The more extreme PCND parameters ($\xi = 0.4$ kcal/(mol·nm) and $\tau = 5000$ ps) does appear to shift the radius of gyration of the chains slightly lower. However, these parameters are higher than any useful set of parameters as will be shown later. When stochastic fluctuations reach a certain level they dominate the conserved force between the atoms or beads and produce an unrealistic trajectory. For reasonable parameter values though, (what is reasonable will be discussed in more detail later) PCND does not alter the shape of chains or packing of beads in the system.

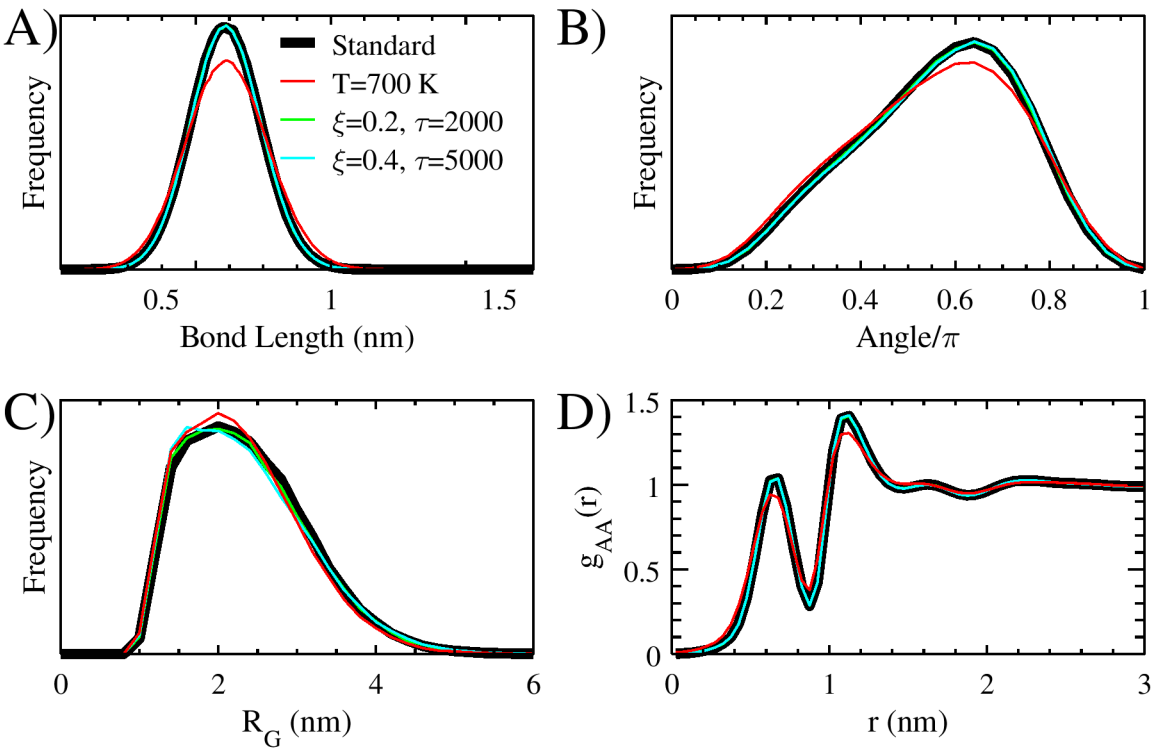

Figure 7.5: Plots of A) the bond length distribution, B) the bond-angle distribution, C) the radius of gyration distribution, and D) the radial pair distribution for bulk homopolymers under standard conditions (black), elevated temperature conditions (red), with moderate PCND parameters of $\xi = 0.2$ kcal/(mol·nm) and $\tau = 2000$ ps (green), and with more extreme PCND parameters of $\xi = 0.4$ kcal/(mol·nm) and $\tau = 5000$ ps (cyan).

7.3.3 Block Copolymer Defect Annihilation

In many block copolymer simulations, the block copolymer can become kinetically trapped in a defective state. An example of such a defect is a dislocation pair defect which can be seen in Figure 7.6. Previous studies have been done to measure the kinetic rate of defect annihilation of these dislocation pairs.[50, 84, 51, 85, 86] The data for the defect annihilation rate for a BCP of length $N = 64$ at various χN values without PCND (using the simulations from Peters *et al.*[50]) is shown by the black data points in Figure 7.7A. While the rate of defect annihilation remains relatively constant at low χN, suggesting a barrier free transition at low χN,[50, 84] the rate drastically drops after a χN of ~30. If the rates are extrapolated to $\chi N = 55$, a simulation would need to run for about a year on

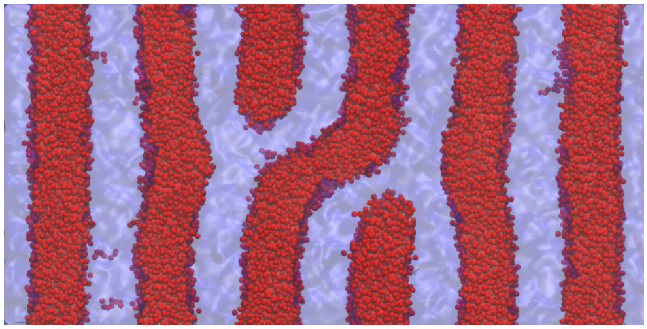

Figure 7.6: A dislocation pair defect is shown as an example of a kinetically trapped defect that can occur in a BCP simulation. Red beads represent type A, while the blue matrix represents type B. Images are rendered using VMD.[26, 27]

the hardware used here to observe defect annihilation.

PCND was applied to this system as well with various values of ξ and τ, yielding significantly higher kinetic rates for all parameter sets tested. In the best case the rate increased more than 10,000 times over the extrapolated rate without PCND and were equivalent to the apparently barrier free regime at low χN. More moderate values did not reach the barrier free transition, but did heal over 2,000 times faster than the extrapolated rate without PCND. Intuitively, applying a strong force would result in more quickly passing over energy barriers, and that is what is found. It was not possible to increase the defect heal rate beyond that of the barrier free transition rate at low χN without altering the domain size of the BCP, as will be discussed later.

Figure 7.7B plots defect annihilation rates as a function of τ for various ξ. There appears to be a peak in the rate as a function of τ that shifts to lower τ for high ξ. Increasing τ allows the system to sample over energy barriers better and therefore increase defect heal rate, but when τ is too large, it causes less efficient sampling. There appear to be two causes for this. First, large τ values may allow the sampling over barriers that are ultimately not conducive to defect annihilation. For example, the pathway to defect formation or growth has a larger energy barrier than the pathway to defect annihilation since the free energy of the simulation without a defect is lower than that of the simulation with a defect,[25,

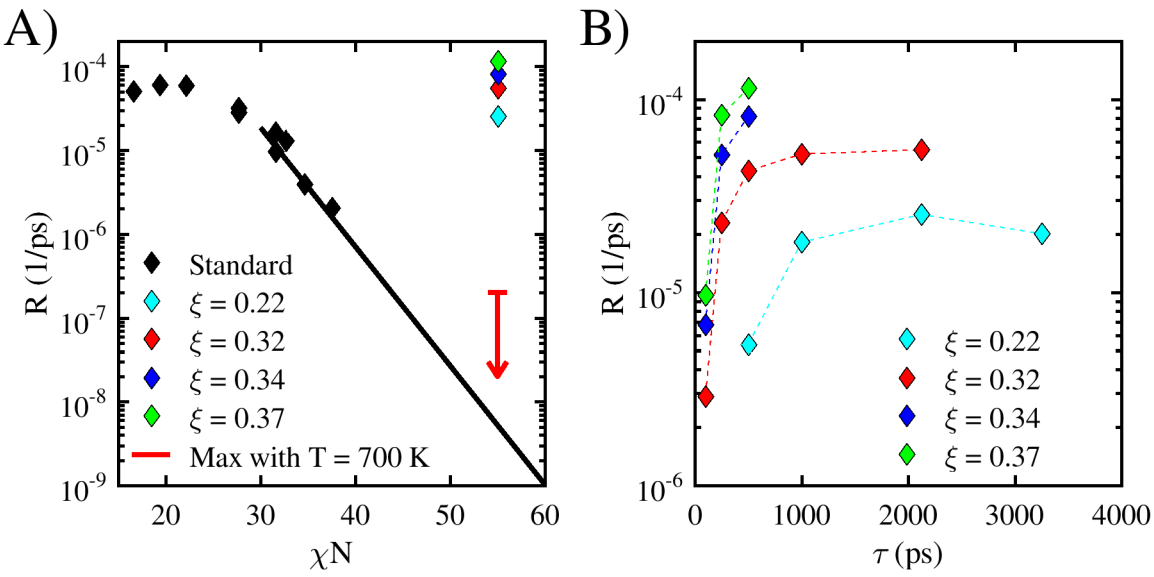

Figure 7.7: Plots of rate of defect healing as a function of χN and PCND parameters for $N = 64$. A) shows defect heal rates as a function of χN without PCND alongside rates using PCND at various ξ values their optimal τ values and maximum rates at elevated temperatures. B) shows the defect heal rates as a function of τ and ξ. The 95% confidence interval for the PCND points are smaller than the markers.

84] but the simulations with higher ξ and τ values were seen to occasionally form larger defects before annihilating them, or to form new defects after removing defects within the simulation time. Additionally, the random noise, when applied in a certain direction, may be probing a pathway that is not useful for defect removal. When τ is very large, then this pathway will continue to be probed for long times, ultimately wasting simulation time. The fact that this peak shifts to lower τ as ξ increases makes sense, as the time required for a certain pathway to be properly probed is decreased due to the increased force applied, and the time required to sample over pathways that form defects rather than remove them is also decreased. This results in the observed lower optimal τ value.

For comparison, the same simulations were run at elevated temperatures in order to increase defect heal rate. While typical simulations in this paper are run at 500 K, these high temperature simulations were run at 700 K. However, none of the elevated temperature simulations annealed out in the time given (500 ns). The ”fastest case” kinetic rate, that is

the rate assuming all simulations would anneal out immediately after the simulations were halted, is marked on Figure 7.7A by the base of the red arrow, which corresponds to the inverse of the 500 ns maximum simulation time. Since the rate is certainly much lower than this fastest case scenario, a red downward arrow is drawn to indicate the lower rate. This result shows that introducing energy into the system by PCND is far more efficient at sampling over large energy barriers than simply increasing the overall kinetic energy. This makes sense as the PCND random forces are correlated in such a way as to specifically encourage chain movement, whereas an overall increase in kinetic energy via a temperature increase is not. Increasing the temperature also adds energy into many unhelpful modes, such as into bond vibrations, which do not significantly participate in the defect annihilation process. While this increased temperature also increases some helpful motion, such as diffusion, the motion of each bead in the chain is uncorrelated and so is less efficient at sampling phase space. In contrast to increased temperature, PCND adds a correlated force to the beads of a chain, increasing the ability of a chain to move. Additionally, since these are phase separated lamellar block copolymers, each chain is, on average, stretched in a direction normal to the microphase interface. This means the PCND force, which acts in the direction of the backbone, will be normal to the interface, and motion in this direction will promote the formation of bridges between domains, a necessary step in the annihilation of defects and a step with a very large energy barrier.

7.3.4 Effect of PCND on Domain Size and the Free Energy Landscape

The significant increase in defect annihilation rate is very encouraging, but this technique is only useful if the overall energy landscape is not significantly perturbed. For this reason, a typical PCND simulation would consist of a PCND active stage which is used to induce large morphology changes that are otherwise inaccessible by MD, followed by a PCND inactive stage which is used to perform more precise calculations. During the PCND active stage, the locations and relative values of the minima of the system must remain roughly

constant. Ideally, a direct free energy calculation of the entire landscape surrounding the defect and defect free states would be performed to show that the landscape is not altered, but such a calculation is very time consuming and difficult given our model. Instead, lamellar repeat distance is used as a proxy for a portion of the free energy landscape. If PCND does not alter the repeat distance of the lamellae, then it is unlikely to significantly alter the locations of minima and maxima.

The lamellar repeat distance (L_0) as a function of τ for various ξ is shown in Figure 7.8. The parameters shown here include those shown in Figure 7.7 that gave optimal increases in defect annihilation rate. Most of these parameters show no measurable effect on L_0, though the highest show a slight decrease. The effect of increasing temperature to 700 K is included as well and clearly has a much greater impact on L_0 than even the largest effective PCND parameters. This indicates that PCND, when using well-chosen parameters, has little effect on the final equilibrium structure, an important feature in regards to the usefulness of this technique. It should also be pointed out in cases where PCND does have a slight effect on L_0, turning off PCND quickly returns (less than 8 ns for all simulations shown here to return to within 0.01 nm of the natural pitch without PCND) to the unaffected repeat distance.

7.3.5 Limits of PCND Parameters

Only moderate PCND parameters were used in the previous sections to highlight the advantages of PCND; however, very large parameters can have negative effects on the simulation and it's accuracy. This can be illustrated by Figure 7.9, which shows a lamellar forming BCP with steadily increasing τ values. Initially, with no PCND (Figure 7.9A), the system has well formed lamellae and a small interfacial width. For small parameters (Figure 7.9B), the fluctuations at the interface have increased slightly, but the overall structure remains intact. At larger values (Figure 7.9C), the fluctuations have significantly increased, but the lamellae still remain intact. Finally, at even larger values (Figure 7.9D) the fluctuations

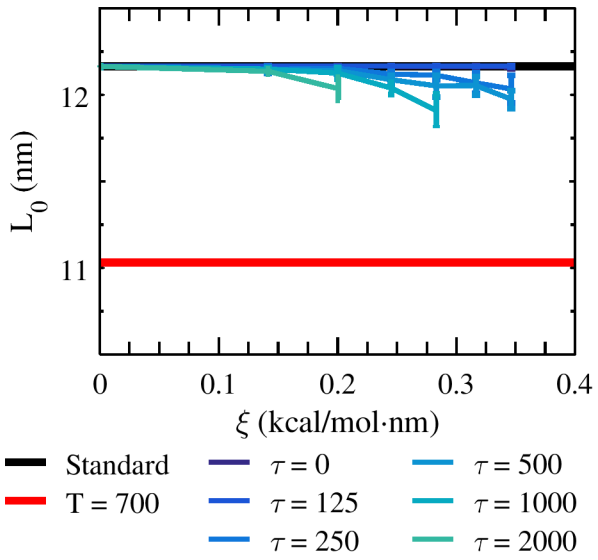

Figure 7.8: Plot of pitch of a BCP as a function of ξ and τ for $N = 64$. PCND slightly lowers the pitch of the BCP, while elevating the temperature significantly lowers the pitch.

have begun to dominate the structure. There are still local regions of lamellae present, but the simulation is dominated by fluctuations and chains rapidly cross domains.

This state is easily identifiable as can be seen in Figure 7.10 where the red line delineates the approximate transition to this fluctuation dominated state. Lamellae are clearly seen at values to the left and below the red line, but cannot be identified to the right and above the red line. For parameters near this transition, it can be seen that lamellae are still present, though the interfaces are far rougher (indicated by the gray coloring or the waviness of the lines).

The transition to the highly fluctuating state as a function of ξ and τ was found for BCPs at different degrees of polymerization. These results are found in Figure 7.11A. Parameter sets to the upper right of the lines shown are dominated by fluctuations, while sets to the lower left remain in a well ordered lamellar state. As the strength of PCND (ξ) increases, the force does not need to be correlated as long (τ) in order to enter the highly fluctuating state. Similarly, if the force is highly correlated (large τ), the force does not need to be as strong in order to enter the highly fluctuating state. This leads to the

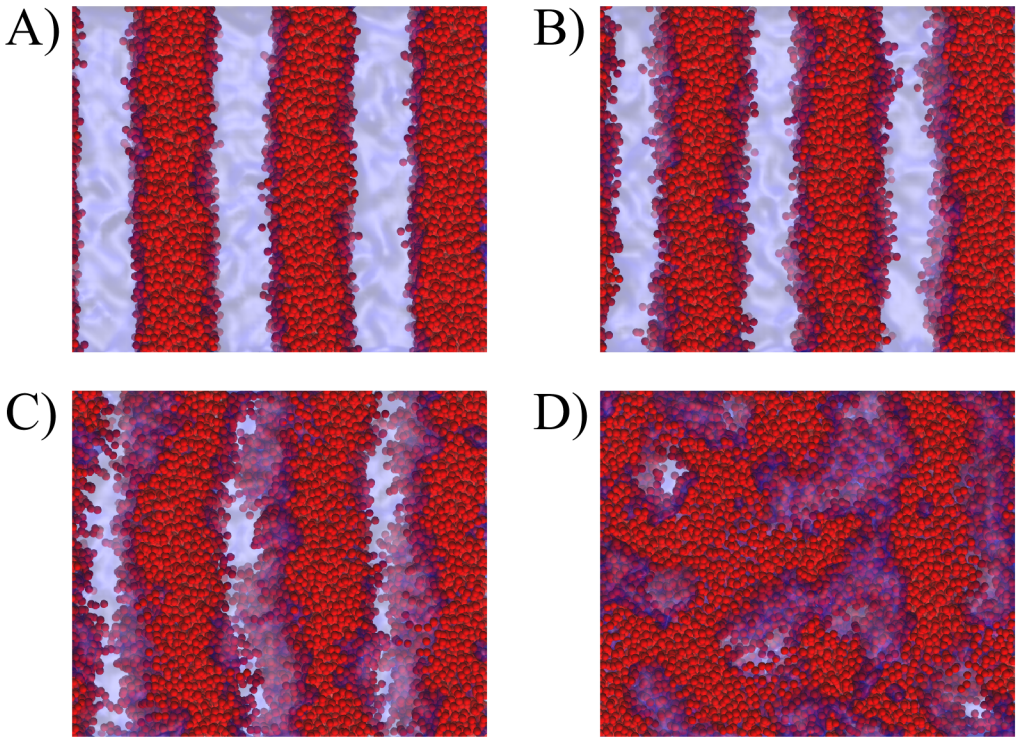

Figure 7.9: Images of the block copolymer simulations with A) no PCND, B) $\xi = 0.32, \tau = 250$, and C) $\xi = 0.32, \tau = 1000$, and D) $\xi = 0.32, \tau = 5000$. Images are rendered using VMD.[26, 27]

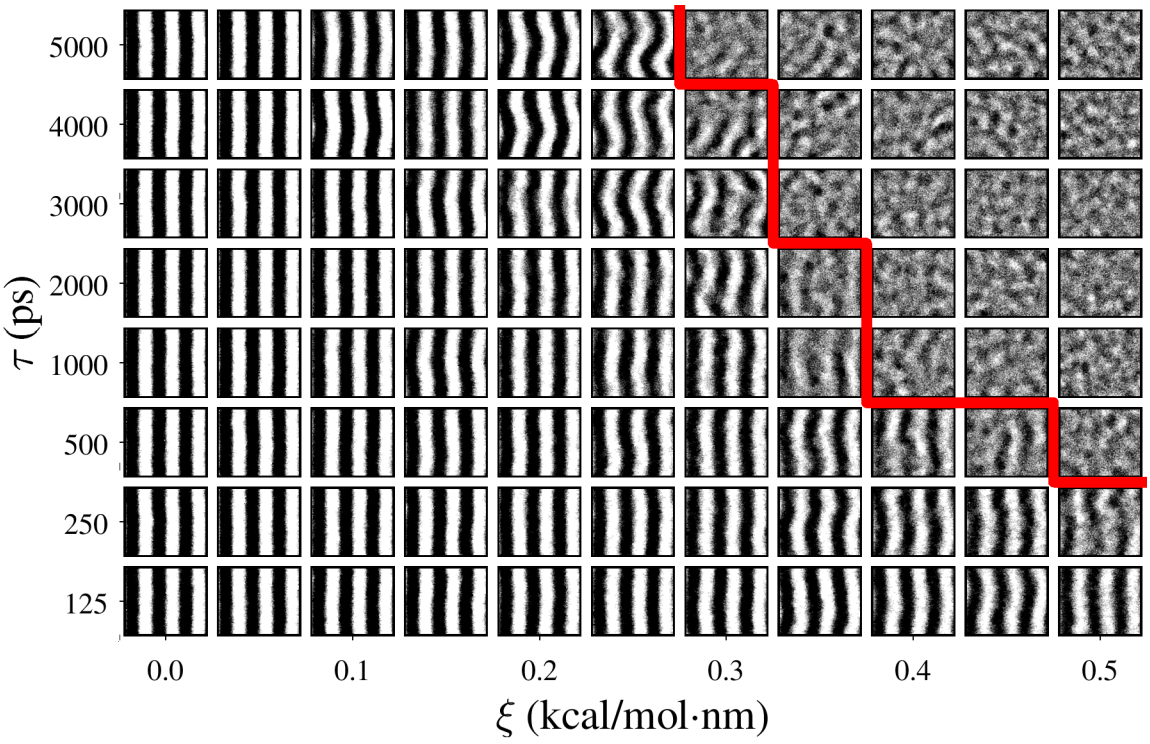

Figure 7.10: Plot of simulation results with varying ξ and τ. A red line is drawn roughly to indicate approximately the transition to the highly fluctuating state. Images are rendered using MATLAB.[36]

result that the transition curves in Figure 7.11 are dependent on both τ and ξ. Increasing the degree of polymerization of the BCP increases the total force on the chain for the same ξ because each bead receives the same force. Additionally, since these are phase separated BCP, the chains are going to be extended, meaning the PCND force will largely be applied in the same direction, increasing the net force applied. This is likely part of why a smaller chain requires a greater ξ to enter reach the transition. However, there are likely other important factors, such as L_0, which also increases with N. A BCP with a larger L_0 would likely require stronger PCND to enter the highly fluctuating state since chains would need to be dragged across a greater distance to jump from one domain to another. More work is required to fully understand the dependence of this transition on factors such a the degree of polymerization, the Flory Huggins χ parameter, and the volume fraction of the BCP. However it is worth noting that when the mean square force is multiplied by the number of forces per chain a single transition curve is created, as plotted in Figure 7.11B. This indicates that the total mean square stochastic force may be a universal scaling parameter to determine the useful parameter space of PCND. If this can be understood, then the optimization of PCND parameters can be significantly streamlined, resulting in a technique more easily applied to a variety of systems.

7.4 Conclusions

An algorithm to apply Protracted Colored Noise Dynamics (PCND) to polymeric systems was developed. PCND increases the fluctuations in the system, specifically targeting the reptation mode of the polymer by applying a time correlated force to every bead in a coarse-grained polymer chain in the direction of the backbone. While only linear coarse-grained polymer chains were explored here, similar methods can be used to apply PCND to atomistic models or polymers with side chains. In homopolymer simulations PCND was shown to greatly increase the rate of diffusion while not significantly altering chain conformation or crystal packing structure. In block copolymer simulations, PCND was shown to

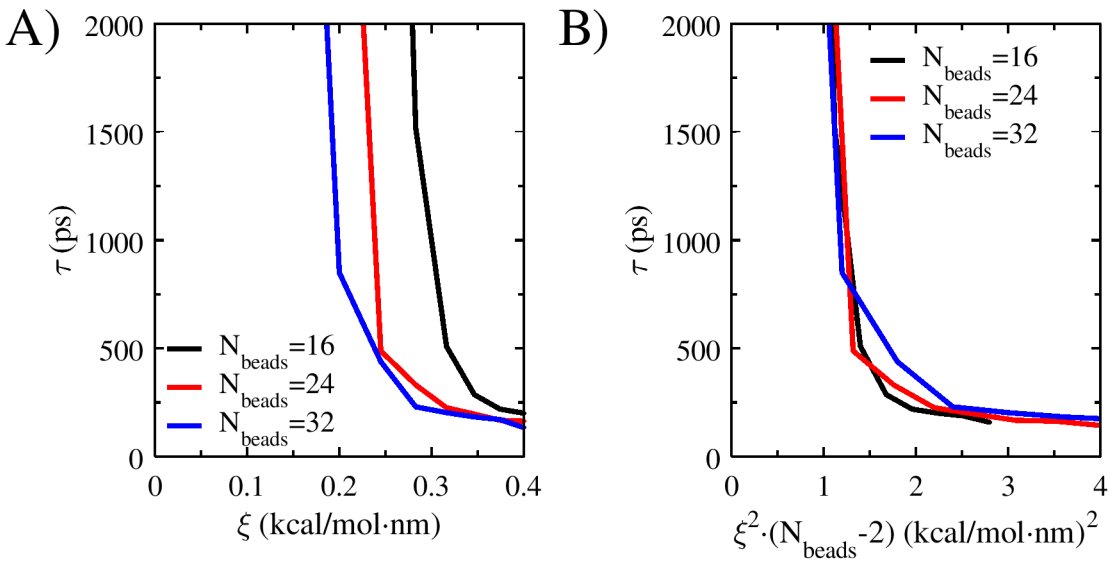

Figure 7.11: The transition to the highly fluctuating state as a function of τ and ξ for both $N_{beads} = 16$, $N_{beads} = 24$, and $N_{beads} = 32$ BCPs. For parameters above and to the right of the line the BCP simulation mixes, while for parameters below and to the left the BCP simulation formed well ordered lamellae.

drastically increase the kinetics of defect annihilation. The pitch of the BCPs was not significantly affected by PCND when using optimal parameters, suggesting PCND is not drastically altering the free energy. The limits of PCND when applied to BCP systems was explored, as it was found too strong of PCND could force the BCP to enter a highly fluctuating state. PCND is a simple simulation tool that can be used quickly to probe across energetic barriers in simulations for minimal computational cost.

CHAPTER 8
CONCLUSIONS AND RECOMMENDATIONS

8.1 Conclusions

Block copolymer directed self-assembly is currently being explored as a potential method for producing smaller features in the integrated circuit fabrication industry. However, while the defectivity of current BCP-DSA systems is low and difficult to characterize experimentally, it is still too high to satisfy the requirements of the integrated circuit fabrication industry. This work uses a coarse-grained molecular dynamics model to look at how the design of guiding underlayers can be altered to minimize the defectivity that BCP DSA produces. Additionally, other factors related to the resulting lamellae quality are considered. Finally, a new simulation technique for better probing equilibrium states of large scale polymeric molecular dynamics simulations is introduced.

In Chapter 3 the effect that the geometry and energetics of a simple chemoepitaxial guiding underlayer have on the defectivity of multiple sample BCPs are considered. Defectivity is found to be minimized when the contrast between the pinning stripe and the background region is as high as it can be without transitioning the film into the mixed lamellae morphology. Altering the BCP in such a way that the mixed lamellae morphology is less stable (such as by altering the volume fraction) can help lower defectivity. A density asymmetric BCP was simulated and it was found that the optimal volume fraction of this BCP for minimizing the defectivity was shifted away from $\phi_A = 0.5$ (the ideal for a density symmetric BCP), likely due to the asymmetry in the compressibilities of the blocks. A frustrated film thickness is found to give a larger window for forming well-aligned vertical lamellae for symmetric BCPs and density asymmetric BCPs. When there is a cohesive energy density (CED) asymmetry in the BCP, film thickness has a large effect on the opti-

mal background region composition for forming well-aligned vertical lamellae due to the preferential wetting of the free interface by the lower CED block.

In Chapter 4 the free energy for defects of various sizes were measured on various underlayers. It was found that the free energy was generally highest when a pinning stripe was located under the interior adjacent lamellae to the terminating block of a dislocation, suggesting low probability of this occuring at equilibrium. It was found that pinning stripes located approximately 1 L_0 outside of the terminating blocks of the defect have little effect on the free energy of the defect. If the defect is large enough, there exists a location in the center of the defect where pinning stripes have less of a free energy penalty than underneath the terminating block, suggesting defects can be stable while straddling a pinning stripe. For all the different sized defects explored the thermodynamic driving force for the removal of the defects was approximately the same on an 8x density multiplying underlayer as it was on an unpatterned underlayers since the defect is able to fit fully in an area without a pinning stripe nearby. While increasing density multiplication does theoretically increase the number of defects present due to a decreased free energy difference, the free energy difference is still incredibly high even on an unpatterned underlayer, making their estimated population at equilibrium very small. This bolsters the idea that the high defect densities reported experimentally are due to kinetic entrapment. Increasing the defect order reveals a maximum in the free energy of the defects around defect order 3 or 4. It is hypothesized that free energy versus defect order is controlled by two competing factors: the increase in interfacial area for larger defects increases free energy while the greater separation of the dislocation pairs decreases free energy by spreading out the strain of the dislocation across a greater area. This leads to free energy initially increasing with increasing defect size, but later decreasing as the defect continues to grow.

In Chapter 5 simulations were run to analyze the quality of lines formed on flat chemo-epitaxial guiding underlayers with varying composition of the background region and width of the pinning stripe. It was found that underlayer properties had little effect on LWR,

which was more dependent on the BCP itself. Increasing the guidance of the system (wider pinning stripes, more preferential background regions) decreases the LER of the resulting lamellae. However, this increase in guidance increased the variation of lamellae width through the depth of the film. This suggests the optimal conditions for LER and line quality are in conflict, so some compromise will have to be made depending on the requirements of the process when choosing processing conditions.

In Chapter 6 both the geometric aspects as well as the chemical preferences of hybrid chemoepitaxial and graphoepitaxial guiding underlayers were explored with respect to their effect on the resulting defectivity of the BCP film. Hybrid underlayers with vertical sidewalls were found to behave in manners similar to purely graphoepitaxial guiding underlayers. Increasing topographic step heights decreased defectivity, though with diminishing returns. The width of the trench needs to be within approximately 10% of an integer multiple of the natural BCP repeat distance. A hypothesis was developed as to what the optimal integer multiple to target was. The chemical preference of both the top of the mesa and bottom of the trench had little effect on the defectivity as long as the preference is neutral enough to prevent the formation of horizontal lamellae.

Hybrid underlayers with sloped sidewalls were found to behave more similar to chemoepitaxial guiding underlayers. This was particularly true when the top of the mesa as well as the width of the sidewalls were approximately the width of one lamellae. In these cases it was found that there was an optimal height of the topography for minimizing the defectivity. The optimal height is hypothesized to be the height that makes the effective width of the sidewall the same width as a lamellae. Additionally, it was found that a slightly preferential bottom of the trench and a very preferential top of the mesa helped further lower defectivity. An additional sloped sidewall case where the topographic feature was triangular in shape was explored. It was found that this triangular topographic feature yields far lower defectivity than a similarly sized rectangular topographic feature.

Finally, in Chapter 7 an algorithm to apply Protracted Colored Noise Dynamics (PCND)

to polymeric systems was developed. PCND increases the fluctuations in the system, specifically targeting the reptation mode of the polymer by applying a time correlated force to every bead in a coarse-grained polymer chain in the direction of the backbone. While only linear coarse-grained polymer chains were explored here, similar methods can be used to apply PCND to atomistic models or polymers with side chains. In homopolymer simulations PCND was shown to greatly increase the rate of diffusion while not significantly altering chain conformation or crystal packing structure. In block copolymer simulations, PCND was shown to drastically increase the kinetics of defect annihilation (two to three orders of magnitude). The pitch of the BCPs was not significantly affected by PCND when using optimal parameters, suggesting PCND is not drastically altering the free energy. The limits of PCND when applied to BCP systems was explored; when the magnitude and time correlation of the PCND force were to high the BCP entered a highly fluctuating state. PCND is a simple simulation tool that can be used to quickly probe across energetic barriers in simulations for minimal computational cost.

8.2 Recommendations for Future Work

The work in Chapters 4, 5, and 6 all rely on a simplified BCP where both blocks have the same density and cohesive energy density. While this is important, it there is a need to build off these works by adding more realistic BCPs that have more differences between the two blocks, as was done in Chapter 3. However, even the BCPs in Chapter 3 are not fully realistic. It would be of great value to parameterize real BCPs into the coarse-grained molecular dynamics model. Work could be done to expand Chapter 3 by having BCPs with both a density mismatch and a cohesive energy density mismatch. Additionally, BCPs with more extreme cohesive energy density mismatches could be explored, though this may require the addition of a topcoat. This model could be used to thoroughly explore the addition of topcoats to the BCP and the potential designs for said topcoats. Additionally, it would be valuable to introduce a molar mass dispersity into the two blocks of the BCP

for Chapters 3-6. A molar mass dispersity has been shown to alter the BCP phase diagram, therefore it is likely it will have an effect on DSA.

In Chapters 3-6 fairly small periodic boxes full of straight lamellae were simulated. However, in a real device more complex features will need to be considered. One example of a feature could be a bend. Another possible feature may include the interface between a region of vertical lamellae and a region of horizontal lamellae. An additional complexity will arise when attempting to use density multiplication so that the lithographic guiding pattern is less dense than the resulting BCP features.

Another extension of the work here would be including pattern defects. All guiding underlayers in this work were assumed to be perfect, while in real systems some defects may be present. These defects may be due to a particle landing on a substrate that is being prepared, or it may be due to a material defect in the resist. Either way, the way the BCP reacts to these pattern defects is of great interest.

While elements of the work done in this thesis have been produced experimentally, it would be of value to experimentally reproduce some of the other results. In Chapter 3 the behavior of a density asymmetric BCP on chemoepitaxial guiding underlayers, which would be of interest to experimentally confirm. In Chapter 5 the shape of the lamellae through the film was considered. There have been some attempts to do this experimentally, though only for 1x density multiplying underlayers.[52, 53] It would be of value to look into this on higher density multiplications, though it is experimentally difficult.

All simulations in this work used thermal annealing for the BCP. Thermal annealing is the process of elevating the temperature of the BCP above its glass transition temperature, allowing for increased mobility of the chains. There is a second method for annealing BCPs called solvent annealing. Here, a solvent is added to the BCP which swells the BCP and effectively lowers the glass transition temperature, allowing annealing at lower temperatures. Solvent annealing could be explored using the coarse-grained molecular dynamics model if a solvent could be parameterized to include.

In Chapter 7 a new method for crossing energetic barriers in polymeric molecular dynamics simulations was introduced. There are many unanswered question with regards to this method. Much work was done exploring the effect the two primary PCND parameters had, though more can be done. It would be valuable to further explore how to predict what PCND parameters are appropriate to use without needing to test the parameters for every unique system. Furthermore, it would be of value to test PCND with other systems such as atomistically detailed polymeric molecular dynamics or even simulations involving protein folding.

Finally, BCPs have many applications in fields other than the integrated circuit manufacturing industry. This coarse-grained molecular dynamics model can be used to solve problems in these fields. This includes any field that could benefit from the complex geometries, small feature sizes, and two component nature that BCPs offer, such as the fields of catalysis, filtration, adsorption surfaces, or energy storage.

REFERENCES

[1] M. A. Morris, "Directed self-assembly of block copolymers for nanocircuitry fabrication," *Microelectron. Eng.*, vol. 132, pp. 207–217, 2015.

[2] P. A. Gargini, "How to successfully overcome inflection points, or long live moore's law," *Computing in Science Engineering*, vol. 19, no. 2, pp. 51–62, 2017.

[3] A. Erdmann, T. Fhner, P. Evanschitzky, V. Agudelo, C. Freund, P. Michalak, and D. Xu, "Optical and euv projection lithography: A computational view," *Microelectronic Engineering*, vol. 132, pp. 21 –34, 2015.

[4] K. Lucas, C. Cork, A. Miloslavsky, G. Luk-Pat, L. Barnes, J. Hapli, J. Lewellen, G. Rollins, V. Wiaux, and S. Verhaegen, "Interactions of double patterning technology with wafer processing, opc and design flows," *Proc. SPIE*, vol. 6924, p. 692 403, 2008.

[5] B. Wu and A. Kumar, "Extreme ultraviolet lithography and three dimensional integrated circuita review," *Applied Physics Reviews*, vol. 1, no. 1, p. 011 104, 2014.

[6] L. Leibler, "Theory of microphase separation in block copolymers," *Macromolecules*, vol. 13, pp. 1602–1617, 1980.

[7] F. S. Bates and G. H. Fredrickson, "Block copolymer thermodynamics: Theory and experiment," *Annu. Rev. Phys. Chem.*, vol. 41, pp. 525–557, 1990.

[8] G. H. Fredrickson and E. Helfand, "Fluctuation effects in the theory of microphase separation in block copolymers," *J. Chem. Phys.*, vol. 87, p. 697, 1987.

[9] S. Lee, M. J. Bluemle, and F. S. Bates, "Discovery of a frank-kasper phase in sphere-forming block copolymer melts," *Science*, vol. 330, no. 6002, pp. 349–353, 2010.

[10] M. W. Matsen and M. Schick, "Stable and unstable phases of a diblock copolymer melt," *Phys. Rev. Lett.*, vol. 72, p. 2660, 1994.

[11] M. W. Matsen and F. S. Bates, "Unifying weak- and strong-segregation block copolymer theories," *Macromolecules*, vol. 29, pp. 1091–1098, 1996.

[12] C. Sinturel, F. S. Bates, and M. A. Hillmyer, "High χ low N block polymers: How far can we go?" *ACS Macro Letters*, vol. 4, no. 9, pp. 1044–1050, 2015.

[13] M. C. Orilall and U. Wiesner, "Block copolymer based composition and morphology control in nanostructured hybrid materials for energy conversion and storage: Solar cells, batteries, and fuel cells," *Chem. Soc. Rev.*, vol. 40, pp. 520–535, 2 2011.

[14] A. Rösler, G. W. Vandermeulen, and H.-A. Klok, "Advanced drug delivery devices via self-assembly of amphiphilic block copolymers," *Advanced Drug Delivery Reviews*, vol. 64, pp. 270 –279, 2012.

[15] M. M. Pendergast and E. M. Hoek, "A review of water treatment membrane nanotechnologies," *Energy Environ. Sci.*, vol. 4, pp. 1946–1971, 6 2011.

[16] Y. S. Thio, J. Wu, and F. S. Bates, "Epoxy toughening using low molecular weight poly(hexylene oxide)poly(ethylene oxide) diblock copolymers," *Macromolecules*, vol. 39, no. 21, pp. 7187–7189, 2006.

[17] H. Kim, S.-M. Park, and W. D. Hinsberg, "Block copolymer based nanostructures: Materials, processes, and applications to electronics," *Chemical Reviews*, vol. 110, no. 1, pp. 146–177, 2010.

[18] R. Ruiz, H. Kang, F. A. Detcheverry, E. Dobisz, D. S. Kercher, T. R. Albrecht, J. J. de Pablo, and P. F. Nealey, "Density multiplication and improved lithography by directed block copolymer assembly," *Science*, vol. 321, p. 936, 2008.

[19] F. A. Detcheverry, G. Liu, P. F. Nealey, and J. J. de Pablo, "Interpolation in the directed assembly of block copolymers on nanopatterned substrates: Simulation and experiments," *Macromolecules*, vol. 43, no. 7, pp. 3446–3454, 2010.

[20] H. Kim, C. T. Rettner, and L. Sundstrom, "Fabrication of 20 nm half-pitch gratings by corrugation-directed self-assembly," *Nanotechnology*, vol. 19, p. 235 301, 2008.

[21] E. Han, H. Kang, C. Liu, P. F. Nealey, and P. Gopalan, "Graphoepitaxial assembly of symmetric block copolymers on weakly preferential substrates," *Adv. Mater.*, vol. 22, pp. 4325–4329, 2010.

[22] S. Park, M. P. Stoykovich, R. Ruiz, Y. Zhang, C. T. Black, and P. F. Nealey, "Directed assembly of lamellae-forming block copolymers by using chemically and topographically patterned substrates," *Adv. Mater.*, vol. 19, pp. 607–611, 2007.

[23] H. Pathangi, V. Vaid, B. T. Chan, N. Vandenbroeck, J. Li, S. E. Hong, Y. Cao, B. Durairaj, G. Lin, M. Somervell, T. Kitano, R. Harukawa, K. Sah, A. Cross, H. Bayana, L. DUrzo, and R. Gronheid, "DSA materials contributions to the defectivity performance of 14nm half-pitch line flow at imec," *Proc. SPIE*, vol. 9777, 97770G–97770G–6, 2016.

[24] U. Nagpal, M. Müller, P. F. Nealey, and J. J. de Pablo, "Free energy of defects in ordered assemblies of block copolymer domains," *ACS Macro. Lett.*, vol. 1, pp. 418–422, 2012.

[25] A. J. Peters, R. A. Lawson, B. D. Nation, P. J. Ludovice, and C. L. Henderson, "Calculations of the free energy of dislocation defects in lamellae forming diblock copolymers using thermodynamic integration," *J. Micro. Nanolith. MEMS MOEMS*, vol. 15, no. 2, p. 023 505, 2016.

[26] W. Humphrey, A. Dalke, and K. Schulten, "Vmd: Visual molecular dynamics," *J. Mol. Graphics*, vol. 14, pp. 33–38, 1996.

[27] J. Stone, "An efficient library for parallel ray tracing and animation," Master's thesis, Computer Science Department, University of Missouri-Rolla, 1998.

[28] N. Laachi, H. Takahashi, K. T. Delaney, S. Hur, D. Shykind, C. J. Weinheimer, and G. H. Fredrickson, "Self-consistent field theory of directed self-assembly in laterally confined lamellae-forming diblock copolymers," *Proc. SPIE*, vol. 8323, 83230K, 2012.

[29] S. Hur, C. J. Garcia-Cervera, E. J. Kramer, and G. H. Fredrickson, "Scft simulations of thin film blends of block copolymer and homopolymer laterally confined in a square well," *Macromolecules*, vol. 42, pp. 5861–5872, 2009.

[30] R. A. Lawson, A. J. Peters, P. J. Ludovice, and C. L. Henderson, "Coarse grained molecular dynamics model of block copolymer directed self-assembly," *Proc. SPIE*, vol. 8680, 86801Y, 2013.

[31] P. J. Flory, "Thermodynamics of high polymer solutions," *The Journal of Chemical Physics*, vol. 10, no. 1, pp. 51–61, 1942.

[32] M. L. Huggins, "Solutions of long chain compounds," *The Journal of Chemical Physics*, vol. 9, no. 5, pp. 440–440, 1941.

[33] A. J. Peters, "Mesoscale simulation of block copolymer phase separation and directed self-assembly processes: Applications for semiconductor manufacturing," PhD thesis, Georgia Institute of Technology, 2015.

[34] J. Glaser, T. D. Nguyen, J. A. Anderson, P. Lui, F. Spiga, J. A. Millan, D. C. Morse, and S. C. Glotzer, "Strong scaling of general-purpose molecular dynamics simulations on GPUs," *Comput. Phys. Commun.*, vol. 192, pp. 97 –107, 2015.

[35] J. A. Anderson, C. D. Lorenz, and A. Travesset, "General purpose molecular dynamics simulations fully implemented on graphics processing units," *J. Comput. Phys.*, vol. 227, pp. 5342–5359, 2008.

[36] *MATLAB version 8.0.0.783*. Matick, Massachusetts: The MathWorks Inc., 2015.

[37] A. J. Peters, R. A. Lawson, P. J. Ludovice, and C. L. Henderson, "Detailed molecular dynamics studies of block copolymer directed self-assembly: Effect of guiding layer properties," *J. Vac. Sci. Technol. B*, vol. 31, 06F302, 2013.

[38] E. Bitzek, P. Koskinen, F. Gähler, M. Moseler, and P. Gumbsch, "Structural relaxation made simple," *Phys. Rev. Lett.*, vol. 97, p. 170 201, 17 2006.

[39] G. J. Martyna, D. J. Tobias, and M. L. Klein, "Constant pressure molecular dynamics algorithms," *J. Chem. Phys.*, vol. 101, no. 5, pp. 4177–4189, 1994.

[40] J. Cao and G. J. Martyna, "Adiabatic path integral molecular dynamics methods. ii. algorithms," *J. Chem. Phys.*, vol. 104, no. 5, pp. 2028–2035, 1996.

[41] M. E. Tuckerman, J. Alejandre, R. Lpez-Rendn, A. L. Jochim, and G. J. Martyna, "A liouville-operator derived mea-sure-preserving integrator for molecular dynamics simulations in the isothermal isobaric ensemble," *Journal of Physics A: Mathematical and General*, vol. 39, no. 19, p. 5629, 2006.

[42] T. Yu, J. Alejandre, R. López-Rendón, G. J. Martyna, and M. E. Tuckerman, "Measure-preserving integrators for molecular dynamics in the isothermal isobaric ensemble derived from the liouville operator," *Chemical Physics*, vol. 370, no. 1, pp. 294 –305, 2010.

[43] Y. Chuang, K. S. Jack, H. Cheng, A. K. Whittaker, and I. Blakey, "Using directed self assembly of block copolymer nanostructures to modulate nanoscale surface roughness: Towards a novel lithographic process," *Adv. Funct. Mater.*, vol. 23, pp. 173–183, 2013.

[44] T. P. Russell, R. P. Hjelm, and P. A. Seeger, "Temperature dependence of the interaction parameter of polystyrene and poly(methyl methacrylate)," *Macromolecules*, vol. 23, no. 3, pp. 890–893, 1990.

[45] D. P. Sweat, M. Kim, A. K. Schmitt, D. V. Perroni, C. G. Fry, M. K. Mahanthappa, and P. Gopalan, "Phase behavior of poly(4-hydroxystyrene-block-styrene) synthesized by living anionic polymerization of an acetal protected monomer," *Macromolecules*, vol. 47, no. 18, pp. 6302–6310, 2014.

[46] R. A. Lawson, A. Peters, B. D. Nation, P. J. Ludovice, and C. L. Henderson, "Effect of χN and underlayer composition on self-assembly of thin films of block copolymers with energy asymmetric block," *Proc. SPIE*, vol. 9423, p. 94231L, 2015.

[47] C. Liu, A. Ramírez-Hernández, E. Han, G. S. W. Craig, Y. Tada, H. Yoshida, H. Kang, S. Ji, P. Gopalan, J. J. de Pablo, and P. F. Nealey, "Chemical patterns for

directed self-assembly of lamellae-forming block copolymers with density multiplication of features," *Macromolecules*, vol. 46, pp. 1415–1424, 2013.

[48] F. A. Detcheverry, D. Q. Pike, P. F. Nealey, M. Mller, and J. J. de Pablo, "Simulations of theoretically informed coarse grain models of polymeric systems," *Faraday Discuss.*, vol. 144, pp. 111–125, 2010.

[49] B. D. Nation, A. Peters, R. A. Lawson, P. J. Ludovice, and C. L. Henderson, "Predicting process windows for pattern density multiplication using block copolymer directed self-assembly in conjunction with chemoepitaxial guiding layers," *Proc. SPIE*, vol. 9049, p. 90491C, 2014.

[50] A. J. Peters, R. A. Lawson, B. D. Nation, P. J. Ludovice, and C. L. Henderson, "Coarse-grained molecular dynamics modeling of the kinetics of lamellar block copolymer defect annealing," *J. Micro. Nanolithogr. MEMS MOEMS*, vol. 15, no. 1, p. 013 508, 2016.

[51] S. Hur, V. Thapar, A. Ramírez-Hernández, G. Khaira, T. Segal-Peretz, P. A. Rincon-Delgadillo, W. Li, M. Müller, P. F. Nealey, and J. J. de Pablo, "Molecular pathways for defect annihilation in directed self-assembly," *Proceedings of the National Academy of Sciences*, vol. 112, no. 46, pp. 14 144–14 149, 2015.

[52] G. M. Perera, C. Wang, M. Doxastakis, R. J. Kline, W. li Wu, A. W. Bosse, and G. E. Stein, "Directed self-assembly of lamellar copolymers: Effects of interfacial interactions on domain shape," *ACS Macro. Lett.*, vol. 1, pp. 1244–1248, 2012.

[53] D. F. Sunday, M. R. Hammond, C. Wang, W. li Wu, R. J. Kline, and G. E. Stein, "Three-dimensional x-ray metrology for block copolymer lithography line-space patterns," *J. Micro/Nanolith. MEMS MOEMS*, vol. 12, p. 031 103, 2013.

[54] R. Seidel, L. Williamson, Y. Her, J. Kim, G. Lin, P. Nealey, and R. Gronheid, "The role of guide stripe chemistry in block copolymer directed self-assembly," *Proc. SPIE*, vol. 9425, 94250W–94250W–9, 2015.

[55] L. D. Williamson, R. N. Seidel, X. Chen, H. S. Suh, P. Rincon Delgadillo, R. Gronheid, and P. F. Nealey, "Three-tone chemical patterns for block copolymer directed self-assembly," *ACS Appl. Mater. Interfaces*, vol. 8, no. 4, pp. 2704–2712, 2016.

[56] J. Kim, J. Wan, S. Miyazaki, J. Yin, Y. Cao1, Y. J. Her, H. Wu, J. Shan, K. Kurosawa, and G. Lin, "The SMART^{TM} process for directed block co-polymer self-assembly," *J. Photopolym. Sci. Tec.*, vol. 26, pp. 573–579, 2013.

[57] Y. Seino, Y. Kasahara, H. Sato, K. Kobayashi, H. Kubota, S. Minegishi, K. Miyagi, H. Kanai, K. Kodera, N. Kihara, Y. Kawamonzen, T. Tobana, M. Shiraishi, S. No-

mura, and T. Azuma, "Directed self-assembly lithography using coordinated line epitaxy (COOL) process," *Proc. SPIE*, vol. 9423, pp. 942 316–942316–7, 2015.

[58] G. Blachut, S. M. Sirard, M. J. Maher, Y. Asano, Y. Someya, A. P. Lane, W. J. Durand, C. M. Bates, A. M. Dinhobl, R. Gronheid, D. Hymes, C. J. Ellison, and C. G. Willson, "A hybrid chemo-/grapho-epitaxial alignment strategy for defect reduction in sub-10 nm directed self-assembly of silicon-containing block copolymers," *Chem. Mater.*, vol. 28, no. 24, pp. 8951–8961, 2016.

[59] H. Takahashi, N. Laachi, K. T. Delaney, S.-M. Hur, C. J. Weinheimer, D. Shykind, and G. H. Fredrickson, "Defectivity in laterally confined lamella-forming diblock copolymers: Thermodynamic and kinetic aspects," *Macromolecules*, vol. 45, no. 15, pp. 6253–6265, 2012.

[60] S. C. Glotzer and W. Paul, "Molecular and mesoscale simulation methods for polymer materials," *Annual Review of Materials Research*, vol. 32, no. 1, pp. 401–436, 2002.

[61] D. Reith, M. Pütz, and F. Müller-Plathe, "Deriving effective mesoscale potentials from atomistic simulations," *Journal of computational chemistry*, vol. 24, no. 13, pp. 1624–1636, 2003.

[62] J. Elliott, "Novel approaches to multiscale modelling in materials science," *International Materials Reviews*, vol. 56, no. 4, pp. 207–225, 2011.

[63] G. H. Fredrickson, V. Ganesan, and F. Drolet, "Field-theoretic computer simulation methods for polymers and complex fluids," *Macromolecules*, vol. 35, no. 1, pp. 16–39, 2002.

[64] E. Helfand and Z. R. Wasserman, "Block copolymer theory. 4. narrow interphase approximation," *Macromolecules*, vol. 9, p. 879, 1976.

[65] F. A. Detcheverry, D. Q. Pike, U. Nagpal, P. F. Nealey, and J. J. de Pablo, "Theoretically informed coarse grain simulations of block copolymer melts: Method and applications," *Soft Matter*, vol. 5, pp. 4858–4865, 2009.

[66] R. B. Thompson, V. V. Ginzburg, M. W. Matsen, and A. C. Balazs, "Predicting the mesophases of copolymer-nanoparticle composites," *Science*, vol. 292, no. 5526, pp. 2469–2472, 2001.

[67] S. W. Sides, B. J. Kim, E. J. Kramer, and G. H. Fredrickson, "Hybrid particle-field simulations of polymer nanocomposites," *Physical review letters*, vol. 96, no. 25, p. 250 601, 2006.

[68] M. Müller and F. Schmid, "Incorporating fluctuations and dynamics in self-consistent field theories for polymer blends," in *Advanced Computer Simulation Approaches for Soft Matter Sciences II*, Springer, 2005, pp. 1–58.

[69] P. J. Ludovice, S. Ahmed, J. Van Order, and J. Jenkins, "Simulation of intermediate order in polymeric glasses," in *Macromolecular Symposia*, Wiley Online Library, vol. 146, 1999, pp. 235–241.

[70] J. W. Jenkins and P. J. Ludovice, "A novel protocol for simulation of highly viscous molecular systems," *AIChE Symposium Series*, vol. 97, no. 325, pp. 216–219, 2001.

[71] J. W. Jenkins, "Novel efficient simulation techniques for use in molecular modeling," PhD thesis, Georgia Institute of Technology. Atlanta, Georgia., July 2000.

[72] R. F. Fox, I. R. Gatland, R. Roy, and G. Vemuri, "Fast, accurate algorithm for numerical simulation of exponentially correlated colored noise," *Phys. Rev. A*, vol. 38, pp. 5938–5940, 11 1988.

[73] D. E. Knuth, *The Art of Computer Programming*. 1969.

[74] M. Matsumoto and T. Nishimura, "Mersenne twister: A 623-dimensionally equidistributed uniform pseudo-random number generator," *ACM Trans. Model. Comput. Simul.*, vol. 8, no. 1, pp. 3–30, 1998.

[75] P. de Gennes, "Reptation of a polymer chain in the presence of fixed obstacles," *Journal of Chemical Physics*, vol. 55, no. 2, pp. 572–579, 1971.

[76] P. G. de Gennes, "Entangled polymers," *Physics Today*, vol. 36, no. 6, pp. 33–47, 1971.

[77] T. P. Lodge and M. C. Dalvi, "Mechanisms of chain diffusion in lamellar block copolymers," *Phys. Rev. Lett.*, vol. 75, pp. 657–660, 4 1995.

[78] H. Yokoyama and E. J. Kramer, "Self-diffusion of asymmetric diblock copolymers with a spherical domain structure," *Macromolecules*, vol. 31, no. 22, pp. 7871–7876, 1998.

[79] E Lorch, "Neutron diffraction by germania, silica and radiation-damaged silica glasses," *Journal of Physics C: Solid State Physics*, vol. 2, no. 2, p. 229, 1969.

[80] J. Du, C. J. Benmore, R. Corrales, R. T. Hart, and J. R. Weber, "A molecular dynamics simulation interpretation of neutron and x-ray diffraction measurements on single phase y2o3–al2o3 glasses," *Journal of Physics: Condensed Matter*, vol. 21, no. 20, p. 205 102, 2009.

[81] Y. Takahashi, S. Kitade, M. Noda, N. Ochiai, I. Noda, M. Imai, and Y. Matsushita, "Order-disorder transition of symmetric poly (styrene-b-2-vinylpyridine) in bulk and solution," *Polymer journal*, vol. 30, no. 5, pp. 388–393, 1998.

[82] H Hasegawa, N Sakamoto, H Takeno, H Jinnai, T Hashimoto, D Schwahn, H Frielinghaus, S Janβen, M Imai, and K. Mortensen, "Small-angle neutron scattering studies on phase behavior of block copolymers," *Journal of Physics and Chemistry of Solids*, vol. 60, no. 8, pp. 1307–1312, 1999.

[83] W. W. Maurer, F. S. Bates, T. P. Lodge, K. Almdal, K. Mortensen, and G. H. Fredrickson, "Can a single function for χ account for block copolymer and homopolymer blend phase behavior?" *J. Chem. Phys.*, vol. 108, no. 7, pp. 2989–3000, 1998.

[84] W. Li, P. F. Nealey, J. J. de Pablo, and M. Müller, "Defect removal in the course of directed self-assembly is facilitated in the vicinity of the order-disorder transition," *Phys. Rev. Lett.*, vol. 113, p. 168 301, 2014.

[85] W. Li and M. Müller, "Thermodynamics and kinetics of defect motion and annihilation in the self-assembly of lamellar diblock copolymers," *Macromolecules*, vol. 49, no. 16, pp. 6126–6138, 2016.

[86] B. H. Kim, S. J. Park, H. M. Jin, J. Y. Kim, S. Son, M. Kim, C. M. Koo, J. Shin, J. U. Kim, and S. O. Kim, "Anomalous rapid defect annihilation in self-assembled nanopatterns by defect melting," *Nano Letters*, vol. 15, no. 2, pp. 1190–1196, 2015.